GFZ Helmholtz Centre Potsdam

Institute of Earth and Environmental Science

Universität Potsdam

Monitoring and modeling observations of plumbing systems at caldera-like topography

Ayleen Gaete Rojas

March, 2020

Cumulative dissertation
to obtain the academic degree
"doctor rerum naturalium" (Dr. rer. nat.)
in the scientific discipline Geophysics

Submitted to the
Faculty of Mathematics and Natural Sciences
at the University of Potsdam, Germany

Primary advisor: Priv. Doz. Dr. Thomas R. Walter
Co-advisor: Priv. Doz. Dr. Sebastian Hainzl

Reviewers: Dr. Olivier Galland
Prof. Dr. Jose Palma
Priv. Doz. Dr. Thomas R. Walter

Examining committee: Prof. Dr. Torsten Dahm
Prof. Dr. Eva Eibl
apl. Prof. Dr. Frank Krüger
Prof. Dr. Jens Tronicke
Priv. Doz. Dr. Thomas R. Walter

Published online at the
Institutional Repository of the University of Potsdam:
https://doi.org/10.25932/publishup-44613
https://nbn-resolving.org/urn:nbn:de:kobv:517-opus4-446135

Statement of originality

I hereby declare that this thesis is the product of my own work. All the assistance received in preparing this thesis and the sources used have been acknowledged.

Ayleen Gaete Rojas
March, 2020

Abstract

In this dissertation, I describe the mechanisms involved in magmatic plumbing system establishment and evolution. Magmatic plumbing systems play a key role in determining volcanic activity style and recognizing its complexities can help in forecasting eruptions, especially within hazardous volcanic systems such as calderas. I explore the mechanisms of dike emplacement and intrusion geometry that shape magmatic plumbing systems beneath caldera-like topographies and how their characteristics relate to precursory activity of a volcanic eruption. For this purpose, I use scaled laboratory models to study the effect of stress field reorientation on a propagating dike induced by caldera topography. I construct these models by using solid gelatin to mimic the elastic properties of the earth's crust with a caldera on the surface. I inject water as the magma analog and track the evolution of the experiments through qualitative (geometry and stress evolution) and quantitative (displacement and strain computation) descriptions. The results show that a vertical dike deviates towards and outside of the caldera-like margin due to stress field reorientation beneath the caldera-like topography. The propagating intrusion forms a circumferential-eruptive dike when the caldera-like size is small, whereas a cone sheet develops beneath the large caldera-like topography.

To corroborate the results obtained from the experimental models, this thesis also describes the results of a case study utilizing seismic monitoring data associated with the unrest period of the 2015 phreatic eruption of Lascar volcano. Lascar has a crater with a small-scale caldera-like topography and exhibited long-lasting anomalous evolution of the number of long-period (LP) events preceding the 2015 eruption. I apply seismic techniques to constrain the hypocentral locations of LP events and characterize their spatial distribution, obtaining an image of Lascar's plumbing system. I observe an agreement in shallow hypocentral locations obtained through four different seismic techniques; nevertheless, the cross-correlation technique provides the best results. These results depict a plumbing system with a narrow sub-vertical deep conduit and a shallow hydrothermal system, where most LP events are located. These two regions are connected through an intermediate region of path divergence, whose geometry and orientation likely is influenced by stress reorientation due to topographic effects of the caldera-like crater.

Finally, in order to further enhance the interpretations of the previous case study, the seismic data was analyzed in tandem with a complementary multiparametric monitoring dataset. This complementary study confirms that the anomalous LP activity occurred as a sign of unrest in the preparatory phase of the phreatic eruption. In addition, I show how changes observed in other monitored parameters enabled to detect further signs of unrest in the shallow hydrothermal system. Overall, this study demonstrates that detecting complex geometric regions within plumbing systems beneath volcanoes is fundamental to produce an effective forecast of eruptions that from a first view seem to occur without any precursory activity.

Furthermore, through the development of this research I show that combining methods that include both observations and models allows one to obtain a more precise interpretation of the volcanic processes.

Zusammenfassung

In dieser Dissertation beschreibe ich die physikalischen Mechanismen, die maßgeblich an der Entstehung und Entwicklung von magmatischen Systemen beteiligt sind. Das magmatische System eines Vulkans spielt eine Schlüsselrolle bei der Bestimmung des vulkanischen Aktivitätsstils und die Erkennung seiner Komplexität kann bei der Vorhersage von Ausbrüchen helfen, insbesondere bei gefährlichen vulkanischen Systemen wie Calderas. Hier erforsche ich deshalb die Mechanismen der Platznahme von Eruptivgängen, sogenannten Dikes und die Geometrie der Intrusionen, welche die magmatischen Systeme unterhalb von Calderen formen, und beleuchte wie ihre Eigenschaften an der Vorläuferaktivität eines Vulkanausbruchs beteiligt sind. Zu diesem Zweck untersuche ich mit Hilfe von skalierten Labormodellen den Effekt, der durch die Caldera-Topographie induzierten Stressfeldneuausrichtung auf einen sich ausbreitenden Dike ausgeübt wird. Ich habe diese Modelle mit fester Gelatine durchgeführt, um die elastischen Eigenschaften der Erdkruste mit einer Caldera an der Oberfläche nachzuahmen. Ich injizierte Wasser als Magma-Analog und verfolgte die Entwicklung der Intrusion. Die Ergebnisse zeigen, dass ein vertikaler Dike aufgrund einer Umorientierung des oberflächennahen Spannungsfeldes unterhalb einer Caldera sowohl in Richtung, als auch nach außerhalb des Caldera-Randes abgelenkt wird. Die propagierende Intrusion bildet somit bei kleinen Calderen einen umlaufend eruptiven Dike, während sich unter großen Calderen bevorzugt sogenannte cone sheets bilden.

Um die Ergebnisse aus den vorangegangenen experimentellen Modellen zu bestätigen, werden im Anschluß die Ergebnisse einer Fallstudie beschrieben, in welcher seismologische Monitoringdaten für den Zeitraum des Ausbruchs des Vulkans Lascar im Jahr 2015 herangezogen wurden. Lascar hat einen Krater mit einer kleinräumigen caldera-ähnlichen Topographie und zeigte vor dem phreatischen Ausbruch im Jahr 2015 eine lang anhaltende Periode anomaler Entwicklung bezüglich der Anzahl der täglich registrierten langperiodischen (LP) Erdbeben. Ich habe verschiedene seismische Techniken angewendet, um die Herdregionen (Hypozentren) dieser LP-Erdbeben zu lokalisierenund ihre räumliche Verteilung zu charakterisieren, und somit ein Bild von Lascars magmatischen System zu erhalten. Ich beobachte eine Übereinstimmung in den flachen hypozentralen Positionen, die durch vier verschiedene seismische Techniken ermittelt wurden, allerdings lieferte die Kreuzkorrelationstechnik die besten Ergebnisse. Diese Ergebnisse zeigen ein magmatisches System mit einem schmalen tiefen subvertikalen Kanal und einem flachen hydrothermalen System, in dem sich die meisten LP-Ereignisse befinden. Diese beiden Bereiche sind durch einen Zwischenbereich der Pfaddivergenz miteinander verbunden, dessen Geometrie und Ausrichtung wahrscheinlich auf eine oberflächennahe Spannungsumorientierung aufgrund der topographischen Wirkung des caldera-ähnlichen Kraters zurückzuführen ist.

Um die Interpretation der vorigen Fallstudie weiter zu vertiefen, habe ich die seismischen Daten in einer weiteren Studie zusammen mit einem ergänzenden multiparametrischen Überwachungsdatensatz analysiert, und wurde darin betstätigt, dass die anomale LP-Aktivität wahrscheinlich als Anzeichen für Unruhe in der Vorbereitungsphase der phreatischen Eruption gedeutet werden kann. Hier zeige ich u.a. auch, wie die Änderungen in den verschiedenen anderen überwachten Parametern weitere Anzeichen von Unruhe im flachen hydrothermalen System erkennen ließen. Insgesamt hat diese Studie gezeigt, wie grundlegend das Erkennen komplexer Geometrien des magmatischen Systems unter Vulkanen ist, um eine effektive Vorhersage von Eruptionen zu erstellen, die auf den ersten Blick ohne Vorläuferaktivität zu erfolgen scheinen. Darüber hinaus zeige ich durch die Entwicklung dieser Forschung, dass die Kombination von

Methoden, die sowohl Beobachtungen als auch Modelle umfassen, eine genauere Interpretation der vulkanischen Prozesse ermöglicht.

Acknowledgements

Every journey has important milestones, for me, my Ph.D. thesis has been the most momentous so far. During my time in Germany, I have met many brilliant people, whose support has been greatly appreciated.

First of all, my Ph.D. achievement, together with the experience of living in Germany was possible thanks to the program Forschungsstipendium für Doktorat from Deutscher Akademischer Austausch Dienst DAAD that funded this project, and as such I wish to express my deepest gratitude.

I also wish to thank my supervisor Dr. Thomas R. Walter for sharing his knowledge and enthusiasm for research with me.

I would also like to extend my deepest appreciation to my colleague and friend Dr. Mehdi Nikkhoo who provided unbounded support during the long process of obtaining my Ph.D. degree. Mehdi's mentoring and kindness guided me in the toughest moments of my studies.

I would like to extend my appreciation to Dr. Eleonora Rivalta and Dr. Janine Kavanagh. Both supported my research project with empathy and motivated me to develop my career as a researcher, demonstrating in the process, that women have a lot to contribute to science.

Finally, I am infinitely grateful to my family, despite the physical separation they have always been present, showing their love and supporting me during this process.

Contents

Chapter 1

Introduction

1.1 Plumbing systems at caldera-like topography

Calderas are topographic lows that can form due to explosive eruptions or gradual the reservoir drainage driving the subsidence of the plumbing system roof along caldera ring faults. Once the caldera is formed, the plumbing system can remain untouchable or be modified by the re-intrusion of magma in different scales and geometries. This consequently produces unrest at calderas that eventually may end in eruptions (Kennedy et al., 2018).

The plumbing systems are networks of intrusions and storage bodies through which magma is transported and stalled below and inside of active volcanic systems (see Caricchi and Blundy, 2015; Galland et al., 2015). At calderas, the plumbing system configuration consist of shallow structures and magma bodies that adopt a broad variety of dimensions and shapes (see Fig. 1.1). They are classified according to the geometry and emplacement mechanism of the intrusion, such as sub-vertical (dikes and ring dikes), inclined (circumferential dikes and cone sheets) and lateral intrusions (sills and laccoliths) (Anderson, 1936; Galland et al., 2015). Dikes are approximately vertical laminar intrusions that travel upwards and/or laterally, cutting the host rock or sediment independently of any discordant layering. Ring dikes grow similarly to dikes, nevertheless, they are formed by subsidence that commonly occurs along a ring fault, where magma is intruded to form the ring dike. The inclined sheets are typically igneous bodies that may feed eruptions; circumferential dikes have an arcuate horizontal section and cone sheets taper downwards towards a central point with a circular horizontal section.

Lateral intrusions such as laccoliths and sills are sub-horizontal intrusions that grow concordant to the stratification of the surrounding host rocks. The geometry depicted by a laccolith is an upper-domed margin limited by a flat margin in the lower part. Sills have a flatter geometry in comparison with laccoliths, and the stacking of sills produces a sill complex. Furthermore, most of the volcanoes contain in the shallowest part of the plumbing system a network of channels conforming the hydrothermal system. This is the result of the interaction of the upper part of the magma plumbing system with the crust, hydrosphere, and atmosphere, producing heating and pressurization of hydrothermal fluids and inducing changes in the geophysical and chemical parameters.

The organization and geometry of the intrusions that shape the volcanic plumbing system as well as the emplacement and propagation can be determined by mechanical factors. They act on the surrounding host rock and together with the physical properties of the intruding fluid determine the magma transport and emplacement in the crust (Burchardt et al., 2018). A commonly-observed factor is the ambient stress field that can be governed by tectonic conditions as compression or extension, or regional and local conditions due to topographic irregularities. Changes in the ambient stress cause the reorientation of its components, implying the deviation of the dike trajectory according to the new orientation of the maximum compressive stress

component (σ_1) (Anderson, 1936). In this regard, evidence of magma emplacement beneath active (e.g., Long Valley caldera, USA, Prejean et al., 2003)) and eroded (e.g., Tejeda caldera, Canary Islands, Schmincke, 1967) calderas have demonstrated the effect of their topographic architecture on the magma emplacement and development of their plumbing system. The structures that form the plumbing systems of calderas have resulted in the formation of magmatic intrusions with inclined section as cone sheets and circumferential dikes described previously. Their geometries have been associated with the effect of unloaded stress fields induced by the caldera topography (Corbi et al., 2016).

The complexity of a volcanic plumbing system is associated with its historical eruptions, stratigraphy and magma chemistry. These parameters determine the dimension of the plumbing system, varying from less complex structures such as small-scale basaltic monogenetic volcanoes (Németh and Kereszturi, 2015) to very complex and large-scale plumbing systems observed in rhyolitic calderas (Kennedy et al., 2018). Plumbing systems with shallow magma storage within a volcanic edifice usually host magmatic activity that displays surface expressions such as surface deformation, gas exhalation, thermal spots, etc. This activity allows close monitoring and the opportunity to study these volcanic processes to forecast eruptions and assess their associated risk (Sparks, 2003). Nevertheless, the challenge associated with volcano monitoring occurs when the volcanic plumbing system is not identified and/or the signs of activity weak increases the potential for damages and casualties due to the lack of identification of precursor activity. For instance, the most hazardous volcanic systems are silicic calderas for which in general, geophysical and geochemical studies reveal shallow aseismic zones with extension that can be larger than the caldera size but with a low geometric definition, usually interpreted as sills and laccoliths (Kennedy et al., 2018). Thus, the complexities of the subsurface structures of silicic calderas and in general explosive volcanoes are often tricky to identify through geophysical data due to seismic signal scattering effects produced by irregularly-layered topographies (Wegler and Lühr, 2001).

Hence, detection of the volcanic plumbing systems can provide information about the location of storage bodies as well as provide clues about the magma chemistry. This information can also provide knowledge about the dynamics involved in the establishment of the plumbing system and physical processes conducted within it that evolve in unrest or eruptive activity, governing the eruption style and magnitude. Multidisciplinary approaches in this field may provide a global comprehension of the role played by plumbing systems through geophysical and geodetic methods, geological and structural evidence, geochemistry and modeling (Burchardt and Galland, 2016).

The aforementioned remarks imply the imminent need for understanding the establishment and arrangement of plumbing systems as well as the volcanic processes that are caused by their complexities and features. This can be approached through observations that consider *in-situ* and remote monitoring combined with the modeling of processes that confer those observations. Thus, with this dissertation, I aim to explore the mechanisms involved in the magma pathway and plumbing system formations in the caldera-like environment and their role as hosts of eruptive activity. On different scales, I study the effect of topographic unloading produced by a caldera architecture on the magma migration and emplacement by using laboratory models conducted in gelatin as the analog of earth's crust and injecting dyed water as the magma analog. Later, I search for evidence of the unloading topographic effect on the configuration of the plumbing system of Lascar volcano, Chile. Lascar is one of the most active volcanoes of the Central Volcanic Zone of the Andes, whose activity is characterized by frequent phreatic explosions in the absence of precursor activity. Lascar contains a summit crater that exhibits a small-scale caldera-like topography and a permanent multiparametric monitoring network that makes it attractive to test the results obtained from laboratory models. I approach the

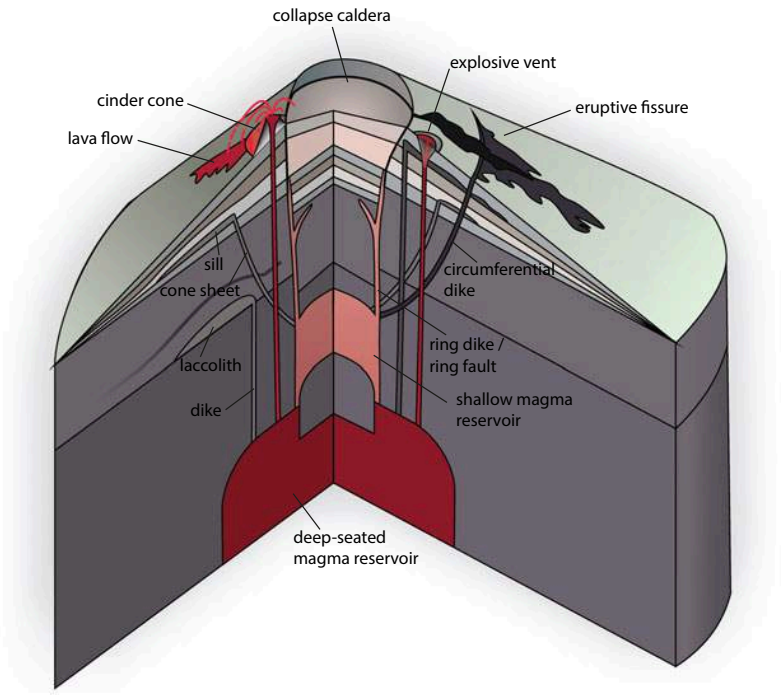

Figure 1.1: Schematic representation of the main intrusions and magma bodies that shape the volcanic plumbing system beneath a caldera: 1) Sub-vertical (dikes and ring dikes); 2) Inclined (circumferential dikes and cone sheets); 3) Lateral intrusions (laccoliths, sills); 4) Magma reservoirs (shallow and deep magma reservoirs). Modified from Galland et al. (2015). The geometry depicted here is more simplified and may be much more asymmetric in nature.

Lascar case by reconciling its plumbing inner structure through the location of long-term (LP) seismic events to prove whether the seismicity depicts evidence of any effect of the caldera-like crater on the stress field. Later, I explore the role of the caldera-like crater architecture and its evidenced deepening in the preparatory phase of the phreatic eruption occurring on 30 October 2015, and consequently on the co- and post-eruptive phases.

1.2 Methods

In the development of this dissertation, I have applied different methods that involve laboratory models and *in-situ* record techniques supported by remote-sensing data to monitor the volcanic activity. The selection of these techniques was based on the data collected in field campaign and laboratory work. Furthermore, the chosen techniques allow interpreting the processes and determine the type of complexity that I approach in each study. Laboratory models provide a simplified approach to simulate the process under study, while monitoring data is used to verify these results in detail. A general description of these methods is given below.

1.2.1 Laboratory modeling

Laboratory models have been successfully used to model complex processes occurring in the earth that have not been easy to approach numerically. Through these models we are able to study processes that occur on a spatiotemporal scale that spans from microns to thousands of kilometers and from milliseconds to millions of years (Galland et al., 2015). They are spatially and/or temporally scaled through the geometry, kinematics and dynamics that govern the studied processes (Buckingham, 1914). I selected gelatin as the analog for the earth's crust and water as the analog for magma. The elastic properties of gelatin prepared at low concentrations

(2.0–5.0 wt %) and solidified at low temperatures (5–10 °C) are suitable to study the effect of the crustal stress reorientation on propagating intrusions (Di Giuseppe et al., 2009). Accordingly, water was chosen due to its low viscosity, suitable to represent basaltic magma that is mostly driven by the overpressure of liquid injected from a distant source (Kervyn et al., 2009). This technique is described in detail and applied in chapter 2.

1.2.2 Volcano monitoring

Volcano monitoring provides scientifically-valid data that can be successfully applied to study processes occurring in the volcanic plumbing system, allowing one to characterize and forecast eruptions as well as determine inner and outer volcanic structures (Sparks et al., 2012). This provides us quantitative data from which we can observe the evolution of real parameters on time scales that will help to interpret specific processes. Deploying a variety of instruments enables us to detect signs of changes in the activity to obtain an improved understanding of the volcanic processes including observations related to the chemistry of volcanic fluids and rocks and physical processes associated with earthquakes and ground deformation (Scarpa and Tilling, 2012). Nevertheless, the most hazardous activity occurs when these signs are not easily detectable and eruptions occur without any warning. Volcanoes exhibiting surprise eruptions require multidisciplinary permanent monitoring that includes ground-based and space-based as well as sporadic airborne-based techniques, as well as networks that can warn populations about precursory phenomena of eruptive activity in order to reduce the volcanic hazard. One such case is the Lascar volcano, whose historical eruption record repeatedly exhibits a phreatic style (e.g., González-Ferrán, 1995; Siebert et al., 2010). Additionally, the Lascar activity is characterized by continuous emission of magmatic gases that reports about the plumbing system activity. This feature necessitates permanent monitoring of gas constituents such as SO_2 and CO_2 as well as physical parameters that can provide information about changes in the volcanic activity. Thus, monitoring is carried out by using a multidisciplinary instrument network including a seismometer, cameras, and gas and temperature sensors which provide a complete data set which can be complemented by available remote-sensing data. Thus, Chapter 3 details the techniques applied to seismic data to characterize seismicity and to identify the plumbing system of Lascar based on the location of the long-period (LP) seismic signals. These events are characterized by an emergent onset with no clear S phase and narrow predominant frequencies in the low-band (0.2-10 Hz), usually associated with resonance due to fluid movement in a cavity (Chouet, 1986, 1988). Chapter 4 combines the entire data set to identify the pre-, co- and post-eruptive activity associated with the 2015 eruption of Lascar, where I search for evidence of the caldera-like crater's effect on the evolution of these activity phases.

The methods described here complement each other according to their advantages and disadvantages. While laboratory models are able to reproduce processes in a broad spatiotemporal range, volcano monitoring is limited to human-time scales. Additionally, laboratory models can be reproduced to repeat the same process under study assuring the same result if the parameters involved are well-known and constrained. This provides full control over the measurements. Usually, this method is less expensive and doesn't require maintenance as in the case of monitoring. However, the parameters that can be successfully tested in models are fewer than those that can be investigated through monitoring. Thus, the independent application of these two methods may provide an entire picture of the volcanic process.

1.3 Research questions and outline

This thesis combines aspects of volcanic plumbing systems since their formation and the role that they play as a channel that harbors volcanic activity and causes eruptions, focusing on plumbing structures placed in caldera-like settings. As the thesis is cumulative, a collection of individually-published articles is organized in chapters. Each chapter introduces a different method applied to study a specific aspect concerning to plumbing systems and provides interpretations based on observations and previous work. First, I experimentally test the origin of the magma emplacement beneath caldera-like topographies and detect patterns that can be found in nature. Later, I apply seismic location techniques to identify these patterns in the inner structures of a volcano with a caldera-like crater architecture. Finally, I test the implications of this arrangement on the eruptive phases of the same volcano by combining a multidisciplinary data set. The different techniques and methods are part of the knowledge and tools acquired during my Ph.D. studies.

The thesis is organized by chapters. Chapter 2 to Chapter 4 present articles that are published in a peer-reviewed journal. The observations and research questions as well as a summary of findings addressed by the three articles are listed below:

1. **Chapter 2:** Understanding the factors involved in the emplacement of magma pathways and the establishment of volcanic plumbing systems may help in the assessment and mitigation of volcanic eruptions. Calderas are the most hazardous volcanoes and during post-caldera volcanism, geological and geophysical evidence have shown that magma typically is transported through laminar intrusions. These sheet intrusions include circumferential dikes and cone sheets among a variety of forms (see Burchardt et al., 2018) and have been observed, for instance, in the plumbing system of ancient calderas or feeding the eruptions of active ones. Studies developed in the last years have found that mass unloading in the caldera-like topography produces the reorientation in the surrounding medium, inducing emplacement of laminar intrusions with inclined and circumferential shape (Corbi et al., 2015, 2016). Nevertheless, it is still unclear how the variety of these intrusions can occur in the same geological setting. Thus, the open questions to address are:

   - How does the unloading stress field due to caldera-like topography control the dike propagation (geometry and the velocity of the intrusion emplacement)? What are the parameters playing key roles in the stress changes? Which intrusions are more likely to feed eruptions in caldera environments?

   Chapter 2 explores the dynamic process of fluid emplacement in the development of shallow plumbing systems at calderas. I designed and conducted scaled laboratory models using gelatin as the crust analog with a caldera-like topography on the surface, injecting water in the bottom as the magma analog. I tracked intrusion growth, described the sub-surface stress changes and quantified the displacement and strain to follow the evolution of the intrusion emplacement. Unloading stress due to caldera-like topography induces the path deviation of a dike propagating upwards beneath the caldera-like topography to finally form laminar intrusions with round geometry. I recognized the caldera-like diameter as the key parameter in determining the geometry of these shallow intrusions, obtaining an eruptive circumferential dike when the diameter was small and a cone sheet for a large diameter. These results are compared with natural cases and can assist in the interpretation of geological and geophysical data.

2. **Chapter 3:** Identification of deep structures that harbor volcanic processes may help to detect unrest and forecast volcanic eruptions. Seismic techniques have been demonstrated

as useful tools to infer magma pathway complexities and plumbing systems and they are applied to determine the mechanism that produces movement of stationary fluids and/or their transport. For instance, Lascar volcano is one of the most active volcanoes in Chile, exhibiting a permanent degassing attributed to hydrothermal activity (Tassi et al., 2009). The high rate of degassing has been proposed to be stimulated by the continuous deepening of the active crater floor (Matthews et al., 1997) due to sustained cooling, compaction and gravitational sliding (de Zeeuw-van Dalfsen et al., 2017). These changes have been associated with increased numbers of long-period (LP) events preceding an eruption (González et al., 2016). Likewise, Lascar exhibited a long-lasting increase in the number of long-period (LP) events prior to the 2015 eruption. During part of this unrest period, the seismic network was highly densified, which provides the opportunity to carry out a detailed study to characterize its seismicity, addressing the following questions:

- What is the spatiotemporal distribution of LP events? Does the spatial distribution of LP events depict the Lascar plumbing system and its arrangement? Does the architecture of the caldera-like crater have any implication on the plumbing system arrangement?

The data used in Chapter 3 were collected during field campaigns conducted between 2014-2017. I designed and coordinated the installation of the stations as well as their maintenance. Using these data, I constrain the location through two commonly-used methods to locate LP events: waveform amplitude (Battaglia et al., 2003) and polarization (e.g., Cesca et al., 2008). Furthermore, two new approaches are proposed to overcome the challenge of the P-wave onset identification. The first method is based on the coherent detection of anomalous amplitudes and polarization attributes at multiple stations (Grigoli et al., 2013, 2014) and the second uses the cross-correlation of similar waveforms recorded at different stations to infer the hypocenters; this method is used for the first time to locate LP events. In general, the methods agree in shallow hypocentral locations extending down to 5 km beneath the summit, where best result is obtained by the cross-correlation method. These results image a spatial distribution extending in depth along a narrow, conduit-like path and a shallower region exhibiting varying complexities. However, most LP events are located within the first 2 km beneath the summit of the dormant western edifice, indicating the presence of a shallow hydrothermal system. An intermediate region of path divergence covering 1 km depth possibly accommodates the shallow part with the sub-vertical deeper conduit located in the active eastern edifice. A likely explanation for the deviating arrangement of the shallowest events towards the dormant edifice is the effect of the sustained deepening of the active crater that constrain its caldera-like architecture, producing unloading stress influencing the plumbing system arrangement. This process causes volcanic activity migration primarily due to degassing and crater morphology. Additionally, similarities among the waveforms result in the resolution of a single type of signal and thus a single process responsible for the LP activity.

3. **Chapter 4:** The frequent eruptive activity of Lascar volcano has been characterized primarily by a phreatic style. Therefore, this topic does not deal with magmatic plumbing systems, but attempts to better understand this current behavior. These eruptions are generally attributed to the direct feeding of magmatic gases into a deep hydrothermal system or via an open-conduit degassing supplied to a shallow hydrothermal system (Stix and de Moor, 2018). Studies carried out in Lascar have identified a source of tremor at a depth of 2–3 km, possibly associated with fluid migration (water and/or gas) in a shallow hydrothermal system (Hellweg, 2000). This hypothesis was later supported by a magnetotelluric study that identified a high-conductivity volume located at ~1 km beneath the summit (Díaz et al., 2012). Furthermore, the magma reservoir has been hypothesized to be located deeper than

5 km (Díaz et al., 2012; González et al., 2015) from where the fluids ascend to shallow depths to interact with the hydrothermal system influencing the active degassing (Tassi et al., 2009) and the sustained deepening of the active crater (Matthews et al., 1997). The 2015 phreatic eruption of Lascar showed no clear precursory activity. However, after a retrospective analysis, I observe that the explosion was preceded by unrest observed from the gradual changes in the number of LP events over the course of one year with manifestation in the SO_2 flux and a gradual inhibition of the thermal anomaly. 10 days before the eruption, a period of unusual changes in the brightness of the permanent volcanic plume began immediately after strong precipitation. After the eruption, the changes in brightness lasted for a few days accompanied by an increase in fumarole temperature and CO_2 concentration. Additionally, an enhancement of the thermal anomaly as a consequence of the eruption slowly decreased for one year after the eruption. This introduces the following open questions:

- What is the role played by the hydrothermal system in the preparatory phase of the 2015 eruption? What can we learn from the Lascar case to successfully monitor the unrest activity in volcanoes that do not show clear precursor activity?

Chapter 4 reports changes in the parameters measured in the gas fumarole as well as seismicity and thermal anomalies on the active crater of Lascar associated with the 2015 phreatic eruption. I participated in the field campaigns to collect the data and performed station maintenance. One key finding from the analysis of these data is that the shallow hydrothermal system and the persisting deepening of the active crater, inducing by cooling, provide the optimal condition to build pressure during the pre-eruptive phase. Here, I suggest that a magmatic feeding is necessary to maintain the degassing, which can be affected by a blockage in the fluid path due to the deepening. This is hypothesized to be reflected by the inhibition of the thermal anomaly towards the eruption together with the reduction of the number of LP events the last four months. Furthermore, post-eruptive observations of the thermal anomaly revealed an increased size and intensity of this hot spot on the active crater just after the eruption. This gradually decreases over one year following the eruption, whose observation may also be in part attributed to crater deepening. Additionally, inference of a hydrothermal system located in the shallow region of the dormant edifice may support an effective and fast percolation of the meteoric water in the system, boosting changes in the fumarole brightness as well as the cyclic trend in the variation of the fumarole temperature with respect to the CO_2 concentration. This suggests the percolation of meteoric water acts as a trigger of the phreatic eruption; nevertheless, the absence of anomalous volcanic activity after previous strong precipitations is also discussed. Thus, this retrospective study implies that even though volcanoes do not seem to show precursory activity, this can be effectively identified and monitored if the volcano has an appropriate monitor network. In particular, volcanoes with shallow plumbing systems can be easily monitored and provide high-quality data for efficient detection of unrest and forecasting eruptions.

1.4 Author's contributions and publications

Chapters 2 to 4 of this thesis are peer-reviewed articles in scientific journals as listed below:

- Chapter 2:

  Gaete, A., Kavanagh, J. L., Rivalta, E., Hilmi Hazim, S., Walter, T. R., Dennis, D. J. C. (2019): The impact of unloading stresses on post-caldera magma intrusions. - Earth and Planetary Science Letters, 508, 109–121. doi:10.1016/j.epsl.2018.12.016

- The author, AG, designed and carried out the laboratory models and wrote the manuscript implementing suggestions from the first co-author JLK and the other co-authors including her Ph.D. adviser TRW. ER contributed significantly in the scaling method, SHH helped in carrying out the experiments and DJCD provided the trace particle laboratory setup.

- Chapter 3:

  Gaete, A., Cesca, S., Franco, L., San Martin, J., Cartes, C., Walter, T. R. (2019): Seismic activity during the 2013 – 2015 intereruptive phase at Lascar volcano, Chile. - Geophysical Journal International, 219, 449–463. doi:10.1093/gji/ggz297

  - The author, AG, wrote the manuscript, designed the seismic network installation and participated in the field campaigns to install the stations, collecting and processing part of the data. SC implemented most of the seismic location techniques and made suggestions to improve the manuscript together with observations provided by LF and Ph.D. adviser TRW. JSM implemented and taught to AG one of the techniques to localize the LP events, while CC re-localized the VT events.

- Chapter 4:

  Gaete, A., Walter, T. R., Bredemeyer, S., Zimmer, M., Kujawa, C., Franco, L., San Martin, J., Bucarey Parra, C. (2020): Processes culminating in the 2015 phreatic explosion at Lascar volcano, Chile, monitored by multiparametric data. - Natural Hazards and Earth System Sciences, 20, 377–397. doi:10.5194/nhess-20-377-2020

  - The author, AG, wrote the manuscript, participated in the field campaigns to collect the data and processed part of the data. Her Ph.D adviser TRW provided part of the camera and Sentinel-2 data, made suggestions to improve the manuscript together with SB, who also provided the analysis of SO_2 measurement. MZ provided the analyzed CO_2 measurements and helped revise the manuscript together with LF. CK, JSM and CBP participated in the field campaigns, as well as TRW and MZ.

The following work has benefited from the author's contribution and has been published in the course of her Ph.D. research; however, it is not included as a part of this thesis:

- Zimmer, M., Walter, T. R., Kujawa, C., Gaete, A., Franco-Marin, L. (2017): Thermal and gas dynamic investigations at Lastarria volcano, Northern Chile. The influence of precipitation and atmospheric pressure on the fumarole temperature and the gas velocity. - Journal of Volcanology and Geothermal Research, 346, 134–140. doi:10.1016/j.jvolgeores.2017.03.013

  - AG participated in the field campaigns to collect the data and helped revise the manuscript.

Chapter 2

The impact of unloading stresses on post-caldera magma intrusions

Abstract

Calderas represent morphological depressions several kilometers in diameter, and the unloaded crustal stresses they produce can form rapidly (e.g. Pinatubo, 1990) or slowly (e.g. Hawaii, 2018). Active calderas are known as sites of persistent magma intrusions, and yet the dynamics of their shallow plumbing system is not well constrained. We use scaled laboratory experiments to study how experimental intrusions are created beneath a caldera by injecting dyed water (magma analogue) into the base of an elastic gelatin solid (crust analogue) with a cylindrical cavity in its surface to mimic a caldera-like topography. The evolving dike geometry and stress field were qualitatively determined using polarized light, and digital image correlation allowed the incremental and total strain to be quantified by tracking passive-tracer particles in the gelatin that fluoresced in a thin 2D vertical laser sheet. Our results show that the unloaded stress field from a caldera can cause a divergence of vertical dikes, and leads to circumferential dikes and cone sheets. When the caldera was large the initially vertical dike became arrested, then grew laterally via circumferentially-propagating en echelon segments; these eventually joined to complete a cone sheet that was parallel to, but extended outside and beneath, the large caldera. When the caldera was small, a circumferential dike erupted, producing a short fissure which was outside, but parallel to, the caldera. We suggest that the distinct curved geometry, velocity, strain and stress characteristics of circumferential dikes and cone sheets can be used to interpret the origin and growth of post-caldera magmatism and the likelihood of eruption in caldera systems.[1]

[1]Originally published as: Gaete, A., Kavanagh, J. L., Rivalta, E.,Hilmi Hazim, S., Walter, T. R., Dennis, D. J.C. (2019): The impact of unloading stresses on post-caldera magma intrusions. Earth and Planetary Science Letters, 508, 109-121. doi:10.1016/j.epsl.2018.12.016

2.1 Introduction

Calderas are associated with some of the largest volcanic systems (e.g. Yellowstone, USA) where topographic lows form due to subsidence along caldera ring faults (Cole et al., 2005). Caldera-forming events can be rapid (Mt Pinatubo in Philippines, 1990, e.g. Pallister et al., 1996) or slow (Kilauea volcano in Hawaii, 2018, e.g. USGS, 2018) and may form due to explosive volcanic eruptions (Cole et al., 2005) or gradual drainage of a deep reservoir by lateral intrusion. Despite the largest cataclysmic eruptions being produced during the formation of the caldera itself (Jellinek and DePaolo, 2003), unrest at calderas and relatively small post-caldera eruptions are frequent and pose a significant hazard to the population. Caldera systems are active sites of mineralization, and understanding their development and impact on the volcanic plumbing system is important for georesources, e.g. copper-porphyry deposits (e.g. Blundy et al., 2015), and carbonatite-hosted Rare Earth Elements (e.g. Le Bas, 1987). Irregular topographies and crustal loads are common in volcanic terrains, from tectonic rift zones (e.g. Afar and Iceland) to laterally collapsed sectors of a volcanic edifice (e.g. Mt St Helens, USA), unstable volcanic islands (e.g. La Palma, Canary Islands), ice unloading, and excavation of quasi-cylindrical craters associated with volcanic vents, calderas, tuff cones and diatremes.

Field observations suggest that post-caldera magmatism typically occurs via inclined sheet intrusions (Burchardt et al., 2011). These may take a variety of forms (e.g. Burchardt et al., 2018). In this paper we use the terms 'circumferential dike', which have an arcuate horizontal section, and 'cone sheet', which taper downwards towards a central point and have a circular horizontal section, to distinguish and reflect the end member intrusion geometries, without reference to their process of formation. These intrusion types are common igneous magma bodies, are a major constituent of sub-volcanic plumbing systems, and may feed eruptions in caldera settings (e.g. Bagnardi et al., 2013; Chadwick et al., 2011).

There are several contrasting conceptual models to explain cone sheet formation, but these often do not invoke the presence of a caldera. For example, Galland et al. (2014) carried out an experimental study of cone sheet development by injecting oil into compacted silica flour with a flat topography. They found that cone sheets formed due to a dynamic dimensionless ratio which included the effects of magma viscosity and host-rock deformation mode. In comparison, Magee et al. (2012) proposed that cone sheets form by lateral propagation of regional dikes from an adjacent source, whereas other authors invoke stress changes from a central magma chamber at depth (Anderson, 1936; Geshi, 2005; Johnson et al., 1999; Schmiedel et al., 2017). These fundamentally different models demonstrate there remains uncertainty in the growth dynamics of the magmatic system, and cone sheets in particular. Accurately interpreting the surface signals of magma movement for hazard assessment at active volcanoes ultimately depends on the quality of the models upon which these inferences are made (Di Vito et al., 2016; Guldstrand et al., 2017).

The emplacement, propagation and geometry of magma intrusions are influenced by several related factors including density contrasts between magma and host-rock, the ambient stress field (tectonic, regional or local), stress barriers, the physical properties of the intruding magma (e.g. viscosity), and mechanical heterogeneities in the crust such as rock layering and faults (see reviews by Burchardt et al., 2018; Rivalta et al., 2015). A commonly explored scenario is that of dike propagation beneath a volcanic edifice where crustal loading influences the tendency for magma to stall at depth or erupt, and whether an eruption occurs in the summit or flank of the volcano (Kervyn et al., 2009; Maccaferri et al., 2011), depending on the magma buoyancy, edifice size and crustal layering (density, rigidity and interface weakness).

The load from a volcanic edifice can cause the attraction of dikes located away from the volcano, and in some cases promote their lateral (blade-like) propagation rather than vertical

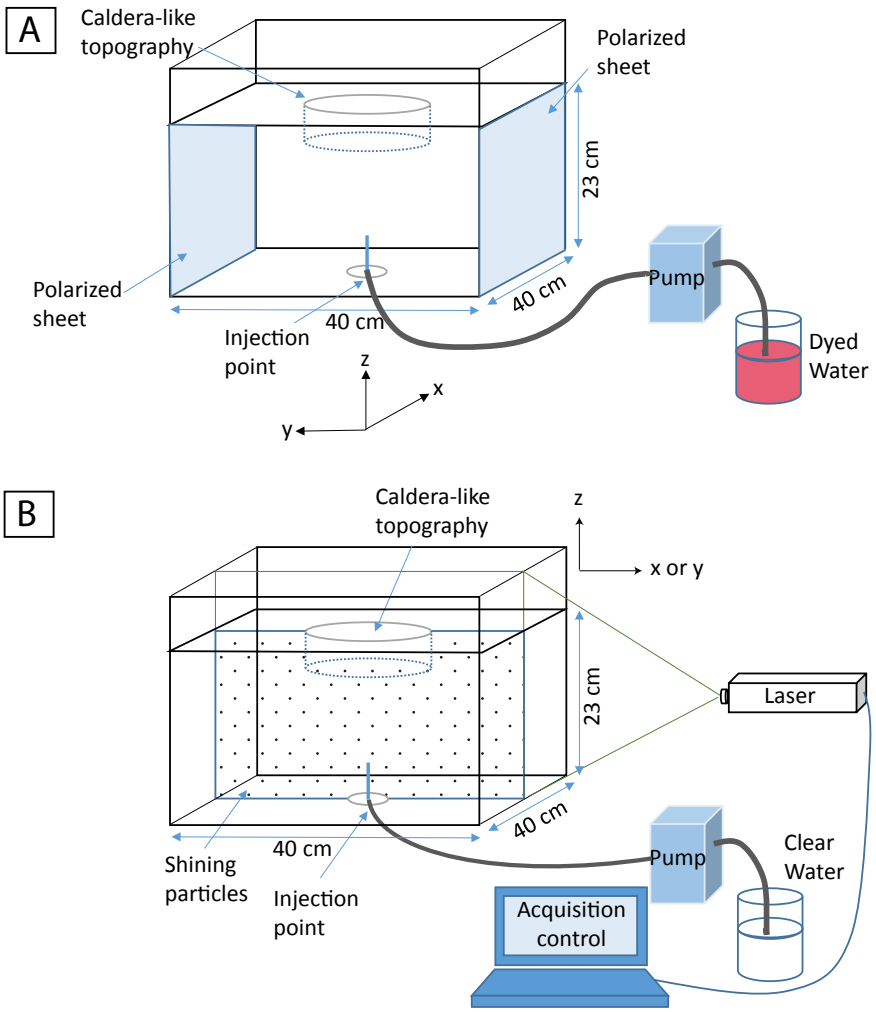

Figure 2.1: Schematic diagram of the experimental setups. A) Polarized light experiment: dyed water is injected into the base of a gelatin slab using a peristaltic pump. The gelatin surface is modeled to have a caldera-like topography, and stress in the gelatin is visualized using two parallel polarized sheets attached to the tank walls on the $x-z$ plane and perpendicular to the initial dike profile. Two HD video cameras (not shown) record images the $x-z$ and $y-z$ directions. B) Tracer particle experiment: a high intensity vertical laser sheet illuminates a 2D profile (either $x-z$ plane or $y-z$ plane) through the center of the tank and exciting passive-tracer fluorescent particles in the gelatin. A CCD camera records the illuminated plane at 1 frame per second, synchronized with the laser.

growth (Watanabe et al., 2002). This supports the hypothesis that dikes change their trajectory during propagation in response to perturbations of the maximum compressive stress (σ_1), whose orientation may vary due to local or regional compression or extension of the medium (Anderson, 1936; Maccaferri et al., 2011; Mathieu et al., 2015; Rivalta et al., 2015).

Magma propagation under a topographic low, such as a caldera, has been relatively unexplored, despite such unloaded stress fields being common features in volcanic terrains (Corbi et al., 2015; Mathieu et al., 2015). Numerical and analogue modeling suggest that a caldera geometry in a volcanic edifice induces unloading stresses that in a cohesive, crystalline rock may favor the emplacement of laminar intrusions with circumferential and/or radial shapes and sills (Corbi et al., 2016, 2015).

Despite the significance of post-caldera magmatism, questions remain regarding the nature of magma intrusion in an unloaded crust. We present results from gelatin laboratory experiments that model the emplacement of a dike in the vicinity of a caldera-like topography. The experiments integrate measurements of sub-surface strain evolution and stress evolution using digital

image correlation and polarized light, respectively. Our results test existing models of circumferential dike and cone sheet development and assist in their interpretation by constraining their geometry, propagation pathway, sub-surface deformation and likelihood of eruption.

2.2 Modeling framework

Following the approach described by Merle (2015), we define a laboratory prototype scaled geometrically (ratio of distances is constant in nature and the prototype), kinematically (the geometric scaling is maintained over time), and dynamically (the ratio of the mechanical forces between nature and the model is constant). Our selected analogue material for the crust is gelatin, and for magma we have selected water (see Supplementary Table S1 for detailed scaling). Gelatin has been very well studied in scaled laboratory experiments to simulate elastic process in the crust associated with magmatic intrusions (Di Giuseppe et al., 2009; Kavanagh et al., 2013). Gelatin is a visco-elastic material and its transparency allows the evolving dynamic process of dike propagation to be visually tracked in an experiment (Takada, 1990; Watanabe et al., 2002). When used at low concentration (2–5 wt %) and at low temperature (5–10 °C) it behaves elastically over the timescale of an experiment (Kavanagh et al., 2013), which lasts approximately 10 minutes. Gelatin has been intruded by a range of fluids to simulate dike emplacement (see for a review Kavanagh et al., 2018b). We have chosen water as the magma analogue as it is a low-viscosity fluid (10^{-3} Pa s) and is slightly less dense than the gelatin ($\Delta\rho = 6\,\mathrm{kg\,m^{-3}}$). It is a suitable analogue to simulate intrusions of low to intermediate viscosity magma that is mostly driven by the overpressure of liquid from a distant source (Kervyn et al., 2009), and it has been used in several previous experiments that study dike propagation (Kavanagh et al., 2018a; McLeod and Tait, 1999). We define the geometric scale between nature n and prototype p in our experiments as the length scale factor:

$$L^* = \frac{L_p}{L_n} \tag{2.1}$$

Giving $L^* = 1.0 \times 10^{-5}$ such that 1 cm in the laboratory represents 1 km in nature, considering that in nature the size of calderas range from 1 km to tens of kilometers in diameter (see Table S1). An alternative length scale factor is the buoyancy length L_b when magma buoyancy drives the rock fracture (Corbi et al., 2016; Kavanagh et al., 2013; Merle, 2015):

$$L_b^* = \left(\frac{K_c}{\pi^{1/2}\Delta\rho g}\right)^{2/3} \tag{2.2}$$

where K_c is the fracture toughness of the host medium, $\Delta\rho$ is the density contrast between host rock and magma, and g is gravity (Taisne and Jaupart, 2009). Therefore we calculate $L_b^* = 4.1 \times 10^{-5}$ (see Table S1). Overall, the two length scales (Equations 2.1 and 2.2) agree as they are within the same order of magnitude.

We have used two contrasting approaches to scale the stresses in our experiments: firstly we scale the elastic deformation of the host material, and secondly we scale the unloading pressure associated with the caldera. Firstly, we calculate the strain scale factor e^*:

$$e^* = \frac{a}{b} \tag{2.3}$$

where a is the dike thickness and b is the dike width. This means $e^* = 10$ when $e_n = 0.002$ and $e_p = 0.02$ in gelatin (Kavanagh et al., 2013). We define a Young's modulus scale factor $E^* = 3 \times 10^{-7}$, as $E_n = 10^9$–10^{10} (Kavanagh et al., 2013) and $E_p = 300$–3000 (see Table S1). As

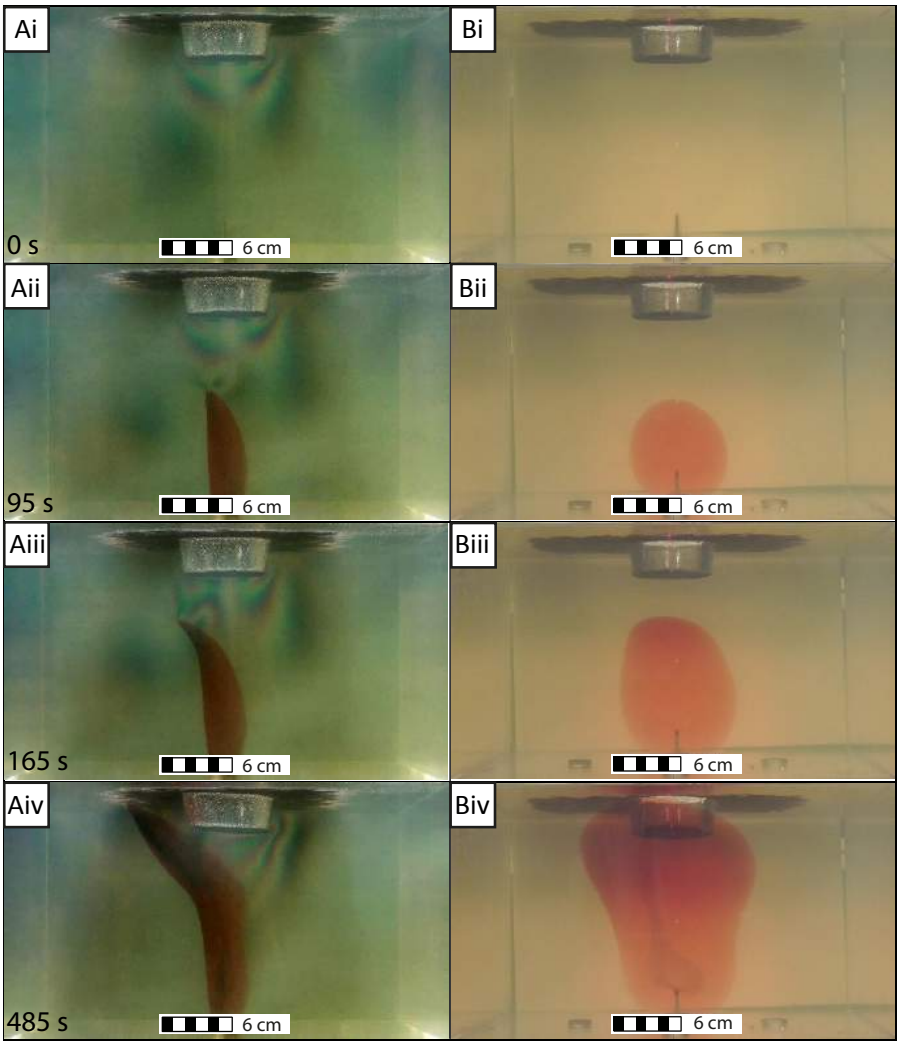

Figure 2.2: Photographs of circumferential dike development in the presence of a small caldera (Experiment AG-07, see Table 2.1): A) Polarized light ($x - z$ plane), and B) artificial light ($y - z$ plane). i) Pre-injection state, ii) Stage I: sub-vertical dike (95 s), iii) Stage II: inclined sheet (165 s), iv) Stage III: ascent to eruption (485 s). See also Supplementary Video Fig. S1.

the elastic deformation of the gelatin can be defined by the relationship between stress (σ), strain (e) and Young's modulus (E) (Gudmundsson, 2006; Merle, 2015):

$$\sigma^* = E^* e^* \tag{2.4}$$

This gives σ^* =3.0 $\times$ 10^{-6} (see Table S1). We also use the unloading pressure scale factor:

$$\sigma^* = P_U^* = \rho_r^* g^* D^* \tag{2.5}$$

where D is the caldera depth and ρ_r is the host rock density. As $\rho_r^* = 0.37$ and D^* =1.0 $\times$ 10^{-5}, this gives σ^* =3.7 $\times$ 10^{-6}. The agreement between the stress values calculated from both of these approaches (Equation 2.4 and 2.5) confirms that we have properly scaled our experiments.

2.3 Experimental methodology

2.3.1 Gelatin preparation and Young's modulus measurement

We use pigskin gelatin solids (20 Mesh, 260 Bloom; supplied by Gelita UK) prepared at 2.5 wt % by dissolving the appropriate amount of gelatin powder into water at 80 °C. The mixture preparation requires three stages: an initial stage where a concentrated mixture is created and left to cool until it reaches ~30 °C, then the remaining water is added at 5 °C to achieve a mixture temperature of ~23 °C. Some experiments required the addition of passive-tracer particles, coated in Rhodamine-B which fluoresces in laser light, to the liquid gelatin in order to apply Digital Image Correlation (DIC) analysis (Sutton et al., 1983). For this purpose, (20–50 µm) diameter fluorescent particles (peak fluorescence wavelength: 590 nm) are added to the gelatin mixture following the method described by Kavanagh et al. (2015). A clear-Perspex tank (40 cm square-base, 30 cm; Fig. 2.1) is then filled up to 23 cm height and the mixture stirred until it reaches the gel point (21 °C) to obtain a homogeneous distribution of particles in the solid gel. A caldera-like geometry is established using a round, plastic container (9 or 12 cm diameter) placed onto the gelatin surface and fixed into position relative to the central injection port in the base of the experimental tank using plastic tape. The depth of the caldera is controlled by adding water to the plastic container so that it is submerged by 4 cm depth. Subsequently, the gelatin mixture is covered with vegetable oil which is carefully poured onto its surface to inhibit dehydration, the tank is then covered with plastic wrapping and then left to cool and solidify in a refrigerator set at 5 °C for 20 hours. The tank is then taken from the refrigerator, and the plastic container is removed from the center of the gelatin solid by filling it with hot water to allow an easy release and avoid any damage at the floor and/or wall of the caldera that is formed. The oil is then carefully removed using a spoon and paper towel, and the actual depth of the caldera is measured (typically 3–4 cm, see Table 2.1).

Immediately prior to the experiment starting, the Young's Modulus of the gelatin is calculated by measuring the deflection to the gelatin surface caused by two cylindrical brass loads placed sequentially on the gelatin slab (see Supplementary Table S2 for load properties). The load is placed away from the corner of the tank to minimize any wall effects. The Young's Modulus is calculated using the following equation (Kavanagh et al., 2013):

$$E = \frac{mg(1-\nu^2)}{\Psi w} \tag{2.6}$$

where m is the load mass, g is the acceleration due to gravity, ν is the Poisson's ratio (0.5 for gelatin (e.g. Kavanagh et al., 2013; Watanabe et al., 2002), Ψ is the load diameter, and w is the deflection of the surface produced by the load. The average Young's modulus from each load placement is then reported (see Table 2.1).

2.3.2 Experiment setup

Two imaging techniques were used on the experiments to study the subsurface processes associated with dike growth and evolution using two different sets of apparatus: photoelasticity for visualizing stress (Fig. 2.1A), and tracer particle for measuring sub-surface strain and displacement (Fig. 2.1B). To create an experimental dike, a small cut is made in the bottom of the gelatin slab, which controls the orientation of the initial dike. A metal pipe with a tapered end is inserted into this slit and dyed water is injected using a peristaltic pump at a constant volumetric flow rate (Q) of $3.9 \times 10^{-7}\,\mathrm{m}^3/\mathrm{s}$. The fluid velocity ($V$) is approximated by dividing Q by the cross-sectional area of the 1 mm-diameter injection outlet. Injections were made at

Table 2.1: Model parameters, observed results, and methods applied in the experiment analysis. The experiments are listed in order of caldera diameter C and offset injection position X. The measured caldera depth D, gelatin concentration wt.%, thickness of gelatin slab H, time left to cure t, refrigerator temperature T, average Young's modulus E, and injection flux of fluid Q is reported. 'Result' corresponds to the final geometry of the intrusion classified as 'C. dike' (circumferential dike), 'Cone sheet', or 'Cone-Trans' for transitional geometries, and the final depth of bending h, and extent of intrusion d are also reported. The analysis methods used are: Polarized light (PL), vertical tip tracking (TT) and tracer particles (TP).

Experiment code	C [cm]	X [cm]	D [cm]	wt.%	H [cm]	t [hr]	T [°C]	E [Pa]	Q [m^3/s]	Result	h [cm]	d [cm]	Analysis Method
AG-07	9.0	0.0	3.31	2.5	22.6	20.5	5	2675	3.9×10^{-7}	C. dike	8.2	13.0	PL, TT
AG-13	9.0	0.0	3.78	2.5	23.1	20.5	5	2843	3.9×10^{-7}	C. dike	10.7	13.3	TP
AG-09	9.0	1.0	3.04	2.5	23.2	21.0	5	2490	3.9×10^{-7}	C. dike	8.8	13.8	PL, TT
AG-08	12.0	0.0	3.94	2.5	23.5	20.0	5	3113	3.9×10^{-7}	Cone sheet	12.1	22.4	PL, TT
AG-06	12.0	0.0	3.52	2.5	22.4	19.8	5	2779	3.9×10^{-7}	Cone-Trans	10.7	17.5	–
AG-14	12.0	0.0	4.20	2.5	23.5	21.0	5	2739	3.9×10^{-7}	Cone-Trans	11.1	16.9	–
AG-15	12.0	0.0	3.65	2.5	23.5	21.1	5	2586	3.9×10^{-7}	Cone-Trans	9.8	17.7	–
AG-16	12.0	0.0	3.77	2.5	23.2	20.5	5	2902	3.9×10^{-7}	Cone-Trans	16.8	17.5	–
AG-10	12.0	1.0	3.55	2.5	22.5	21.0	5	2401	3.9×10^{-7}	Cone sheet	12.0	23.4	PL, TT
AG-05	12.0	1.0	3.58	2.5	23.1	19.7	5	2721	3.9×10^{-7}	Cone sheet	14.3	23.7	TT
AG-17	12.0	1.0	3.95	2.5	23.2	19.7	5	2580	3.9×10^{-7}	Cone sheet	15.2	24.5	TP
AG-19	12.0	1.0	3.80	2.5	23.1	19.0	5	2964	3.9×10^{-7}	Cone sheet	15.3	24.0	TP
AG-18	12.0	2.0	3.90	2.5	23.2	22.0	5	3031	3.9×10^{-7}	Cone sheet	14.5	23.9	TP

two different offset positions (0.0 cm and 1.0 cm, relative to the center of the caldera) beneath two different caldera sizes (see Table 2.1).

2.3.2.1 Photoelasticity setup

Polarized light is known to be a useful tool to visualize the stress distribution in two dimensional elastic problems (Crisp, 1953; Watanabe et al., 2002). We use the photoelastic property of gelatin with the purpose of understanding the interaction of the local stresses with those of the pressurized experimental dike, making a qualitative description of the changes in the stress field during the intrusion development. The sequence of colored fringes represents the gradient of the differential stress ($\sigma_1 - \sigma_3$) perpendicular to the light propagation direction, and the increasing fringe order represents linearly increasing stress (Crisp, 1953); which in the experiments depend on the caldera diameter and caldera depth. The photoelasticity experimental setup (Fig. 2.1A) consists of two polarized sheets attached to the front and back walls of the tank ($x - z$ plane), and two HD video cameras positioned to record images with polarized light ($x - z$ plane, perpendicular to the dike plane) and artificial light ($y - z$ plane, parallel to the dike plane).

2.3.2.2 Tracer particle setup

The tracer particle experiment setup requires the use of a high intensity laser that was configured to fire at 1 Hz and produce a vertical, thin sheet (approximately 1 mm thick) in the gelatin slab centered on the injection point (Fig. 2.1B, see also Kavanagh et al., 2015). A New Wave Solo-PIV III Nd-YAG Laser provides 50 mJ pulses of energy between 3 and 5 ns and 532 nm wavelength. The laser firing and acquisition is controlled by Dantec Dynamic Studio software and synchronized to a MP CCD camera fitted with a 35 mm Nikon lens (Fig. 2.1B). Longpass (550 nm wavelength) filters fitted to the CCD camera allow only the fluorescent light reflected by the particles to be captured.

A 2D calibration image is required for post-experiment image processing. Prior to the experiment tank being filled with gelatin, the tank is filled with water and a white calibration plate with equally-spaced black dots of known size and spacing was aligned with the laser beam in the center of the experimental tank. An image is then captured for later data pre-processing using DIC.

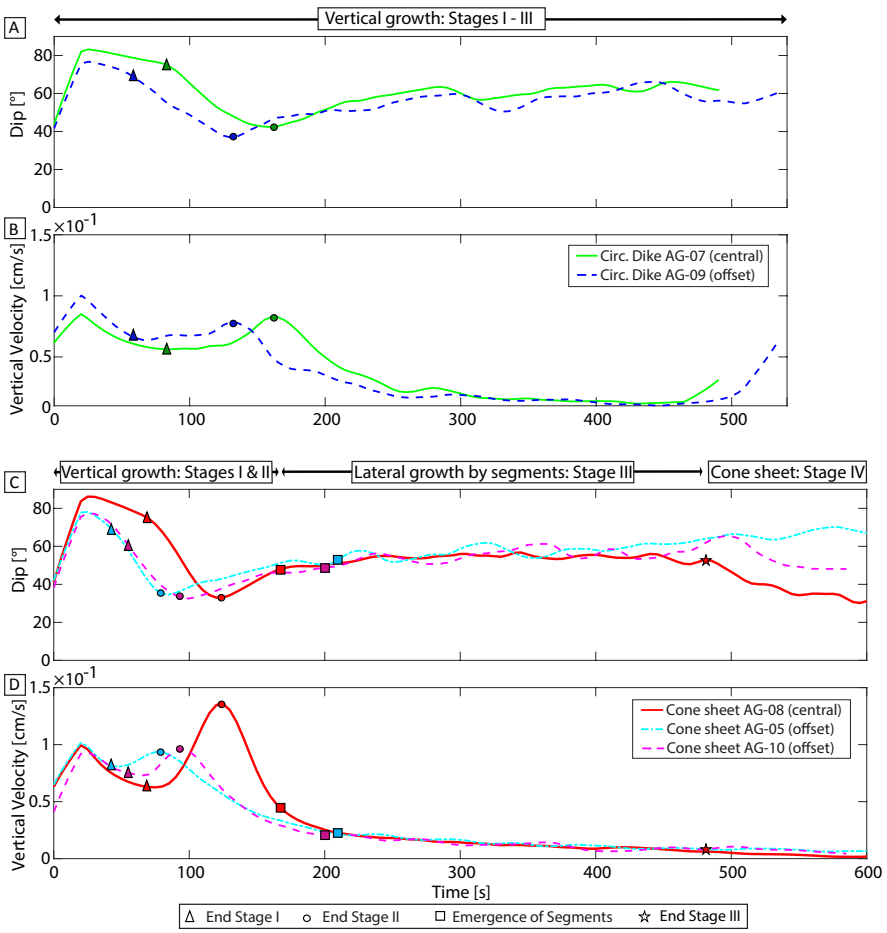

Figure 2.3: Three stages of circumferential dike (A-B) and four stages of cone sheet (C-D) growth shown by changes in Dip angle (°) and velocity (cm/s) of the vertical dike tip in the presence of the caldera. The approximate timings of stage transitions is indicated at the top of the graphs (A for circumferential dikes, and C for cone sheets). In the graphs the triangle indicates the end of Stage I (sub-vertical dike), the circle indicates the end of Stage II (inclined sheet), and the star indicates the end of Stage III (lateral growth by arcuate segments in cone sheet emplacement). Stage III shows the ascent to eruption in circumferential dike emplacement. The Stage III of cone sheet growth produces laterally propagating arcuate segments (the time of their emergence is indicated by a square) and these join at the start of Stage IV to complete the geometry.

2.3.3 Data processing

In order to study the evolution of the growing intrusion geometry, we first track the vertical dike tip trajectory in the $x-z$ plane using video images from the polarized light setup (Fig. 2.1A). This is conducted at intervals of one frame every 5 seconds using the free Java software Tracker vs 4.10.0 (Brown, 2012). The coordinate origin is set as the top of the needle in the calibrated model, and the position of the vertical dike tip is manually tracked over time. The velocity of the dike tip, and the local dip angle relative to horizontal, is simultaneously computed.

DIC is then used to quantify the sub-surface displacement vectors and total strain due to the dike intrusion, at an interval of one image every 5 seconds (0.2 Hz), by using the commercial image analysis tool StrainMaster, implemented in the DaVis software package vs. 8 (LaVision). The calibration image captured prior the experiment is imported into DaVis in a pre-processing stage to scale the results in dimensional units. This process converts the scale from pixels to distance units, and corrects any distortions through the de-warping function. The incremental strain is then calculated by implementing a 'Least Square Matching' algorithm (LSM-algorithm), which operates using an optical flow approach (Fleet and Weiss, 2010). Three seeding points are defined within the reference image, and these are static win-

dows of initial size 121 x 121 pixels that experience no deformation in the experiment. The interrogated area then increases in size with each iteration implementing the 'region grow' algorithm. Outlier and Smoothing filters are then applied, and a mask function is added to exclude the tank walls and caldera cavity from the analysis. The incremental strain is summed to give the total strain. For very small displacement gradients, the strain tensor values are defined by Cauchy's infinitesimal tensor:

$$\epsilon_{ij} = \frac{1}{2}\left(\frac{\partial v_i}{\partial x_j} + \frac{\partial v_j}{\partial x_i}\right) \tag{2.7}$$

where v is the vector component and x the spatial axis. As the experiment observations are carried out in two dimensions ($x - z$ or $y - z$ plane), the lineal deformation in the x or y-direction and in the z-direction are determined by the normal strain components:

$$\epsilon_{xx} = \frac{\partial u}{\partial x} \quad \text{or} \quad \epsilon_{yy} = \frac{\partial v}{\partial y} \tag{2.8}$$

and,

$$\epsilon_{zz} = \frac{\partial w}{\partial z} \tag{2.9}$$

Thus, the shear strain is given by:

$$\epsilon_{xz} = \epsilon_{zx} = \frac{1}{2}\left(\frac{\partial u}{\partial z} + \frac{\partial w}{\partial x}\right) \quad \text{or} \quad \epsilon_{yz} = \epsilon_{zy} = \frac{1}{2}\left(\frac{\partial v}{\partial z} + \frac{\partial w}{\partial y}\right) \tag{2.10}$$

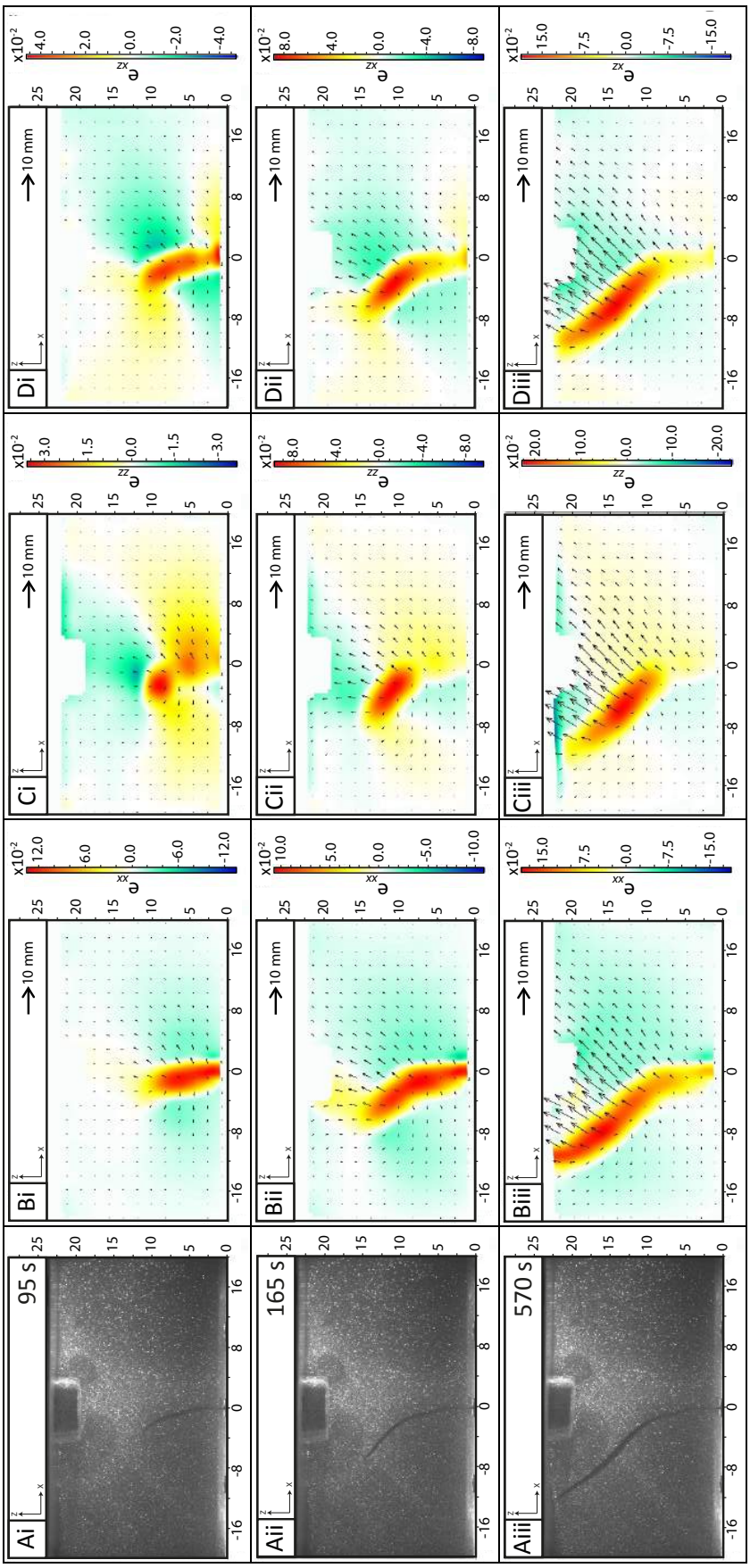

Figure 2.4: Three stages of circumferential dike development in the presence of a small caldera, imaged in the $x-z$ plane, with sub-surface total strain (color maps) and displacement (vector arrows) calculated using DIC (Experiment AG-13, see Table 2.1): i) Stage I: initial sub-vertical dike (95 s), ii) Stage II: inclined sheet (165 s), and iii) Stage III: ascent to eruption (570 s). A) Dewarped experimental images, B) horizontal total normal strain e_{xx}, C) vertical total normal strain e_{zz}, and D) total shear strain component e_{xz} are shown. The red color represents extensional deformation in the normal components and anticlockwise rotational deformation in the shear component. See also Supplementary Video Fig. S1.

2.4 Results

In total 19 experiments were conducted to explore the influence of caldera unloading and injection offset on dike propagation, geometry and growth. The experimental results are grouped into two end-member geometries: circumferential dikes and cone sheets, however transition geometries are also observed (see Table 2.1). We detail our experimental observations and results below using representative experiments as examples grouped by their end-member geometries.

2.4.1 Circumferential dikes

Circumferential dikes are formed in our experimental series only in the presence of a small caldera (Table 2.1) and in three stages: 1) sub-vertical dike, 2) inclined sheet, and 3) ascent to eruption (see Supplementary Video Fig. S1). When the injection position is offset, these three stages occur earlier and their transitions happen at greater depth than when the injection is central. The details of each stage of circumferential dike formation and eruption are now described.

2.4.1.1 Stage I: sub-vertical dike

Polarized light shows the unloading stress field induced by the caldera in the pre-injection state (Fig. 2.2Ai). When the injection starts, a vertical dike is produced (Fig. 2.2Aii and 2.2Bii) creating its own stress field that is focused in a small region around the dike tip and intensifying in magnitude and extent as the dike grows upwards until it reaches a vertical length of 9.2 cm by the end of this stage (Fig. 2.2Aii). At this time, the dike grows near vertical with a dip angle of approximately 80° (Fig. 2.3A). During this stage there is an initial rapid acceleration followed by velocity deceleration (Fig. 2.3B). The DIC analysis (Fig. 2.4) shows the displacement vectors are small and radiate out from the entire dike length, and the total normal strain component e_{xx} (Fig. 2.4Bi) is large (14×10^{-2}) compared with the vertical ($e_{zz} = 4 \times 10^{-2}$, Fig. 2.4Ci) and shear components ($e_{xz} = 4.5 \times 10^{-2}$, Fig. 2.4Di).

2.4.1.2 Stage II: inclined sheet

In Stage II, the dike moves away from the caldera center with a maximum height of 12.8 cm in the end of this stage (Fig. 2.2Aiii and 2.2Biii). In terms of stress, this stage is distinguished by the colored fringes from the dike visually interacting with those of the caldera (Fig. 2.2Aiii). It coincides with a rapid decrease in the dip angle (from 80° to 40°, Fig. 2.3A) and a slight acceleration of the vertical tip (Fig. 2.3B). Overall the direction of displacement is upwards and towards the caldera, and its maximum amplitude is less than 5 mm (Fig. 2.4Aii, Bii, Cii). The total strain during Stage II (Fig. 2.4Aii) has slightly decreased in the normal horizontal strain (e_{xx} down to 11×10^{-2}), but has increased in the vertical and shear components (e_{zz} and e_{xz} up to 10×10^{-2} and 9×10^{-2}, respectively); e_{xx} is distributed along the length of the vertical dike and inclined limb (Fig. 2.4Bii), whereas there are local concentrations in e_{zz} (Fig. 2.4Cii) and e_{xz} (Fig. 2.4Dii) at the tip.

2.4.1.3 Stage III: ascent to eruption

The final stage of circumferential dike development is acceleration to eruption to form a circumferential fissure (Fig. 2.2Aiv and 2.2Biv). In our experiments all circumferential dikes erupted. During this final stage, there is no visual interaction between the dike stress field and that from the caldera. The dike dip angle gradually increases to 60° and then broadly maintains this (Fig. 2.3A). The vertical tip decelerates gradually, but then accelerates towards eruption (Fig.

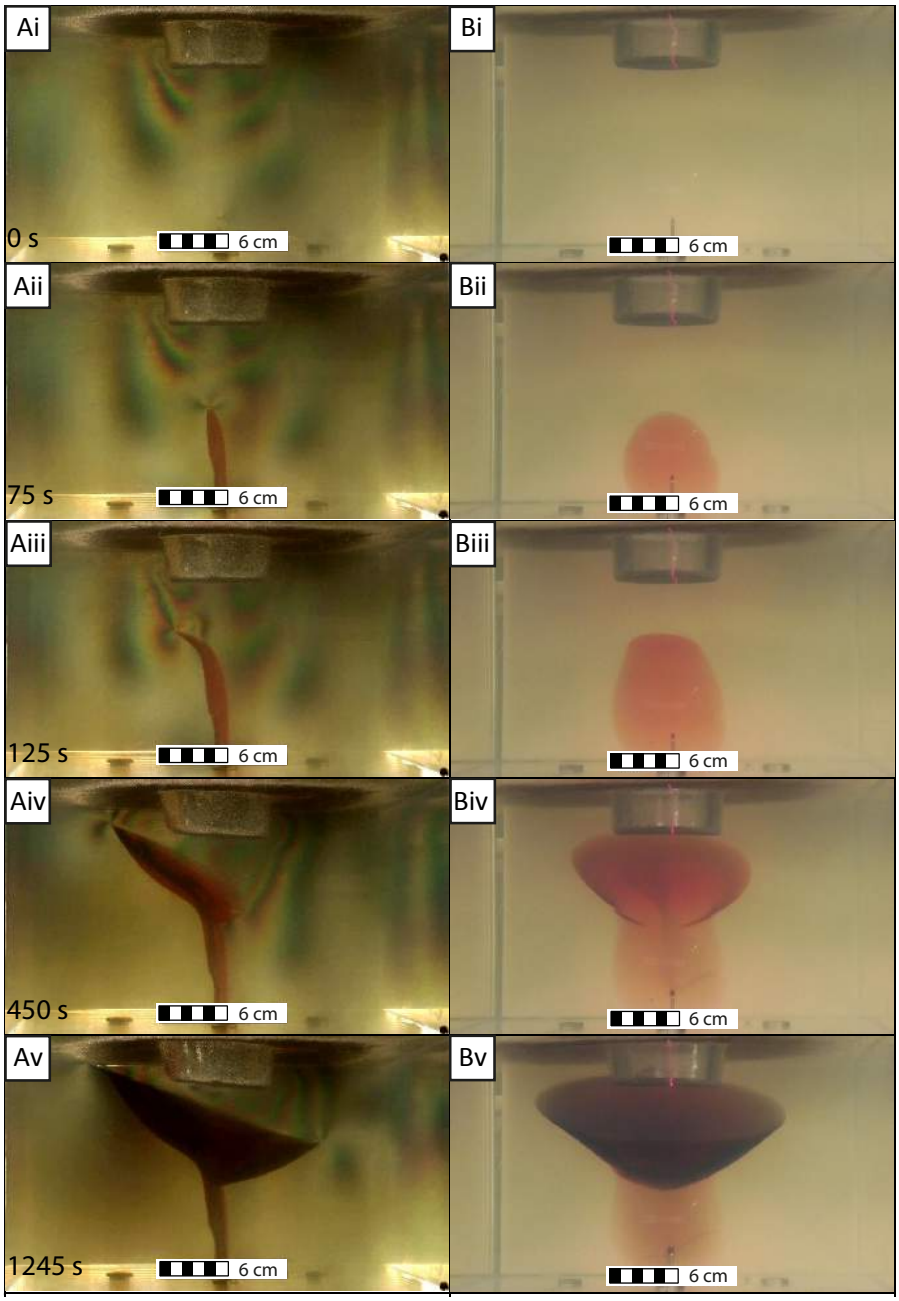

Figure 2.5: Photographs of cone sheet development in the presence of a large caldera (Experiment AG-08, see Table 2.1): A) Polarized light ($x-z$ plane), B) artificial light ($y-z$ plane). i) Pre-injection stress state, ii) Stage I: sub-vertical dike (75 s), iii) Stage II: inclined sheet (125 s), iv) Stage III: lateral growth by en echelon arcuate segments (450 s), and v) Stage IV: cone sheet completion with no eruption (1245 s). See also Supplementary Video Fig. S2.

2.3B). The maximum opening of the inclined limb of the dike is 7.8 mm thick (Fig. 2.4Aiii), generating the largest magnitude of the total displacement vectors which are oriented towards the caldera (Fig. 2.4Biii, Ciii, Diii). The total strain just before eruption produces the maximum deformation during injection, producing visible uplift of the caldera floor. The largest component of total strain is vertical at $e_{zz} = 22.5 \times 10^{-2}$ (Fig. 2.2Ciii), with similar values in total horizontal and shear strain (e_{xx} and e_{xz} up to 17.5×10^{-2}; Fig. 2.4Biii and 2.4Diii).

2.4.2 Cone sheets

Cone sheets were formed in the presence of the large caldera six times (see Table 2.1), and transitional geometries (partial cone, but with dike eruption) were formed four times. The cone sheets are formed in four stages (see Supplementary Video Fig. S2), with the first two stages being identical to the circumferential dike formation. Stage I is a sub-vertical dike, Stage II is an inclined sheet, Stage III is lateral growth, and Stage IV is cone sheet completion. Similarly to the circumferential dike, when the injection position is offset this results in earlier and deeper transitions between the stages.

2.4.2.1 Stage I: sub-vertical dike, and Stage II: inclined sheet

The pre-injection stress pattern induced by the large caldera shows more fringes that extend to greater depths in the gelatin slab (Fig. 2.5Ai) compared to the small caldera (Fig. 2.2Ai). Similarly to the small caldera experiments, the first two stages of cone sheet growth are: 1) sub-vertical dike (Fig. 2.5Aii, Bii), which then changes dip and develops into 2) an inclined sheet (Fig. 2.5Aiii, Biii). During Stage I we observe a moderate decrease in the dip angle from 85° to 75° (Fig. 2.3C) and velocity deceleration (Fig. 2.3D), as the dike reaches 9.3 cm height. During Stage II the dike changes dip angle from 75° to 35°, accelerates from 0.6 cm/s to 1.4 cm/s, and reaches 12.6 cm height by the end of Stage II.

The total displacement and total strain (normal and shear components) of cone sheet growth are measured in the $x-z$ plane (Fig. 2.6) and $y-z$ plane (Fig. 2.7). During Stages I and II, the majority of the propagation is out of the $y-z$ plane and so only minor displacements and total strain are recorded in this view (Fig. 2.7Ai, Bi, Ci, Di, Aii, Bii, Cii, Dii). Stage I of cone sheet formation (Fig. 2.6Ai) has maximum total strain in the horizontal normal component ($e_{xx} = 11 \times 10^{-2}$, Fig. 2.6Bi), with this distributed across the whole dike, with lower vertical and shear total strain components (e_{zz} and $e_{xz} = 4 \times 10^{-2}$; Fig. 2.6Ci and 2.6Di). In contrast, Stage II has maximum total strain in the vertical normal component ($e_{zz} = 12 \times 10^{-2}$; Fig. 2.6Cii), with lower horizontal and shear total strain components (e_{xx} and $e_{xz} = 8 \times 10^{-2}$; Fig. 2.6Bii and 2.6Dii). There are also similar displacement vectors to those observed in Stages I and II of the circumferential dike formation, with low magnitude displacements (< 5 mm in Stage I, and 5–10 mm in Stage II) radiating out from the dike.

2.4.2.2 Stage III: lateral dike growth by arcuate segments

Following initial vertical dike growth (Stage I) and then divergence to a dipping dike (Stage II), a new direction of intrusions establishes at the turning point h (see Table 2.1). Stage III of cone sheet growth is marked by the Stage II dike dip angle stabilizing at approximately 60° (Fig. 2.3C), and the vertical growth rapidly decelerating indicating an arrested dike (Fig. 2.3D). Two circumferential and laterally-propagating en echelon arcuate segments then form close to the turning point (Fig. 2.3C), specifically from the lower part of the inclined sheet (Fig. 2.5Aiv and 2.5Biv). In the $x-z$ plane, the total displacement vectors increase in magnitude relative to Stage II to be > 10 mm, and the maximum displacement continues being oriented radially towards the caldera (Fig. 2.6Biii, Ciii, Diii). The largest total strain is the vertical normal component ($e_{zz} = 37.5 \times 10^{-2}$; Fig. 2.6Ciii) followed by the shear component ($e_{xz} = 23 \times 10^{-2}$; Fig. 2.6Diii) and horizontal normal component ($e_{xx} = 20 \times 10^{-2}$; Fig. 2.6Biii). In Stage III, the cone sheet emerges in the $y-z$ plane as the inclined, laterally-propagating arcuate segments penetrate the laser sheet (Fig. 2.7Aiii). This produces maximum total displacement of 10 mm (which is slightly less than measured in the $x-z$ plane), and a maximum vertical deformation ($e_{zz} = 12 \times 10^{-2}$; Fig. 2.7Ciii) compared to horizontal ($e_{yy} = 7 \times 10^{-2}$; Fig. 2.7Biii) and shear

components ($e_{yz} = 9 \times 10^{-2}$; Fig. 2.7Diii); which are all lower than strains measured in the $x - z$ plane.

2.4.2.3 Stage IV: cone sheet completion

The fourth and final stage of cone sheet formation is the completion of the cone geometry (Fig. 2.5Av and 2.5Bv). This occurs when the laterally-propagating arcuate segments of Stage III join to create a circular profile in the horizontal plane without erupting. The final cone sheet geometry has a range of forms spanning 'cocktail-glass', 'bowl' and 'trumpet' forms (Fig. 2.5, 2.6 and 2.7), in agreement with cone sheet geometries described by Burchardt et al. (2018). In transitional geometries, Stage III still produces the lateral sub-surface arcuate segments but they do not join. Instead, at some moment the vertical ascent of the dike is reinitiated, at the location where it first became arrested, and this results in an eruption. Therefore, transitional geometries do not reach Stage IV and have growth behavior and a final geometry that is intermediate to the circumferential dike and cone sheet.

Stage IV has a slight decrease in the dip angle starting immediately after the arcuate segments join (Fig. 2.3C), and the velocity decrease is maintained (Fig. 2.3D). The thickest opening of the inclined sheet was 13.63 mm (Fig. 2.6Aiv), which produced displacements greater than 10 mm focused directly beneath and towards the caldera (Fig. 2.6Biv, Civ, Div). The maximum strain occurs in the vertical normal component, reaching $e_{zz} = 55 \times 10^{-2}$ in the $x - z$ plane (Fig. 2.6Civ) and $e_{zz} = 50 \times 10^{-2}$ the $y - z$ plane (Fig. 2.7Civ). The total strain is up to $e_{xx} = 20 \times 10^{-2}$ and $e_{yy} = 12 \times 10^{-2}$ in the horizontal components (Fig. 2.6Biv and 2.7Biv, respectively), and $e_{xz} = 35 \times 10^{-2}$ and $e_{yz} = 22.5 \times 10^{-2}$ in the shear component (Fig. 2.6Div and 2.7Div, respectively).

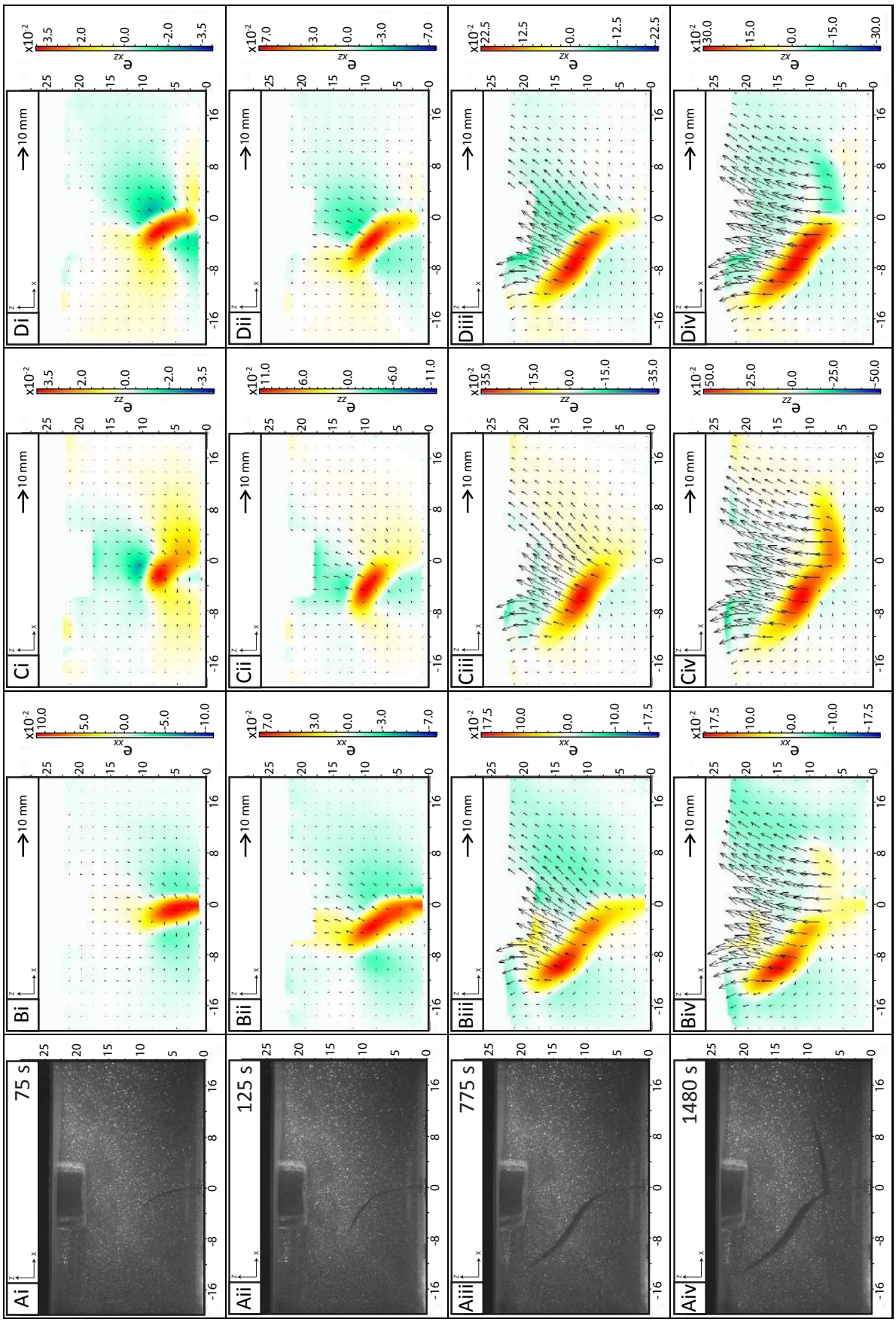

Figure 2.6: Cone sheet development in the presence of a large caldera, viewed in the $x-z$ plane, with sub-surface total strain (color maps) and displacement (vector arrows) calculated using DIC (Experiment AG-17, see Table 2.1). Four stages of cone sheet development are shown: i) Stage I: initial sub-vertical dike (75 s), ii) Stage II: inclined sheet (125s), iii) Stage III: arrest and increased opening of the inclined sheet (775 s), and iv) Stage IV: cone sheet geometry completion with no eruption (1480 s). A) Dewarped experimental images, B) horizontal total normal strain e_{xx}, C) vertical normal strain e_{zz}, and D) shear strain component e_{xz}. The red color represents extensional deformation in the normal components and anticlockwise rotational deformation in the shear component. See also Supplementary Video Fig. S3.

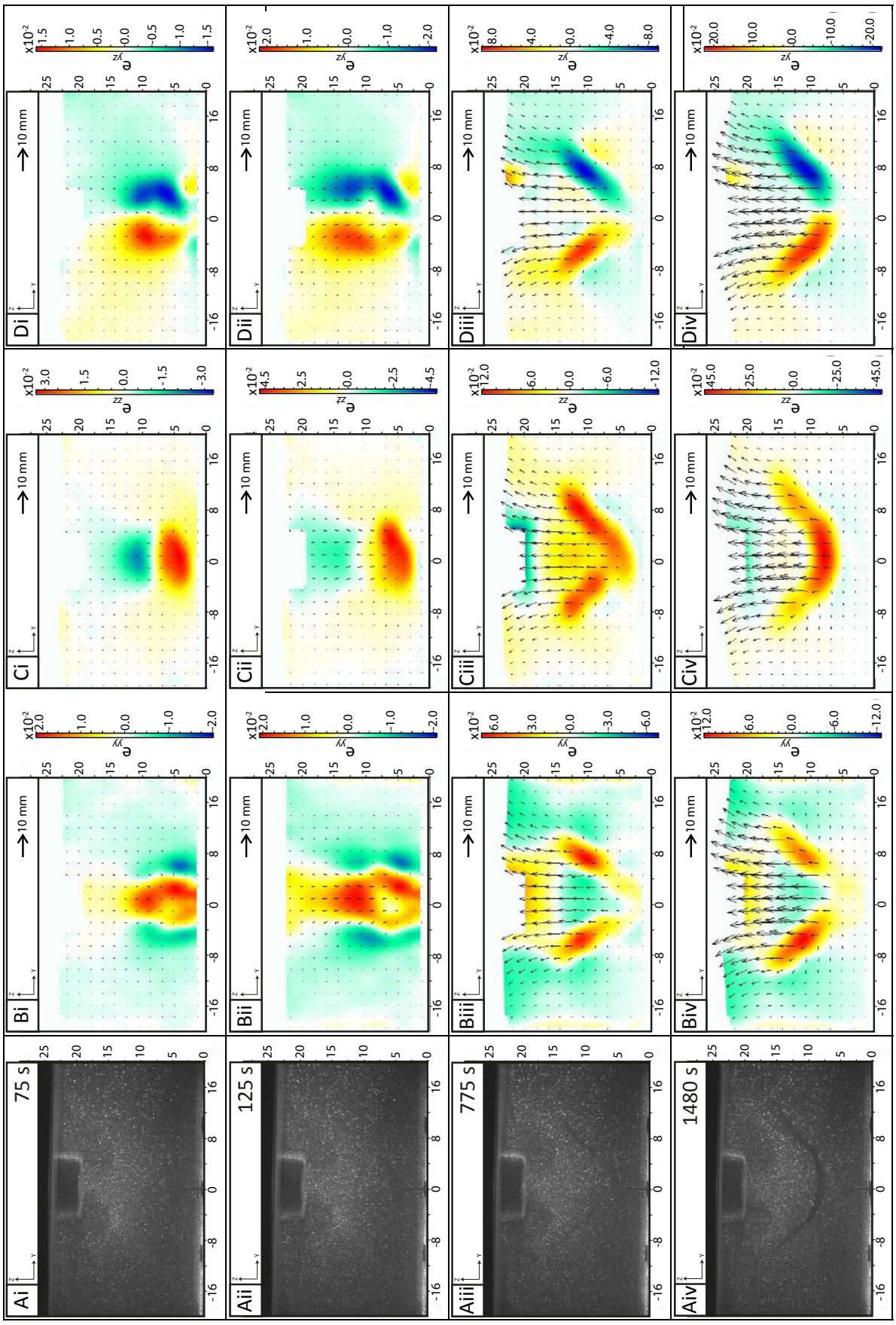

Figure 2.7: Cone sheet development in the presence of a large caldera, viewed in the $y-z$ plane, with sub-surface total strain (color maps) and displacement (vector arrows) calculated using DIC (Experiment AG-19, see Table 2.1). Four stages of cone sheet development are shown: i) Stage I: initial sub-vertical dike (75 s), ii) Stage II: inclined sheet (125 s), iii) Stage III: arrest and increased opening of the inclined sheet (775 s), and iv) Stage IV: cone sheet geometry completion with no eruption (1480 s). A) Dewarped experimental images, B) horizontal normal strain e_{yy}, C) vertical normal strain e_{zz}, and D) shear strain component e_{yz}. The red color represents extensional deformation in the normal components and anticlockwise rotational deformation in the shear component. See also Supplementary Video Fig. S4.

2.5 Discussion

2.5.1 Circumferential dike or cone sheet? Comparison with previous experiments

Our experimental series has produced a spectrum of thin sheet-like intrusions, all of which were parallel to the circular caldera, and with end-member geometries of an erupted circumferential dike (Fig. 2.2) and an intrusive cone sheet (Fig. 2.5). The development of these different end-member geometries was similar. Both circumferential dikes and cone sheets propagated at dip angles which reached almost vertical (Fig. 2.3A, C; Fig. 2.8), but the circumferential dikes dip angle ranged from ~40° compared to 30° for the cone sheets (Fig. 2.8). These dip values are similar to those in nature, for example the trachytic to phonolitic cone sheets of the Tejeda Complex, Gran Canaria which intruded intra-caldera deposits (Schirnick et al., 1999), and the mafic cone sheets of the Ardnamurchan central igneous complex, NW Scotland which intruded into the base of an ancient basaltic volcano (Richey and Thomas, 1930).

Circumferential dikes and cone sheet geometries have been studied in previous laboratory experiments. Using a granular material to represent the properties of the brittle crust and a flat topography, Galland et al. (2014) found that cone sheets form when the magma source is shallow with respect to the intrusion's width, or when the injection velocity or viscosity is high. Corbi et al. (2016) created buoyant air-filled dikes in gelatin edifices which had a topographic depression simulating a caldera. Similarly to our experiments, they observed that the unloading stress field leads to the formation of circumferential dikes. They found that magma buoyancy plays a key role in the dike geometry and the eruption location, and our experiments support this work even though we did not include a volcanic edifice. When the unloading stresses were particularly large we found this was able to stop eruption and cause a full-cone sheet to develop, whereas Corbi et al. (2016) did not form cone sheets.

The caldera diameter was the key parameter in determining the outcome of our experiments: circumferential dikes always developed in the presence of the 9 cm caldera diameter, and a spectrum of transitional to cone sheet geometries were associated with the 12 cm caldera diameter topography (see Table 2.1). Following the approach of Galland et al. (2014), we have analyzed our experiments further by considering the outcomes related to dimensionless Pi-numbers (Fig. 2.9). The first Pi-number is geometric:

$$\Pi_1 = \frac{h}{d} \tag{2.11}$$

where h is the depth at which bending of the dike first occurs, and d is the horizontal extent of the intrusion (see Table 2.1). The second Pi-number considers the fluid-flow properties and extent of unloading stress relative to lithostatic loading:

$$\Pi_2 = \frac{\mu\nu}{d\,(P_L - P_U)} \tag{2.12}$$

where μ is the fluid viscosity, ν is the velocity of the fluid, P_L is the lithostatic pressure, and P_U is the unloading pressure due to the presence of the caldera (see Supplementary Table S1). Fig. 2.9 shows our experiments occupy three distinct regions in this non-dimensional space, with cone sheets forming at low Π_1 and Π_2 values, circumferential dikes forming at high Π_1 and Π_2 values, and transitional geometries forming at intermediate Π_1 and Π_2 values. Geophysical constraints on parameter values that would populate the Π_1 and Π_2 equations in nature (see Supplementary Table S1 for example) suggest that magnitudes of Π_1 and Π_2 in nature are high compared to our experiments. For example, at Rabaul Volcano in Papau New Guinea (Kennedy et al., 2018) the corresponding Π_1 value is 1.5 and the Π_2 value is 3×10^{-5}. This

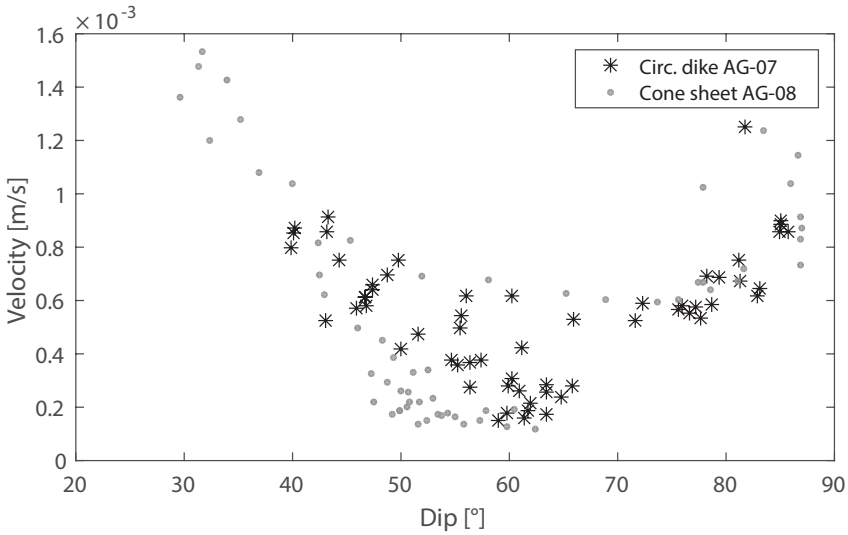

Figure 2.8: The local dip angle relative to vertical ascent velocity for circumferential dike (AG-07) and cone sheet development (AG-08). See Table 2.1 for experimental conditions.

means, according to our models, the most likely intrusion form geometry at Rabaul Volcano would be circumferential dikes.

2.5.2 Circumferential dikes and cone sheets in nature

The Ardnamurchan cone sheets are perhaps the most-famous of all cone sheets, but there are contrasting models to explain their origin. Burchardt et al. (2013) used 3D projections to propose that the Ardnamurchan cone sheets originate from a single, elongated and temporally evolving magma chamber. This model is in contrast to Richey and Thomas (1930) who originally proposed three centers, and Magee et al. (2012) who proposed lateral magma flow from an adjacent magmatic source in a compressional stress field. We show experimentally that local unloading stresses can cause an initially vertical dike originating from directly beneath a caldera to stall in the crust and grow laterally to form a cone sheet. This is relevant to the Ardnamurchan central igneous complex, as our model does not require input from neighboring systems to build a cone sheet (in contrast to Magee et al., 2012) and does not make assumptions about the nature of the magma chamber at depth (as is the case in Burchardt et al., 2013). Instead we demonstrate that such geometries could be formed purely due to local unloading stresses. It is unclear whether or not there was a caldera present at the time when the Ardnamurchan cone sheets formed (Brown and Bell, 2006), but calderas are thought to have been present in the region at the time of intrusion (Troll et al., 2000).

Articulated magma intrusion geometries, made up of circumferential sub-vertical dikes close to the caldera rim which dip towards sub-horizontal sills below the caldera floor, have often been needed to fit crustal deformation data at calderas. Geodetic studies of magma intrusion associated with the 2005 circumferential fissure eruption of Fernandina volcano in the Galapagos (summit caldera: 5 km x 6.5 km) presented pre-eruptive (Bagnardi et al., 2013) and co-eruptive (Chadwick et al., 2011) surface deformation that was recorded using Interferometric synthetic aperture radar (InSAR). Inverse models of the data suggested the intrusion which fed the eruption had a curved and circumferential laminar geometry and originated from a sill, thus showing similar geometry to our experimental circumferential dikes. The continuous vertical growth and final eruption of our experimental circumferential dike agrees well with the Chadwick et al. (2011) model of intrusion leading to the 2005 eruption of Fernandina (Corbi et al., 2015).

Overall, we suggest that the common modeling assumption of flat geometries, such as planar sheets opening dislocations or cracks, the availability of suitable analytical solutions, and the need to keep the number of model parameters low, may have limited our ability to recognize curved geometries such as those we propose here. Deep cone sheet intrusions may produce low-amplitude uplift that may be a satisfyingly fit for pressurized sub-horizontal cracks below the caldera floor, which is a feature ubiquitously found by geophysical and geodetic surveys at calderas worldwide.

2.5.3 Arcuate segment development and lateral dike growth

Lateral propagation of a circumferential dike has been evidenced by geological records, but rarely from geophysical monitoring. Geological evidence of lateral flow during cone sheet development was found by Magee et al. (2012) using magnetic fabrics preserved within crystalline cone sheets. However, they interpreted this as evidence of magma being sourced from an adjacent magma chamber, but our results show that such crystalline fabrics could result from a cone sheet intrusion whose magma source was directly beneath an unloaded topography. Geophysical evidence of lateral propagation of a circumferential dike firstly came from the 1989 seismic swarm at Mammoth Mountain, Long Valley caldera, California (Prejean et al., 2003) where earthquake hypocenter migration into a ring structure was interpreted as fluid which triggered seismicity on a ring fault, but it would be also consistent with lateral propagation 0.4 km/month of a conical opening crack filled with magma or other magmatic fluid evidenced by the migration of seismicity over time. Therefore, our model observations are support the interpretation of lateral magma migration recorded by the seismic data. Secondly, reconstructing ground displacement at the pre-eruptive phase in Monte Nuovo, Campi Flegrei caldera (1935 AD), Di Vito et al. (2016) recognized a circumferential source extending from the center, eccentrically towards the caldera rim, that transfers felsic magma laterally to feed eruptions at the caldera margin, which has been the eruptive magma path for the last $5ka$. In the laboratory, both circumferential dikes and cone sheets had their lowest ascent velocities when the dikes were growing at intermediate dip angle 40–80 °C, and their highest velocities coincided with the lowest and highest dip angles (Fig. 2.8).

Circumferential lateral propagation was present in the growth of our experimental cone sheet intrusions by the establishment of laterally propagating arcuate segments, and the cone sheet geometry initiated at the bending location of the dike (h). We interpret the development of en echelon arcuate segments in our experiments to be associated with stress rotation, due to the influence of the caldera stress field which causes lateral propagation and crack opening under mixed-mode loading (Mode I and Mode III) thus creating shear at the growing tip (Pollard et al., 1982).

2.5.4 Limitations of our models

Our experimental approach was not to reproduce the natural complexity of magma intrusion in the presence of calderas, but to focus on the effect of the magnitude and extent of the unloading stress on the type of intrusion formed and how it grew. Inelastic host-rock deformation was not considered in our models, and yet this may be important in the shallow crust and in a caldera setting in particular, where rocks may have been damaged due to the caldera-forming process (see for review Galland et al., 2018). On a local scale, an inelastic host-rock rheology may dampen the transference of rock deformation signals, due to local compaction and grain rotation, and may increase the possibility of dike segmentation occurring. We did not consider rock layering, yet volcanic settings are likely to be mechanically variable, and previous work has demonstrated how rigidity layering can promote the formation of sills beneath a rigid

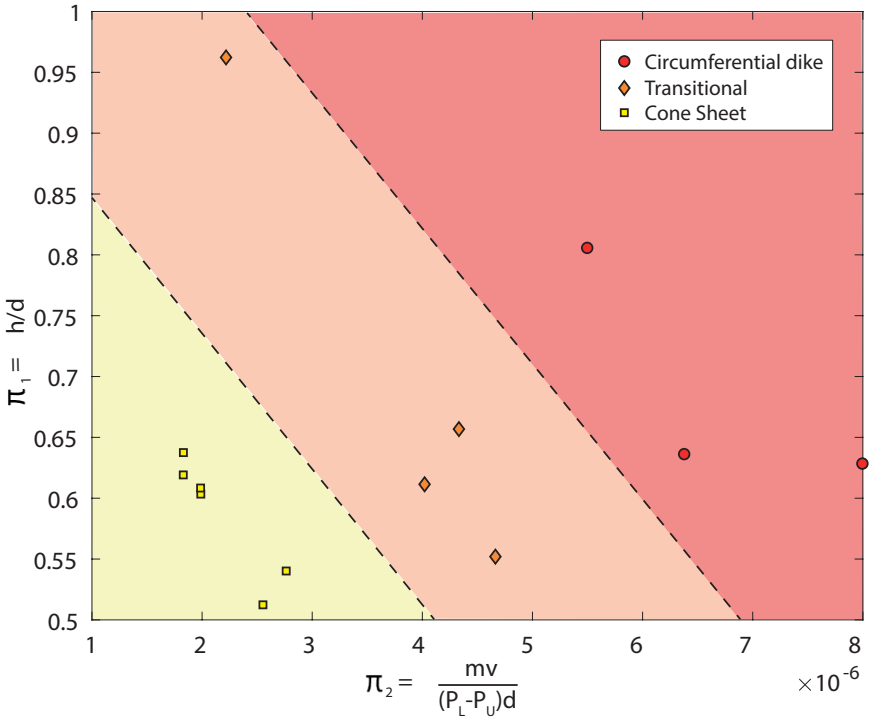

Figure 2.9: Dimensionless phase diagram presenting the range of intrusion geometries formed in the experiments: circumferential dikes (red circles), Transitional geometries (orange diamonds) and cone sheets (yellow squares). The dimensionless parameters represent the model conditions $\Pi_1 = h/d$ and $\Pi_2 = \mu\nu/(P_L - P_U)d$. The cone sheets and circumferential dikes plot in distinct fields with transitional geometries formed in the intermediate zone.

layer (Kavanagh et al., 2006). Calderas also have fault systems that are likely to influence magma propagation (Browning and Gudmundsson, 2015). Recent experimental work using particle image velocimetry (Kavanagh, 2018; Kavanagh et al., 2018b) to model magma flow in dikes is challenging existing dike propagation models, and demonstrates how consideration of the host rock deformation and the magma flow dynamics are needed to develop the next generation of dike emplacement models. The additional impacts of faults, mechanical layering and magma flow dynamics on magma propagation in caldera settings should be the focus of future multidisciplinary and experimental work.

2.6 Conclusion

We produced experimental circumferential dikes which erupted, and intrusive cone sheets that grew by lateral propagation of en echelon arcuate dike segments. Both originated from a single dike beneath a caldera-like topography in an elastic material. We also formed transitional geometries that were intermediate to these end-member forms. Circumferential dike and cone sheet intrusion dynamics occurred in stages of development which are reflected by their geometric (dip angle), kinematic (velocity) and dynamic (stress and strain) evolution. We identified 3 stages of circumferential dike development (I. Sub-vertical dike; II. Inclined sheet; III. Ascent to erupt) and 4 stages of cone sheets (I. Sub-vertical dike; II. Inclined sheet; III. Lateral growth by arcuate en echelon dike segments, and IV. Completion of the cone sheet). Our results show there are many similarities between the dynamics of cone sheets and circumferential dikes. Our summative dimensionless phase diagram suggests that their occurrence can be related to geometric, fluid flow, and lithospheric unloading conditions.

We have proposed a new origin and emplacement for cone sheets that originate from purely vertical dike growth. However, our analysis suggests that conditions in nature seem to be unfavorable for cone sheets to form due to crustal unloading in a caldera setting, and that circumferential dikes and transitional-cone sheet geometries are more likely to form. Our models can help the interpretation of InSAR, GPS and seismic data from active systems, and contribute to the production of more accurate models of magma sources beneath calderas. An important new implication of our models for volcano monitoring is that the conditions for circumferential dike formation appear to be more prevalent in nature. Significantly, it may not be possible to distinguish whether an intrusion will be likely to erupt or not until it has propagated into the shallow crust, which is when it is also likely to be propagating at its fastest rate. This new understanding of magma intrusion dynamics will help to reconstruct the history of ancient calderas, and to forecast unrest and eruptions in active ones.

Chapter 3

Seismic activity during the 2013 – 2015 intereruptive phase at Lascar volcano, Chile

Abstract

In addition to enabling the physical processes of volcanic systems to be better understood, seismology has been also used to infer the complexity of magma pathways and plumbing systems in steep-sided andesitic and stratovolcanoes. However, in these volcanic environments, the application of seismic location methods is particularly challenging and systematic comparisons of common methods are lacking. Furthermore, little is known about the characteristic seismicity and deep structure of Lascar volcano, one of the most historically active volcanoes in northern Chile known to produce VEI-4 eruptions. To better understand the inner processes and deep structure of Lascar, the local broadband seismic monitoring network was densified during a temporal installation in 2014–2015. Herein, we focus on the local seismicity during the 2014–2015 unrest episode, during which we recorded numerous seismic events mainly classified as long-period (LP) type, but also denote volcano-tectonic (VT) activity. Specifically, a long-lasting phase of LP activity is observed over a period of ~14 months that starts in tandem with a pulse of VT activity. The LP rate and amplitude are modulated over time; they are lower in the initial phase, rise during the intermediate period from October 2014 to July 2015, and finally slowly decay while approaching the eruption time. The location of LPs is challenging due to the typical lack of clear seismic onsets. We thus encompass this problem by comparing a broad range of different standard and novel location techniques to map the source region of LPs by fitting the amplitude decay, polarization patterns, coherence of characteristic functions and cross-correlation differential times. As a result, we principally constrain LP locations within the first 5 km depth below the summit extending downward along a narrow, conduit-like path. We identify different regions of complexity: VTs dominate at depth, both VTs and LPs cluster in an intermediate depth region (down to 1.5 km), suggesting a change in the plumbing system geometry, and LPs dominate the shallowest region. Based on these results, we infer the presence of a sub-vertical conduit extending down to a depth of ~5 km, and a region of path divergence, possibly accommodating a magma plumbing system, at a depth of ~3 km beneath the volcano summit. Identifying the locations of complexities in the magma pathways at Lascar may help identify future unrest. The results are compared with independent observations, demonstrating the strength of the location method used herein that will be tested at volcanoes elsewhere. [1]

[1] Originally published as: Gaete, A., Cesca, S., Franco, L., San Martin, J., Cartes, C., Walter, T. R. (2019): Seismic activity during the 2013–2015 intereruptive phase at Lascar volcano, Chile. Geophysical Journal International, 219, 449-463. doi:10.1093/gji/ggz297

3.1 Introduction

Volcanic eruptions are fed by magma, which is stored within and transported through plumbing systems formed by extensive networks of reservoirs and conduits beneath volcanoes. The physical processes that produce eruptions and their associated dynamics can be better understood by studying these plumbing systems from multiple perspectives through a variety of disciplines, including geology and structural analysis, petrology and geochemistry, geophysics, and geodesy and modeling (Burchardt and Galland, 2016). In particular, some volcanoes, especially basaltic ones, often display clear internal structures featuring dikes, rift zones and magma chambers (Dzurisin, 2007), whereas the characteristics of explosive and often dome-building volcanoes are difficult to reconcile due to the absence of major storage regions and/or scattering effects observed in geophysical data (Wegler and Lühr, 2001).

Seismology is a common geophysical discipline through which active volcanoes are monitored and studied, usually by examining processes associated with the stationary and/or transport effects of magma and gas that produce resonance and brittle earthquake sources, as their spatiotemporal migration and focal mechanisms and can provide insight to volcanic structure. A large variety of seismic signals are typically recorded in volcanic environments in response to source mechanisms and are classified by their waveform and spectral characteristics (e.g., Chouet, 2003; Kawakatsu and Yamamoto, 2015; Nakano and Kumagai, 2005). Volcano-tectonic (VT) signals, the features of which resemble those of tectonic earthquake waveforms, such as clear, high-frequency P and S onsets, are interpreted to be related to brittle failures, possibly as a consequence of magma migration and stress perturbations (Wassermann 2012). In contrast, long-period (LP) seismic signals, which are typically observed at volcanoes, are characterized by emergent onsets, the lack of a clear S phase, a narrow band or monochromatic radiation, and a predominantly low-frequency content of 0.2-10 Hz; LP signals have often been directly associated with shallow processes affecting volcanic plumbing systems (Del Pezzo et al., 2013). The production of these LP signals has been explained in two main ways: (1) LPs have been linked to resonance phenomena in response to gas and magma migration and pressure transients within low-viscosity fluid-gas mixtures, the sources of which have been successfully modeled by the resonance of fluid-filled fracture systems, cracks and conduits (Chouet, 1986, 1988; Neuberg et al., 2006); (2) LPs have also been explained as signals produced by slow-rupture failure in unconsolidated volcanic materials, resulting from the deformation of the shallow part of a volcanic edifice, thereby defining this source as a dry mechanism (Bean et al., 2014). In addition to VT and LP signals, a broader variety of seismic signals in volcanic environments have been proposed, including very-long-period (VLP), volcanic tremor (TR), hybrid (HB) and explosion (EX) signals (Wassermann, 2012). Nevertheless, the locations of VTs and LPs have been used to infer the geometries of plumbing systems. For instance, the lateral propagation of a ring dike beneath Mammoth Mountain, USA, was depicted by the clockwise migration of a VT swarm over a period spanning less than 1 year. In addition, deeper events clearly imaged along a near-vertical plane were interpreted as an intruding dike (Prejean et al., 2003). Similarly, the locations of LP and tremor sources enabled the geometry of the shallow conduit that fed the eruption episodes at Mt. Etna in September and November 2007 to be constrained (Patanè et al., 2008); furthermore, the locations of sustained LP signals associated with hydrothermal activity were employed to define the extent of the source, which was verified with a resonance model consisting of a crack filled with a water-gas fluid in Campi Flegrei, Italy (Cusano et al., 2008).

Very active volcanoes located near to populated areas usually own permanent seismic network to monitor and record data in real time, thereby allowing the risk of volcanic eruption to be studied and assessed continuously. One of the most active volcanoes in the Andean central volcanic zone is Lascar (Fig. 3.1). This volcano (5592 m; 23°22′ S, 67°44′ W) is located at

the southwestern part of the Altiplano-Puna Volcanic Complex (APVC; 21° to 24° S) which is characterized by a volcanism mainly andesitic laying on a 80 km thick crust (Kay and Coira, 2009). The formation of the APVC is associated with uplift produced by shortening of the crust due to plate convergence, a limited rate of magmatism due to shallow subduction processes, and an extensive and Tertiary ignimbrite responsible for producing the silicic volcanism in the region (de Silva, 1989). Lascar is an andesitic volcano composed of two partially overlapping stratocones with five nested craters aligned in an ENE–WSW trend; three craters are located on the eastern stratocone, and two are located on the western stratocone. The westernmost crater, which is usually characterized by permanent degassing from a fumarole field associated with a magmatic-hydrothermal system (Tassi et al., 2009), located on the eastern edifice is the only currently active crater (Matthews et al., 1997). The magma chamber has been hypothesized to be as deep as 10 km to 17 km beneath the volcano (González et al., 2015).

The historic record of activity contains two major eruptions that occurred in 1933 and 1993 (Global Volcanism Program, 2013). The 1993 eruption with a Volcanic Explosivity Index (VEI) of 4 seemingly changed the geometry of both the active crater and the subvolcanic plumbing system (Matthews et al., 1997) and modified the normal volcano activity, as was discerned from the corresponding variation in infrared radiance (Wooster, 2001). More than 10 eruptions have occurred in the 25 years since 1993, including the two more recent events in April 2013 (VEI 1) and October 2015 (VEI 2) (Global Volcanism Program, 2013). These two most recent eruptions were relatively short with a duration of approximately 1 hour; their eruptive style was characterized by postincandescence and single explosive eruptions with a gas plume varying from white to gray with ash emissions that rose 320 m and 2500 m for the 2013 and 2015 events, respectively, as reported by Observatorio Volcanologico de los Andes del Sur (OVDAS, 2013, 2015). Both eruptions were effectively monitored by a permanent multiparametric monitoring network operational since the end of 2010 consisting of seismic stations, time-lapse cameras, differential optical absorption spectroscopy (DOAS) gas sampling instrument, weather stations, and temperature and multigas sensors.

Recent research on Lascar has incorporated a wide range of observations. The search for a shallow magma plumbing system motivated various satellite interferometric synthetic aperture radar (InSAR) studies (Pritchard and Simons, 2002; Pavez et al., 2006), but interferometry was unable to reveal significant deformation associated with common phreatic eruptions. Local deformation was associated with the postdepositional contraction of material on the slopes (InSAR and GPR data; Whelley et al., 2012) and inside the craters (very high resolution (VHR) panchromatic and SAR data; Richter et al., 2018). In addition, numerous works have investigated the mechanism of crater formation. The development and continuous deepening of the Lascar craters is commonly explained by degassing within a shallow conduit system (Matthews et al., 1997) rather than by processes related to eruption. Active degassing from inside the craters, which has also been identified by remote sensing techniques (Bredemeyer et al., 2018), signifies the significant influence of a hydrothermal system, as is reflected by the ascension of deep fluids (Tassi et al., 2009). This can be attributed to the movement of fluid from a magma chamber at depths of 10 km to 17 km as was realized by spectral radiance sensing that produced thermal variations during the observed period of 2000-2004 (González et al., 2015). At present, degassing and changes in the crater morphology continue to be observed; for example, terrestrial laser scanning exposed fresh structures (de Zeeuw-van Dalfsen et al., 2017) displaying gradients in high-resolution surface deformation maps (Richter et al., 2018). These high-resolution data suggest that the deformation of the eastern craters is related to gravitational slumping, cooling, and the compaction of eruption products; however, these data do not provide evidence for deformation associated with a deeper plumbing system, magma pathway or magma chamber.

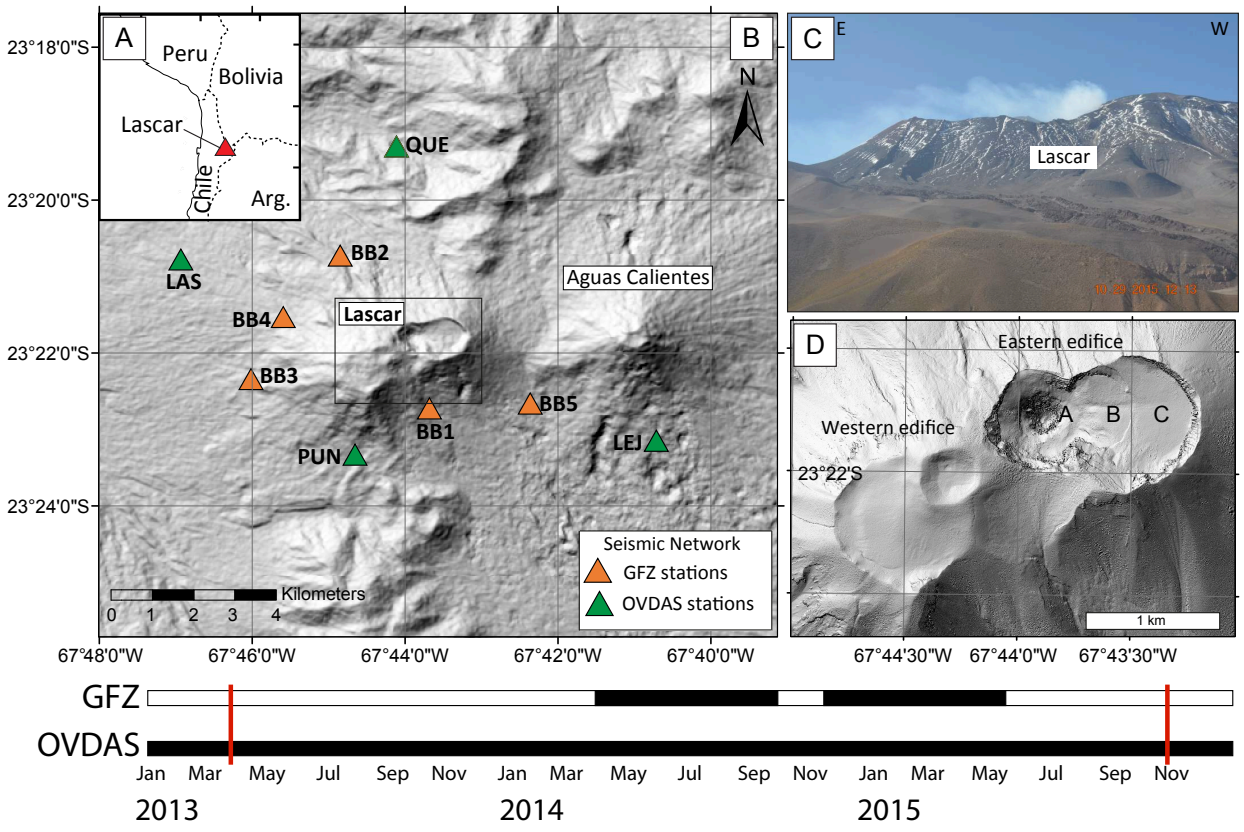

Figure 3.1: A) Location of the study area. B) Map of the area and seismic network deployed for monitoring Lascar volcano. C) View of the northern flank of the active eastern edifice. D) Amplified map of the inactive craters belonging to the western edifice and the eastern edifice with the nested active craters. The timelines show the operational durations of the OVDAS and GFZ seismic networks during the period covered by this study, during which Lascar produced two eruptions in 2013 and 2015 (red lines).

Some information is available about the deeper structure of Lascar. A seismological investigation identified long-term stationary harmonic tremors one year after the 1993 eruption, but these signals were thought to be associated with fumarole degassing (Asch et al., 1996). Closer analysis of the source of this tremor indicated that it could be related to water and/or gas migration in a shallow hydrothermal system, possibly at a depth of 2 km to 3 km (Hellweg, 2000). Additionally, a magnetotelluric study (Díaz et al., 2012) imaged a high-conductivity volume at only ~1 km beneath the summit, suggesting the presence of a shallow hydrothermal system; Díaz et al. (2012) further identified an anomaly at a depth of 6 km, which could be associated with a magma storage zone. Seismic wave interferometry allowed some scholars to speculate on the seismic velocity variations associated with inflation/deflation processes in a magmatic or hydrothermal reservoir during the period of unrest preceding the 2013 eruption (González et al., 2016). This velocity variation also coincided with an increase in the number of LPs, an intensification of fumarole degassing, and the phenomenon of crater incandescence. Similar changes were observed in the more recent 2015 episode of unrest, culminating in a short volcanic explosion on 30 October 2015 (Global Volcanism Program, 2016).

Here, we provide a comprehensive analysis of the data acquired by broadband seismic stations from both a permanent network and a temporary network (Fig. 3.1B) and focus on the locations of LPs and VTs, which represent the vast majority of signals recorded at Lascar during the 2013-2015 inter-eruptive phase. We take advantage of a dense seismological network and combine

signal classification with source location and source characterization to analyze the various types of events, thereby allowing us to characterize the plumbing system beneath Lascar volcano and infer further constraints on possible fluid and magma ascent paths. Moreover, to account for the weak signal amplitudes, emergent signal onsets and poor signal-to-noise ratios of the LP sources, we compare different techniques that are commonly used for challenging event location tasks considering patterns of the signal amplitude, polarization, coherency and correlation. Finally, a joint seismological analysis is performed to propose a plausible model for the internal structure of Lascar.

3.2 Methods

We investigate data acquired by both permanent and temporary networks. The permanent seismic network was installed in December 2012 by OVDAS and consist of 5 broadband stations (LAS, QUE, LEJ, PUN, and TAL) with a sampling rate of 100 Hz buried at a maximum height of 1 m above the bedrock. The temporal network operated from April 2014 to May 2015 with 5 additional broadband stations (BB1, BB2, BB3, BB4, and BB5) at a 100 Hz sampling rate (Fig. 3.1). All seismometers were buried ~1 m deep, thermally isolated and powered by battery/solar panels. The data were investigated using the standard classification (see section 3.2.1), and the location of LPs were evaluated using four different methods as described below. The full waveform data of the temporal network can be openly accessed through the GEOFON Data Centre (1993) data archive (https://geofon.gfz-potsdam.de/).

3.2.1 Signal characterization

Seismic data from the permanently operating OVDAS network are routinely scanned to detect and classify local seismic signals at Lascar, and event detection is performed in real time through visual inspection and classification. Event classification is based on the spectral content, harmonic signature and duration of the waveforms (Latter, 1981; Lahr et al., 1994; Chouet, 1996; Chouet and Matoza, 2013); as a result, the seismic activity at Lascar can be classified into volcanic-tectonic (VT), long-period (LP), very long-period (VLP), volcanic tremor (TR), hybrid (HB) or explosion (EX) signals.

The OVDAS seismic catalog contains 2893 events in the time period from January 1, 2013, to December 25, 2015, covering the whole inter-eruption phase from April 2013 to October 2015. From this catalog, we considered two types of events, VT and LP events, which are the most abundant and cover more than 85 % of the original catalog (approximately 2000 LPs and 350 VTs). The remaining 15 % of the catalog corresponds to the other signals listed above (HB, EX, and TR signals). LP and VT signals recorded at Lascar (see examples in Fig. 3.2A, B) present typical spectral contents and P phase properties similar to those observed at other volcanoes (e.g., Chouet, 1996). The LP spectra (Fig. 3.2A) are restricted to the frequency band between 0.2 and 10 Hz, show an emergent phase onset and lack clear P and S phases (McNutt, 2005). On the other hand, the VT spectral content mostly exceeds 5 Hz and presents impulsive P and S phases (Fig. 3.2B).

The following methods concentrate principally on further analyzing the identified LP events and their association with VT activity. The LP waveforms were visualized, and their first onsets were picked. While this picking procedure is not very accurate, given the emergent onset of LP signals, this approach is useful for automatically selecting time windows for the LP signals, which are used hereafter to perform signal polarization and cross-correlation analysis.

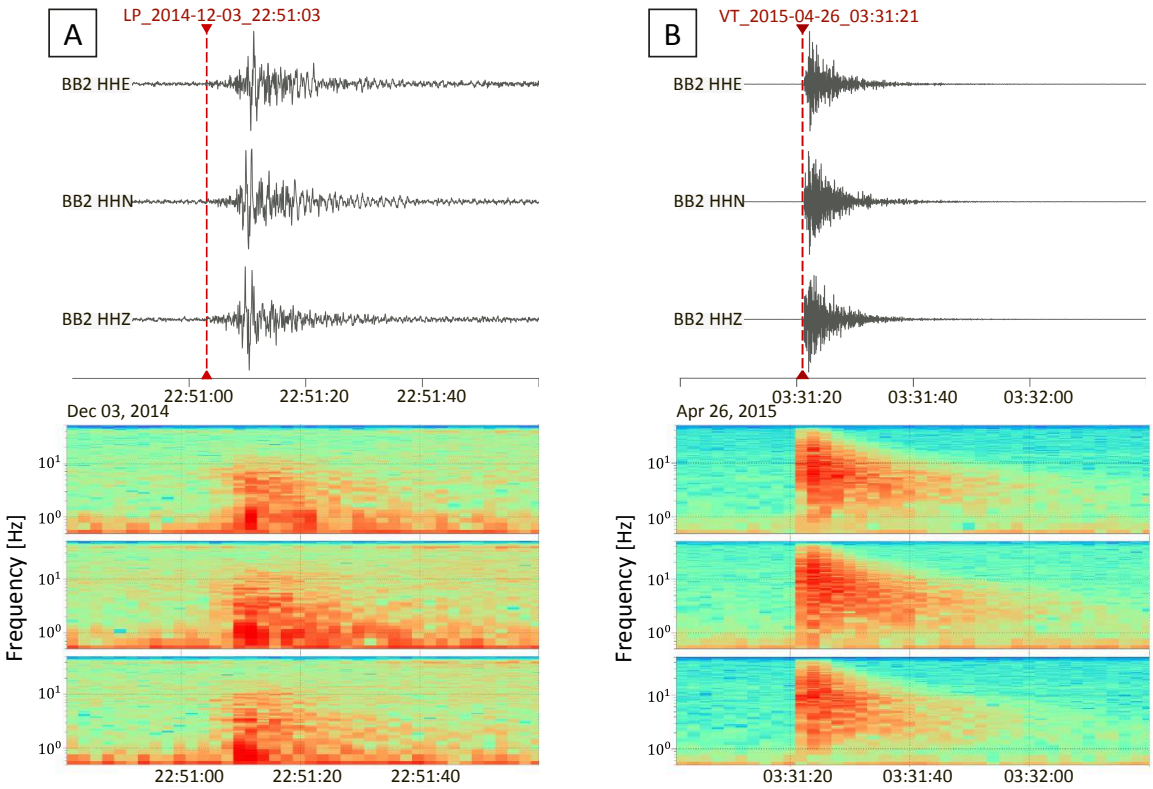

Figure 3.2: Seismic signals recorded at Lascar (top) and spectrograms (bottom). A) Characteristic LP waveforms with frequencies in the band below 10 Hz. B) Characteristic VT event with frequencies reaching 40 Hz.

3.2.2 LP waveform similarity

We evaluate the similarity among the LP waveforms to search for different clusters and to assess their spatial and temporal variations. The concept of waveform similarity based on the cross-correlation of signals at one or multiple stations is an accepted method in volcanic environments for the automated classification and identification of seismic signals and for the amplitude estimation and recurrence analysis of different families of signals, specifically LP signals (e.g., Lokmer et al., 2008; Cannata et al., 2009; Cauchie et al., 2015). The results are described by the waveform correlation, where a high waveform correlation is indicative of a similar location and radiation pattern for two seismic events.

Cluster analysis was applied to characterize the LP waveforms belonging to the long-lasting increase phase (LP II, see Fig. 3.4). We aim to infer the time dependence of the most plausible LP sources at Lascar that can confer information about any precursory signal associated with the 2015 eruption. This requirement is fulfilled only by the OVDAS network, which was tested for the most stable time stations (LAS, QUE and PUN). The test was applied by subtracting the full signal contained in a 12 s window in which onset is defined 2 s earlier from the event time defined in the OVDAS seismic catalog. Therefore, whenever the waveform is not fully contained in the data or suffers from data gaps, it is not considered for further analysis. We tested the signals by applying different filters between 0.75 Hz and 2.0 Hz and collected the waveforms in a folder for subsequent correlation. We iterated this procedure for the different spatial recording components of each station and computed the correlation matrix based on the waveform similarity cross-correlation value. Then, the correlation matrix, which hosts values in the range of [-1,1] for each event pair (ranging from -1 for anticorrelation to 1 for correlation, with 0 denoting no correlation), is transformed into a metric matrix by assigning a distance value of 0 to correlated waveforms and a value of 1 to uncorrelated waveforms. This matrix is used by a density-based clustering algorithm (Cesca et al., 2014) to identify a number of LP

clusters showing similar waveforms with established parameters, thereby establishing clusters of at least 10 waveforms sharing a cross-correlation similarity value exceeding 0.75. Our aim in the application of this method is to search for the spatial component with the highest waveform similarity, independent of the number of resolved clusters. These similar waveforms are then used to interpret the seismic source and further investigate the temporal evolution of LP seismicity.

3.2.3 Seismic event location

The OVDAS catalog provides first rough VT hypocentral locations and no tentative LP locations. The VTs were located in real time by expert seismology analysts assuming two available velocity models. The model provided by Comte et al. (1994) was used for the period from January to December 2013; later, this model was updated with a new study provided by Dorbath et al. (2008) for the remaining period (January 2014 to December 2015). To unify the locations of VTs and LPs under one velocity model, we used a homogenous model assuming a v_p/v_s ratio of 1.73 with $v_p = 4.39\,\mathrm{km/s}$ and $v_s = 2.40\,\mathrm{km/s}$ (Bohm et al., 2002) for the first 5 km, which comprises the zone of interest in this study.

The VT relocation was performed for events that contained 5 phases and were recorded by at least 4 stations. P and S onsets were picked on raw data, and the hypocentral parameters were computed using Hypo71 (Lee and Lahr, 1972). However, because the location of LPs is not trivial, we compare different approaches to locate these characteristic volcanic signals, as detailed below.

The characteristics of LP signals pose a challenge to the identification and accurate picking of first P-wave onsets as well as the recognition of S phases. The major practical consequence is that LPs cannot be located conventionally, and their hypocentral locations often suffer from large uncertainties (Lahr et al., 1994; Chouet, 2003). A number of innovative methods have been proposed to locate LP sources based on the analysis of the waveform amplitude (Battaglia et al., 2003) and polarization (e.g., Cesca et al., 2008). Following these methods, we propose and test two new approaches in this study. The first technique is based on the coherent detection of anomalous amplitude and polarization attributes at multiple stations: this approach has been applied to a range of seismic signals (e.g., Grigoli et al., 2013, 2014), but it has never been applied to LPs heretofore. The second new approach relies on the cross-correlation of similar waveforms recorded at different stations and is tested with LPs for the first time in this study. The time period and hence the number of LPs chosen for the application of these methods were determined according to the availability of good-quality signals according the requirements of each method. The results and performance of these four methods are presented below.

3.2.3.1 Amplitude-based location of LPs

Source location methods based on the decay of seismic amplitudes with increasing distance to the source due to geometrical spreading and attenuation under the assumption of isotropic radiation patterns (Battaglia and Aki, 2003; Battaglia et al., 2003) have been widely used to locate LP, VLP, explosion and volcanic tremor (Di Grazia et al., 2006; Kumagai et al., 2011; Taisne et al., 2011; Morioka et al., 2017). These methods are based on the simple observation that seismic amplitudes (using peak, median or mean absolute amplitudes) often exhibit a smooth spatial pattern after correcting for local amplification factors, which can be readily explained by the theoretical decay of surface or body wave amplitudes in a homogeneous medium; an inversion method can then be established to derive the location that best reproduces the observed peak amplitude pattern (Battaglia and Aki, 2003).

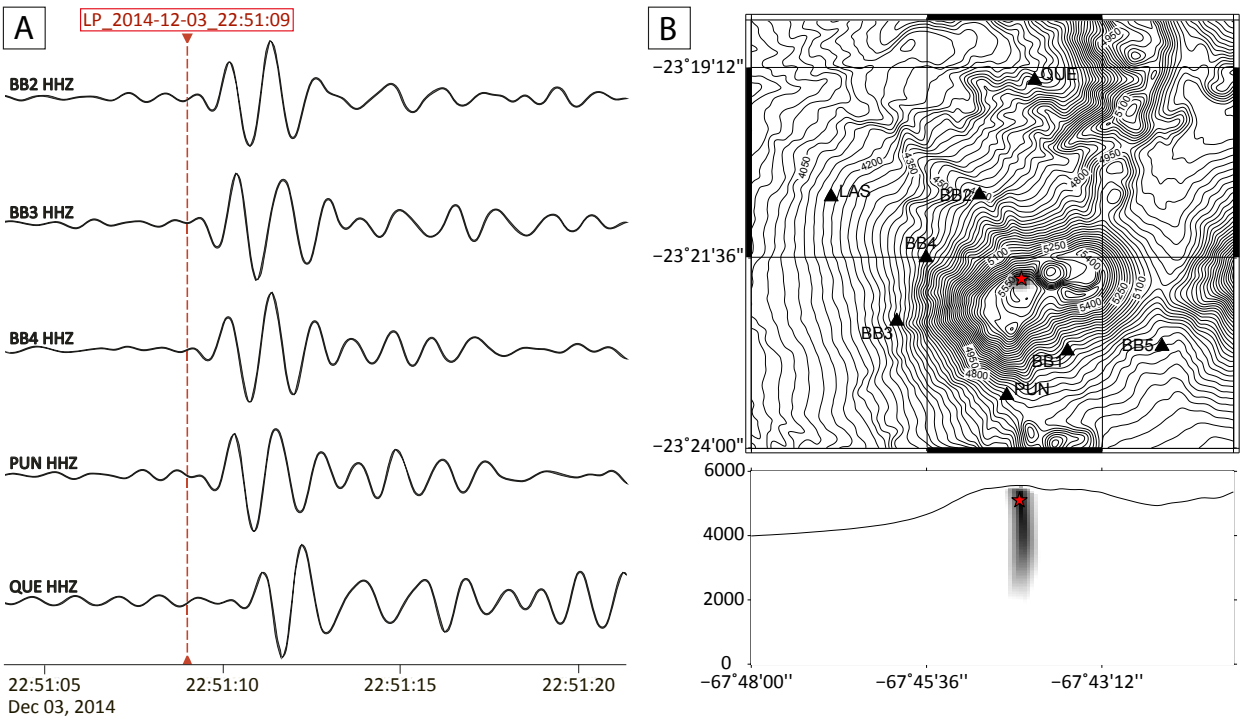

Figure 3.3: A) Vertical component of one characteristic LP event after applying a passband filter at band frequencies of 0.1–1 Hz, revealing a high waveform similarity among different stations. This feature is implemented using cross-correlation to derive the interstation differential arrival time. The event onset waveform, including the day and time are indicated in red. Interstation cross-correlation is performed on a 10 s long time window (filtered vertical component) starting at the picked onset. B) Map and profile views of the synthetic test showing the uncertainties of the cross-correlation method. The red star indicates the location obtained using our velocity model (see section 3.2.3) and the grayscale its corresponding temporal residual depict a high accuracy of the epicentral location and a high uncertainty in the hypocentral constraint.

We located the 196 most energetic LPs recorded by at least 5 stations between September 2014 and October 2015 based on the peak-to-peak amplitudes after applying a bandpass filter in the range of 1–10 Hz. As the location computed through this method uses the spatial distribution of seismic amplitudes, any amplification due to site effect must be removed. Thus, we estimated the site effect represented as the coda amplification factor to correct the seismic amplitudes, as proposed by Battaglia and Aki (2003). To this aim, we assume that the subsurface beneath the volcano is composed of several elastic layers locally characterized by different geometries and attenuation factors, which may locally affect waveform amplitudes and could affect the locations of LPs. To quantify the energy dissipation due to both intrinsic and scattering attenuation, we calculate the quality factor Q^{-1} (Equation 3.1) and minimize the location errors when compared with the theoretical amplitudes calculated for each station as a function of the station-hypocenter distance by iterating over values of the hypocenter. After the application of the coda amplitude regression, we chose 25 regional events with a satisfactory correlation coefficient ($R \geq 0.7$) that were registered by stations BB2, BB3, BB4, BB5, QUE and LAS, all of which are located more than 100 km from the volcano, and calculated the relative site amplification factors, using station BB2 (Fig. 3.1B) as a reference, which shows good-quality data.

$$Q = 2\pi \frac{E}{\delta E} \tag{3.1}$$

3.2.3.2 Polarization-based location of LPs

While LP signals are emergent and first onsets cannot be easily identified, an increase in the signal amplitude is observed at most stations located on the volcano flanks, and this characteristic can be used to assess the polarization of the signal. Many authors have used the linear polarization of particle motions, even in the absence of an accurate velocity model, to locate the sources of seismic signals (including LP and VLP signals) at volcanoes (Del Pezzo et al., 1992; Neuberg et al., 1994; Neuberg and Luckett, 1996; Battaglia et al., 2003; Marchetti and Ripepe, 2005; Saccorotti et al., 2007; Cesca et al., 2008). The general approach is simple: either the 3 components of the seismogram or the two horizontal components only are considered to reconstruct the ground motion vector or its horizontal projection. LP signals often show rectilinear particle motion observed either for the whole signal or for the first part of the signal alone, and this particle motion is assumed to correspond to a P-wave signal. At Lascar, the LP signals at some stations (e.g., BB3, BB4) show a linearly polarized signal for 1-2 s, although this polarization is lost in the later part of the signal, possibly due to the interaction between the seismic radiation and the volcanic topography. Assuming that the first part of the polarized signal corresponds to a P phase, which particle motion should point in the direction of the seismic source, the derived particle motion vector can be back-traced along its travel path, providing a range of potential locations. Performing this analysis for multiple seismic stations allows the hypocentral location (or the epicentral location if the analysis is performed on the horizontal components only) to be mapped: the source location can be found by minimizing the sum of the residuals among the observed and predicted polarization orientations. However, inverting the 3-component ground motion vectors at a volcano requires surface corrections accounting for topography to be applied (Neuberg and Pointer, 2000).

While the method described in section 3.2.3.1 considers the datasets recorded by both networks (OVDAS and GFZ), here, we consider only a selection of 138 LPs recorded by the GFZ temporal network during the period from December 2014 to May 2015 (see Fig. 3.1). We assess the polarization of the signals for these events both for the horizontal components and for the 3-component recordings. We first use the 2-component approach to discuss the epicentral locations of the LPs, and then extend the analysis to all 3-component to further constrain their hypocentral depths. The processing is performed as follows. Particle motions are computed using 3 s long time windows starting 1 s before the first visible amplitude increment after manual picking that corresponds to the first part of the detected LP signal. The seismic signals are then filtered, applying a 4th order Butterworth filter between 0.05 and 1.50 Hz. The polarization analysis is implemented on the 3-component signal in the ObsPy library (Beyreuther et al., 2010) based on the work of Jurkevics (1988). In our implementation, we adopt the definition of rectilinearity given by Montalbetti and Kanasewich (1970) by first considering the two horizontal components to derive the backazimuth and then considering the radial and vertical components to derive the incidence angle. We consider only the signals whose rectilinearity coefficient is larger than 10. In such cases, the backazimuth and incidence angle are inferred, and the deformation vector is used to infer the potential range of locations.

3.2.3.3 Coherency-based location of LPs

Recent automated migration-based location techniques have been developed to detect coherent seismic signals at multiple seismic stations from continuous recordings (see for a review Cesca and Grigoli, 2015). Whereas these techniques are applied mostly to microseismic and regional seismicity datasets (e.g., Kao and Shan, 2004, 2007; Gharti et al., 2010; Grigoli et al., 2013, 2014; Zeng et al., 2014), they may be suited for volcano seismology applications, particularly for locating LP events, given that they do not require any manual phase picking. One category of these coherency-based location algorithms is based on the concepts of the delay and sum

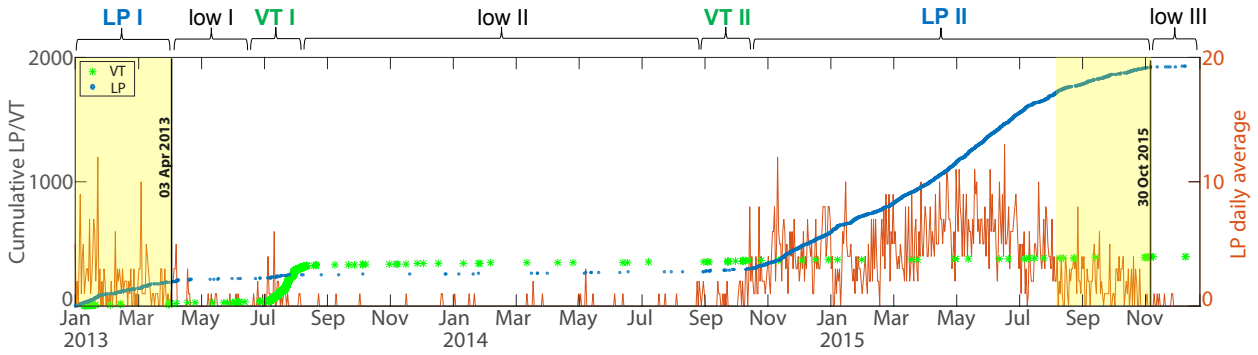

Figure 3.4: Temporal evolution of LP (blue dots) and VT (green stars) events recorded in the period covered by this study. The daily average of LP events (shown in orange) reveals 10 months of an unusually high average preceding the 2015 eruption (LP II) associated with an increasing period of LP activity. The subsequent phase shows a decrease in the rate of LP events starting 2 months before the eruption; this pattern is also observed for the 2013 eruption (LP I), where the activity declines rapidly after the event. Similar patterns in the decreasing LP activity period preceding the 2013 and 2015 eruptions are shaded in yellow.

of characteristic functions, which are positive time series derived from the observed waveforms depicting increments in amplitude, spectral or polarization attributes. The source location is performed using a coherence function, which is obtained by stacking the absolute amplitudes of characteristic functions recorded at different stations according to theoretical travel times over a 4D spatiotemporal grid and then scanning a potential seismogenic volume for different origin times.

In this work, we sample the potential seismogenic volume extending spatially over dimensions of 15.3 km (east) x 10.8 km (north) x 10.0 km (depth) around Lascar volcano containing 2,212,001 grid points. The spatial sampling ranges between 85 m and 100 m depending on the axes. The volume extends from 6.0 km above sea level (a.s.l.) to 4.0 km below sea level. We use raw velocity traces sampled at 100 Hz. We applied this method to 256 LP events recorded between September 2014 and April 2015; beyond this period, the network was operated discontinuously and no longer fulfilled the conditions for operating stations. For the application of this method we adopted the two characteristic functions proposed by Grigoli et al. (2014): first onsets (i.e., P phases) are detected through the short-term-average/long-term-average (STA/LTA, with a short time window of 0.25 s and a long-time window of 0.75 s) of the vertical energy characteristic function, sensitive to the P-phase amplitude increase on the vertical component; furthermore, we aim to detect S phases through the STA/LTA (with the same parametrization) of a second characteristic function, which is sensitive to the S-wave polarization, based on the principal component analysis technique. Theoretical travel times are computed for P and S waves, assuming the homogeneous velocity model described in section 3.2.3 (called M1) and for a second model denoted M2 (v_p = 5.51 km/s, v_s = 3.19 km/s), in which the standard v_p/v_s ratio is also 1.73 (Bohm et al., 2002). This approach circumvents the challenging identification of P and S phases of LPs, by relying instead on the detection of anomalous amplitude and polarization patterns at multiple stations.

3.2.3.4 Cross-correlation-based location of LPs

The cross-correlations of filtered waveforms recorded at the same stations for different events can be used to resolve the relative locations of seismic sources producing similar waveforms at each station. The development and application of double-difference techniques (Waldhauser and Ellsworth, 2000; Waldhauser, 2001) based on the cross-correlation approach has produced substantial advances in improving earthquake locations by suppressing most location uncertainties due to unknown velocity structures without the use of station corrections (Schaff and

Waldhauser, 2005). The cross-correlation technique has been applied to a variety of seismological observations to derive relative hypocentral locations, including seismic signals at volcanoes (Matoza et al., 2013) and specifically LP events (Matoza et al., 2014). In the original approach by Matoza et al. (2013), cross-correlation was performed among the S phases of event pairs to infer the differential S time to locate different seismic signals at volcanoes.

In this work, we use cross-correlation in a different way. Instead of correlating pairs of events at a common station to infer their relative locations, we correlate the waveforms recorded at different stations for the same event to infer the travel time differences and, based upon those differences, the absolute event locations. This approach is possible here only because the observed vertical components of LP signals appear highly similar at most stations deployed on the flanks of the volcanic edifice (Fig. 3.3). The high waveform similarity on the vertical components has further implications in terms of the source radiation pattern, which will be discussed later. Under this condition, we can compute differential P arrival times at each station pair for each considered LPs and constrain the absolute source location with the differential travel time and location of each station. For this analysis, we considered raw velocity waveforms for the vertical components filtered using a 4-pole Butterworth bandpass filter in the frequency band of 0.1–1 Hz and considering a window length of 10 s starting before the first amplitude peak increase for a 1D velocity model. We next performed a grid search for any potential location using the same grid as that used in the coherence-based location approach while assuming a range of homogeneous P-wave velocities between 2.5 and 4.5 km/s and minimizing the differences among the estimated and theoretical differential P arrival times. Out of all the detected LPs, we considered only those with sufficiently high cross-correlations (above 0.8) estimated for at least 8 station pairs, thereby reducing the data set to 83 LPs in the time span from December 2014 to May 2015, which constitutes the period with continuous data recording and the highest network density (see Fig. 3.1). We performed a synthetic test to assess the spatial resolution of this location approach: we assumed a shallow LP source beneath the crater region and computed differential arrival times at the used station pairs while assuming a velocity model with a P-wave velocity of 4 km/s. Then, we applied our location approach, estimated the theoretical differential times (instead of deriving them through waveform cross-correlation) and mapped the spatial distribution of residuals (shown in grayscale in Fig. 3.3B). Our results indicate a good epicentral resolution but a relatively low depth resolution. We also executed a second test by deriving the LP event locations using velocity models perturbed in the range between 2.5 and 4.5 km/s: the result was similar in the sense that we could correctly retrieve the epicentral location while assuming a perturbed velocity model, but shifts were introduced into the resulting depths. This is a novel method, and the results are comparable to other techniques.

3.3 Results

3.3.1 Temporal evolution of LPs and VTs

Based on the significant variations in the numbers of LPs and VTs throughout the entire period covered by this study, we subdivide their temporal evolution into 7 seismicity phases of activity at Lascar volcano (LP I, low I, VT I, low II, VT II, LP II, and low III). Fig. 3.4 graphically outlines these phases by means of the daily rates of LP events and the cumulative number of both LPs and VTs. The low, steady VT activity rate (less than 1 event/day) is obviously exceeded during two, short-duration bursts of activity. The first and largest burst occurred in June-July 2013 (phase VT I in Fig. 3.4, ~300 events), accompanied by a weak increase in LP activity. The second and weaker phase of VT activity struck in September-October 2014 (phase VT II, 9 events). Phase VT II was accompanied by crater incandescence and

effectively coincided with the subtle beginning of a sustained long-term anomaly of LP events; the remarkably long-term LP II anomaly began in September 2014 and lasted for approximately 14 months, culminating in the eruption on October 30, 2015. The LP seismicity rate appears to be strongly modulated in time: during the initial phase corresponding to VT II, LP activity was rather weak, but the activity slowly and steadily increased thereafter until reaching a peak of 13 events/day in May-June 2015 and then slowly decreased to less than 5 events/day while approaching the 2015 eruption. After this eruption, LP activity dropped substantially to the previous phase of quiescence (phase low III). Interestingly, similar decay in the anomaly of LP events is observed just before the 2013 eruption (phase LP I); unfortunately, the catalog is incomplete at preceding dates and therefore does not allow a full comparison of precursor LP activities prior to the 2013 and 2015 eruptions.

Sections 3.2.3.2 and 3.2.3.3 describe the results for the most interesting VT and LP phases, discussing waveform similarity (LP II) and hypocentral locations (VT I, VT II and LP II). The LP II phase is especially attractive due to the abundant number of events, recorded in a phase of densified seismic network (see Fig. 3.1) and in view of its role in the preparatory phase of the 2015 eruption.

3.3.2 LP waveform similarity

The iterative application of a cluster analysis, separately performed for all spatial components of stations QUE, LAS and PUN provides evidence for one single cluster of similar events. This is better resolved using seismic data of stations PUN and QUE, with the last one showing the most clear result and highest waveform similarity. This cluster remains undetectable using the data from station LAS, probably due to the lower signal-to-noise ratio at this site. The final clustering results concern only events recorded at more stations and are clustered on different components simultaneously. This reduces the starting dataset to 450 LP events and reduces the number of clustered events to 72. While losing many events, we can argue with relatively safety that these clustered events represent a similar process since a strict control has been implemented insomuch that these LPs have similar waveforms recorded at different stations and on different components. This high waveform similarity indicates a similar location and radiation pattern but also depends on the quality of the signal: we found that clustered events typically show larger amplitudes than unclustered events. This suggests that unclustered events may also be generated by a similar mechanism, but this mechanism is associated with weaker and noisier signals, and the noise affects the waveform similarity.

The results are illustrated in Fig. 3.5 for station QUE. Clustered LP waveforms with high similarity are shown individually according to their occurrence in time, and they are stacked as well; by stacking similar waveforms, we enhance the common LP signal against random noise and thus improve the signal-to-noise ratio. Stacked waveforms are characterized by clearly visible amplitude modulations (e.g., on the north component of station QUE), which could be controlled by the presence of different seismic phases, the interaction between the seismic radiation with the topography or other strong impedance contrasts, or by the complexity of the source time function. Depending on the waveform amplitudes and seismic noise contamination, the number of clustered signals changes from case to case.

We observe no temporal variation of the waveform similarity, which could suggest a spatiotemporal migration or a temporal change of the source mechanism. The individual plots of the waveforms support the occurrence of an LP event produced by the same source throughout the entire phase LP II (clustered events occur from September 2, 2014, to October 26, 2015). This discards the possibility of employing the temporal evolution of the source as an indicator for a preparatory eruption phase and instead alludes to the recurring occurrence of the same

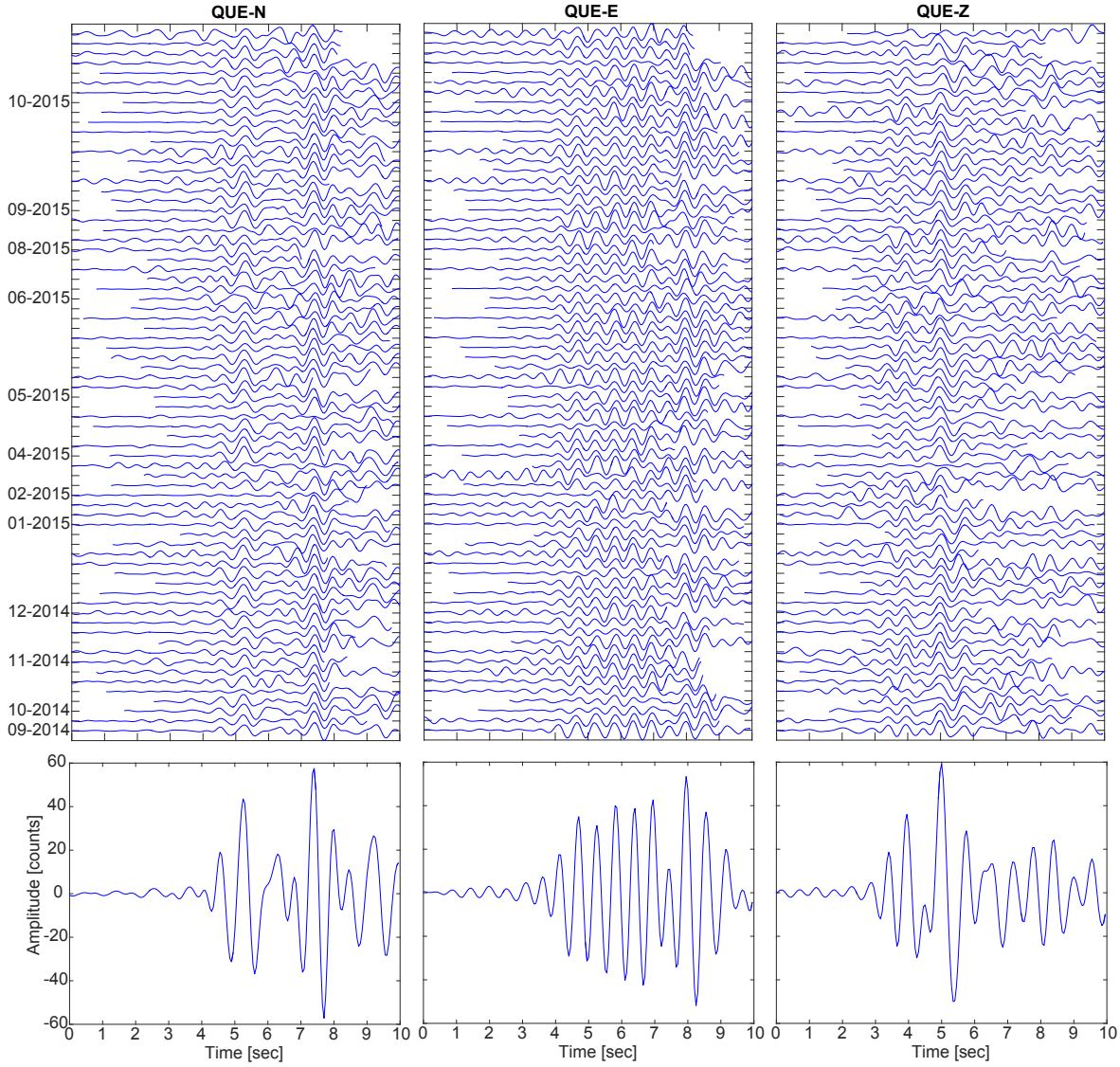

Figure 3.5: Similar LP waveforms on the north, east and vertical components recorded at station QUE. The waveforms correspond to 72 events derived from cluster analysis of the QUE-E component aligned upon cross-correlation, and the respective waveform stacks are shown in the bottom row for the three components. The occurrence dates are sorted on the vertical axis by month.

process with a similar source location and source mechanism that is responsible for the observed similar LP signals. This process is likely to be active over several months, although with a variable activity rate.

3.3.3 Seismic event locations

Fig. 3.6 shows the results obtained by applying the first three location methods described previously. From the amplitude based method (Fig. 3.6A), we observe the LP sources to be located within a compact and shallow cluster confined at depths from 2 km to 5 km below the summit, which has an altitude of 5592 m. However, the cluster location shows a significant offset of approximately 1 km to the northeast with respect to the summit of Lascar, where no surface expression of degassing or surface fracturing has been observed. It is worth noting that, due to the limited data availability and waveform quality, most events have been located using a station geometry with poor azimuthal coverage.

Upon applying the polarization-based method, only a limited number of stations show clear

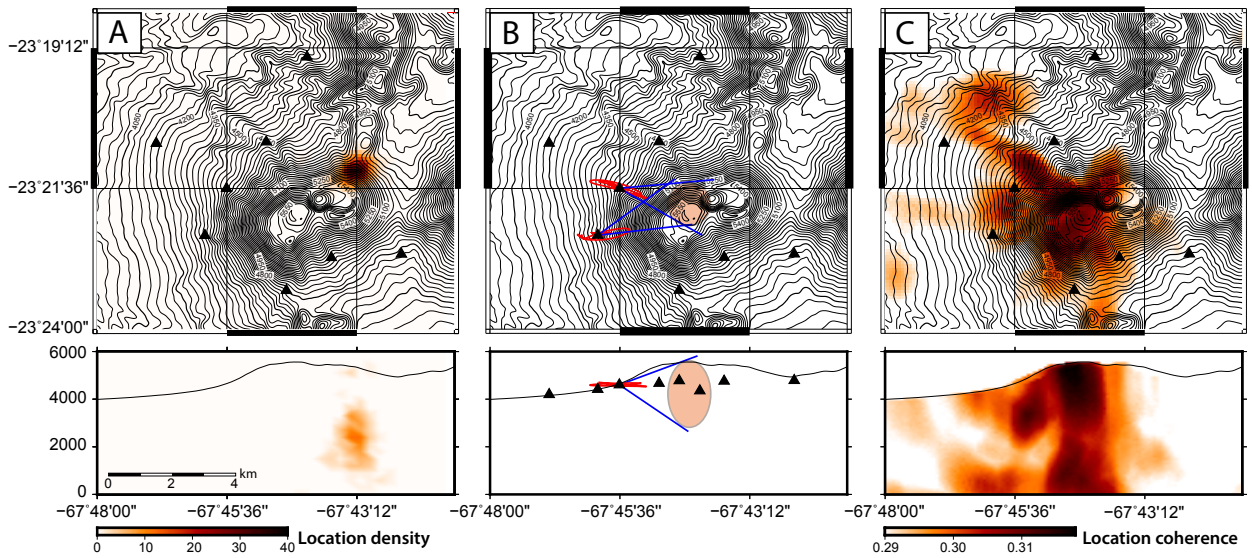

Figure 3.6: Location results using three different methods to compute the hypocentral locations of the LPs in map view (top) and E-W cross sections (bottom), where the black triangles denote broadband stations. A) Amplitude-based LP locations, where the color bar denotes the density of hypocentral locations. B) Polarization-based LP location based on the rectilinear polarization of particle motions at stations BB3 and BB4 (the particle motions are plotted in red for two LPs) pointing to a source region (light brown ellipse only for illustration) located NE of BB3 and ESE of BB4 (blue wedges). C) Coherence-based LP locations, where the color bar denotes the cumulative coherence of all studied LPs.

linear polarization; furthermore, the mentioned rectilinearity condition is rarely met at multiple stations simultaneously for the same event. In particular, stations located on the western flank of the edifice show higher signal polarization, while the polarization is lost to the north and south of the crater and at larger distances. According to abovementioned, the filtered LP signals often appear to be linearly polarized at station BB4 and, in some cases, at stations BB3 and BB2 (see examples in Fig. 3.6B). High signal polarization is rarely observed at other stations, possibly because of their larger epicentral distances and/or topographic effects. At station BB4, 75 computed backazimuths vary between 85° and 120°, while at station BB3, 14 backazimuths range between 48° and 94°. Station BB2 shows highly variable and incompatible particle motion directions and thus does not add a further constraint on the source location. These results are compatible with epicentral locations within an elongated EW-trending region just west of the crater rim in the vicinity of the summit or further eastward. Moreover, the incidence angles restrict the depth beneath the volcano dome in the range of altitudes between ~2.5 km and the summit. An interesting observation concerns the variability of polarization at different stations, which is sometimes higher at either BB4 or BB3 but rarely simultaneously. One possible explanation would be variability in the hypocentral location coincident with different wavefield interactions with the volcanic topography or other structural heterogeneities, thereby disrupting the observed polarization at one station or the other depending on the source location. An alternative explanation may concern the variability of the focal mechanisms and radiation pattern and thus a different geometry of the seismic sources with higher polarization of the P signal at different azimuths. In these conditions, rather than deriving absolute locations for single events, we could find only the approximate location of the LP seismogenic source under the assumption that these LP events are generated within a relatively confined volume.

The application of the coherence-based method provides a whole set of hypocentral locations. The locations were calculated using the general model M1 (see section 3.2.3) and a secondary model M2 (see section 3.2.3.3); M1 showed a better performance in general, providing higher coherence values for most events. Although these events are more scattered than the loca-

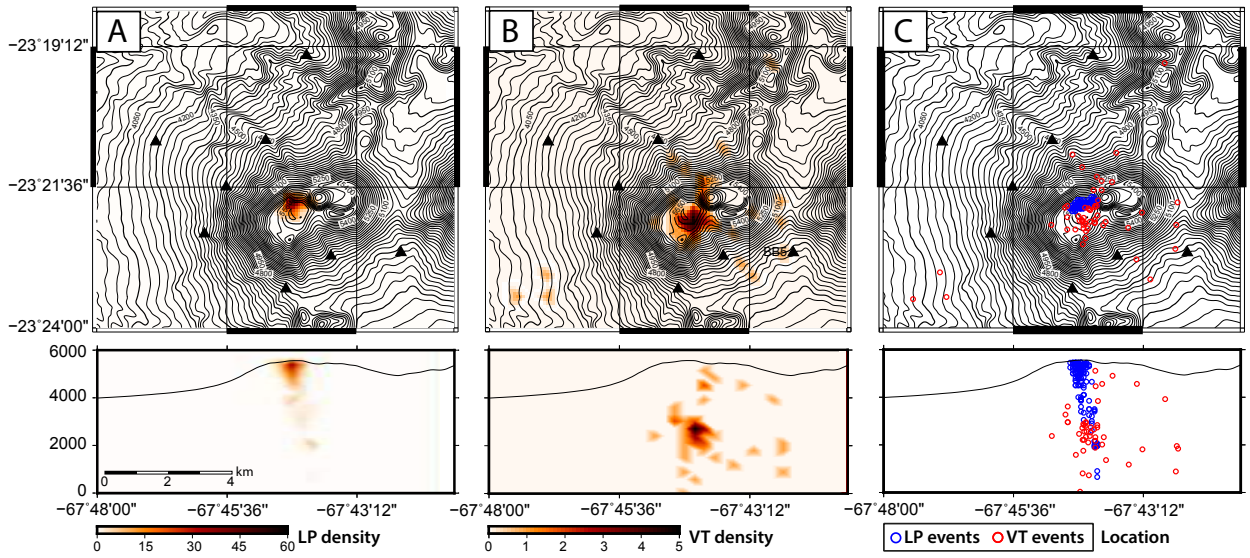

Figure 3.7: Cross-correlation-based LP locations and standard VT locations shown in map view (top) and E-W vertical cross sections (bottom). A) LP location density. B) VT location density. C) Hypocentral locations of LPs (blue) and VTs (red).

tions obtained from the amplitude-based method, we find that an important majority of the coherence-based locations reside within a small area of high coherency. As a result, stacking the coherence matrices for all processed events (following Cesca et al., 2016) reveals a region of high coherence at a very shallow depth extending from the summit down to ~3 km (Fig. 3.6C) exactly below the summit of Lascar volcano (~2.5 to 5.5 km a.s.l.), and these findings are in very good agreement with the independent results of the polarization-based location.

Finally, the cross-correlation method revealed the majority of locations for a velocity of 4.0 km/s, consistent with the velocity model proposed for the applications of this approach (v_p = 3.9 km/s, see section 3.2.3). Thus, we fixed this velocity model and repeated the inversion for the hypocentral location only. The resulting LP event locations are shown in Fig. 3.7 together with 52 relocated VTs that correspond to increased activity during phases VT I and VT II (see Fig. 3.4). The correlation-based LP locations are in general agreement with those relying on the polarization and coherence (Fig. 3.6B, C). However, they identify a much more compact cluster of locations with epicenters that are aligned along an ENE-WSW direction. In depth, the cluster extends from the western rim of the active crater (crater A in Fig. 3.1D) down to an altitude of at least 3.5 km along a narrow stripe, delineating a path along which fluid and gas ascend in the uppermost part of the plumbing system. Most locations, including all of those with lower residuals (below 0.1 s), are found in the shallowest 2 km.

The VT locations are more scattered than the LP locations; most of them occur in correspondence with the LP cluster but at larger depths (between ~0 km and ~3 km a.s.l.). The VT events have a maximum magnitude of 2.3, and the hypocentral errors in the horizontal (Erh) and vertical (Erz) components are smaller than 1.6 and 4.0 km, respectively, with root mean square (RMS) values below 0.6 s. Finally, from the entire image of LP and VT event locations, we can observe a transition phase from VT to LP sources, which would indicate that the uppermost region of brittle processes is found at an altitude of approximately 1.5–3 km and thus at least 3 km below the summit.

3.4 Discussion

This is the first detailed seismic study focused on Lascar volcano in many decades, and the results reveal the presence of approximately 2000 LP and 350 VT events. To confirm standard VT event location methods, we applied the LP event location methods presented in the literature and proposed a new strategy for obtaining reliable results in a difficult volcanic environment.

The results are in general agreement and suggest the presence of a shallow hydrothermal system with a deeper elongated arrangement that can be interpreted as a plumbing system, which would coincide with the findings of independent studies, as further discussed below. However, before debating the implications of the deeper structure under Lascar volcano, we discuss the performance of the LP location methods.

3.4.1 LP location methods

With this well-covered dataset, we were able to describe the inter-eruption phase of Lascar volcano, giving a complete analysis of the most typical seismic waveforms in terms of their source locations and mechanisms. For this purpose, we applied four different methods to locate the most abundant events (LP) recorded. Three of the applied location methods (i.e., the polarization-, coherence- and cross-correlation-based methods) agree on the stationary hypocentral locations of the LP events at shallow depths beneath the volcano summit (Fig. 3.6B, C and 3.7A). However, the hypocentral locations achieved using the (commonly used) amplitude-based method are slightly shifted laterally towards the northeastern flank of Lascar volcano (Fig. 3.6A). The hypocentral accuracy depends, among other factors, on the network geometry, velocity structure and quality of arrival time data. Hence, this lateral shift could result from the limited number of stations and poor azimuthal coverage: the two stations closest to the summit were not considered in this analysis due to the presence of a high seismic noise level (probably produced by the very strong winds in this region). This effect was already discussed elsewhere, for instance, at Etna volcano, where the exclusion of two stations near the summit resulted in the spreading of epicenters in comparison with the results based on the full network (Zobin, 2012). Additionally, using regional events rather than local events to estimate the amplitude corrections may bias the results of the amplitude-based location. However, we discard the effect of the velocity structure because the amplitude-based method does not require a velocity model or P phase picking. On the other hand, the coherence and polarization based methods defines a seismogenic region where it is relatively plausible to find LP sources (at shallow depth from the volcano summit down to ~3 km a.s.l.), but they do not provide precise locations. In contrast, the cross-correlation of waveforms recorded at different stations, provides more accurate and solid results, that match qualitatively the hypocentral region identified by the polarization and coherence-based methods. Thus, this method was successfully applied at Lascar despite the fact that this approach is rarely used at volcanoes and is possible only with a certain source mechanism geometry. The correlation-based method resulted in robust locations for the chosen velocity model with a high accuracy in the epicentral solution, while the depth resolution was less accurate (Fig. 3.3B). Remarkably, these results do not significantly change by perturbing P and S wave velocities, and provide similar LP locations for a range of tested velocity models. In this work, we suggest a comparative analysis of these different location methods as a robust approach to overcome the challenges associated with locating the hypocenters of LP events.

3.4.2 Precursory signals

This work highlighted an almost complete LP quiescence (Fig. 3.4) lasting about 16 months after the 2013 eruption (May 2013 to August 2014). This was followed by a subtle, but long-lasting increase in LP activity (September 2014 to July 2015) before the number of LPs gradually decreased again (August 2015 to October 2015). Another eruption occurred on October 30, 2015. After the eruption we observed again the start of a new LP quiescence period, with almost complete absence of LP activity. The 2015 LP decrease pattern preceding the most recent eruption was also observed before the 2013 eruption with a comparable occurrence rate of LPs while approaching the eruption time. The seismicity therefore indicates that the volcano was in an elevated stage of activity, but it did not display a sharp culmination of events shortly before erupting. This peculiar modulation appears as a preparatory phase of the system prior to an eruption as short-term swarms of precursory activity described, e.g., at Chichón volcano, Mexico; Mt. Pinatubo, Philippines; and Redoubt, Alaska (Chouet, 1996). Likewise, Mt. Etna volcano, in Italy has exhibited a similar LP rate pattern prior to the May 2008 lava fountain episode (an LP period decrease over two weeks, Bonaccorso et al., 2011) as well as prior to the November 2007 strombolian activity and subsequent lava fountain episodes (LP increase/decrease and variation of other signals over a period of two months, Patanè et al., 2008). The LP activity therein was explained as a result of the transport/discharge of gas-rich magma. The main differences between the LP modulations at Lascar and those at Mt. Etna concern the shorter duration of the latter (weeks at Etna versus months at Lascar) and their culmination into lava eruptions compared with the weak explosions accompanied by ash emissions at Lascar volcano.

Redoubt volcano has also shown similar LP precursors over both short (hours to days, Chouet et al., 1994) and long (months to years) time periods. For example, a 6-7 months LP anomaly preceded the March 23, 2009, Redoubt eruption. Then, two months before the eruption, the LP activity dwindled and began to display tremor-like activity. This process has been explained as a protracted period of slow magma ascent, followed by a rapid increasing pressure over a short period (Roman and Gardine, 2013). However, we do not observe exactly the same evolution at Lascar (i.e., the change from LP to tremor-like activity); in the last few months, the LP activity at Lascar decreased. Possibly at Lascar, the rising fluids experienced the following scenarios: (i) they were blocked by a closed fluid path, possibly associated with crater subsidence (González et al., 2015; Richter et al., 2018); (ii) ascending fluids propagated into a very weak material (although we would expect tremor-like signal in this case); or (iii) the ascending fluids and/or magma stalled. In the third case, an important question must be raised: why did the eruption occur? It is possible that such an eruption occurred not to further increase the pressure from below but rather as the result of an external trigger, such as rainfall leading water-magma interaction. The details of this eruption must be elaborated in future works, offering the chance to establish patterns in volcano monitoring data and assess the volcanic hazard over both short and long time scales.

3.4.3 Implications of the similarity among seismic waveforms

While we could not perform an accurate investigation of the source mechanism in this work, the observation of similar vertical component waveforms at different azimuths suggests a radially symmetric radiation pattern comparable to the oscillation of, e.g., a vertical conduit, a spherical volume or a horizontal crack. Given the spatial distribution of the hypocenters along a sub-vertical path, the hypothesis of the oscillation of a vertical conduit appears to be the most plausible. The relatively compact region of shallow LPs depicted by their hypocentral locations, the high waveform similarity and the lack of their spatiotemporal migration throughout the

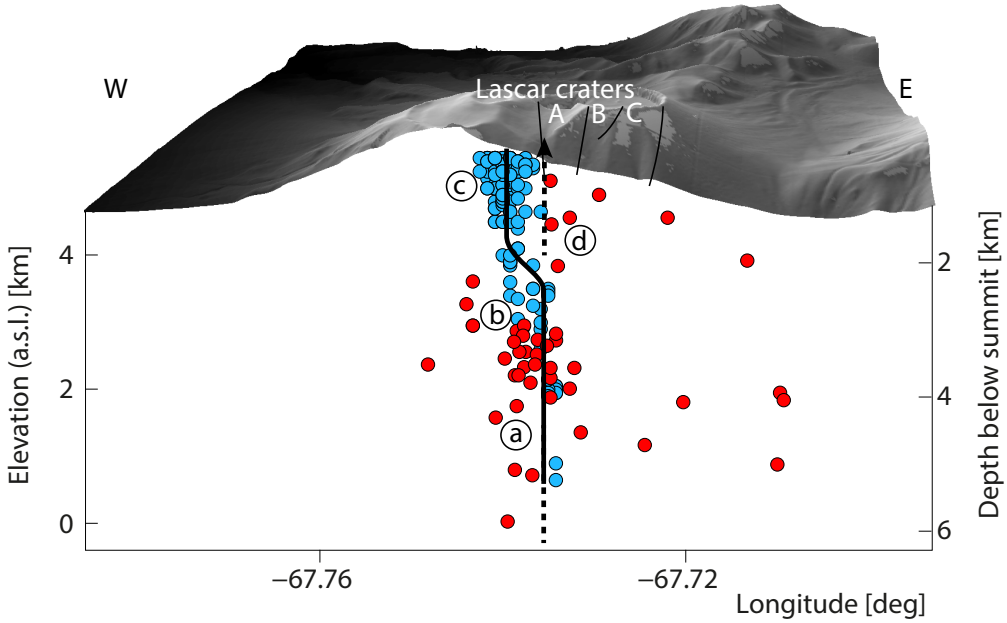

Figure 3.8: Schematic representation of the Lascar topographic profile and path geometry imaged by the LP (blue dots) and VT (red dots) hypocenters. The black thick line represents the three main zones recognized from the hypocentral distribution: (a) sub-vertical deep conduit and VT cluster beneath zone (b), (b) bending zone where the LP trend changes; and (c) shallow LP cluster. The dashed arrow (d) represents the expected path towards the active crater A. Black solid thin line are the fractures associated with the nested summit crater rims (A, B and C) from de Zeeuw-van Dalfsen et al. (2017) and Richter et al. (2018).

entire LP II phase support the common origin of the LP signals (Fig. 3.5). Our results suggest the repetition of a mechanism stationary in time, which is compatible with the oscillation of a vertical conduit or fracture due to gas flux, thereby reflecting pressure fluctuations, as proposed by Chouet (1996). High LP waveform similarity over a long time span was also observed during a long-term period of unrest following the April-May 1999 eruption of Shishaldin volcano, Alaska (Petersen et al., 2006), where the LP events revealed a high level of similarity over several months. Similarly, sustained LP activity at Mt. Etna maintained significant similarity among spectra and waveforms, which agrees with our interpretation of the resonance of a fluid-filled cavity as a vertical conduit (Saccorotti et al., 2007).

3.4.4 Implications for a plumbing system and geothermal fluid path

Our locations show that most LP hypocenters are clustered in the first 2 km below the crater within the dormant edifice next to the active crater. This finding coincides well with the location of a high-conductivity layer 1 km beneath the summit interpreted as fluids within a hydrothermal system resolved by a previous magnetotelluric study (Díaz et al., 2012).

VTs have been located even deeper beneath the volcanic edifice belonging to the VT I and II swarms. The VT I swarm displays stand-alone VT swarm activity neither preceded nor followed by any other seismic or geophysical anomaly. In contrast, VT II precedes the beginning of the long-term LP anomaly. Based on their hypocentral locations, these VTs could be associated with brittle processes accompanying fluid ascent at some depth. Comparatively, a swarm of VTs preceded the LP activity at Campi Flegrei, Italy, associated with a hydrothermal origin (Cusano et al., 2008). Similar to our study, the VTs were rather outspread and occurred at a greater depth, which was interpreted to cause an increase in rock permeability, thus favoring the fluid mobility that caused the LP activity that was followed by an increase in thermal emissions and gas fluxes. Nevertheless, we know very little about the chemical variability of

the hydrothermal system at Lascar, as this is beyond the aim of this study. We conjecture that the spatiotemporal distributions of VT and LP events seem to reflect a process that initiated with deep VT sources associated with the failure of the rock due to the concentration of stress, indicating the first sign of volcano activity, followed by the LP events located at relatively shallow depths, reflecting the instability of the volcanic system and providing early warning of a likely eruption.

Cusano et al. (2008) also found the spatial spreading of LP locations by imaging a sub-vertical path consistent with a fluid-filled crack observed from moment tensor inversion, and their findings are compatible with our results. Despite the depth resolution being lower than the epicentral accuracy of our method, we assume that the LP obtained by waveform cross-correlation delineate a conduit-like geometry down to ~5 km below the summit adjacent to active crater A (Fig. 3.8). This fluid path can be divided into three main zones. The lowest 3 km shows a sub-vertical conduit located beneath the dormant western edifice (Fig. 3.8(a)), whereas the central stretch is characterized by hypocenters arranged in a dipping cluster (Fig. 3.8(b)), and most of the event locations are grouped in the shallowest 1 km in an elongated SW-NE cluster (Fig. 3.8(c)). The VT cluster just beneath the central stretch of LPs supports our previous suggestion about the spatiotemporal distribution of both types of events. We hypothesize that this deviatory path could be associated with the rock permeability attributed to the effect of the VT cluster, similar to Cusano et al. (2008), and possibly attributed to potential stress reorientation causing the migration of shallow seismic activity towards the dormant western edifice (from (d) to (c) in Fig. 3.8). We propose three plausible mechanisms: (1) anisotropy in the bending zone could contribute to the creation of an inclined fluid path, as was confirmed experimentally by Gressier et al. (2010); (2) an unloading effect produced by the deep active crater A could produce the geometrical deviation of the fluid path, as was explained numerically by Maccaferri et al. (2011) and was analogically modeled for dikes propagating beneath calderas by Gaete et al. (2019b); and (3) morphological changes due to constant subsidence and nearly E-W movement of the old nested crater towards the active one (Richter et al., 2018). Now, the remaining question is whether the path imaged through the LPs can also provide us clues about the migration of eruption activity towards the dormant edifice, which would suggest shallow LP locations.

Finally, the seismic data reveal no evidence for a major magma chamber, supporting the shallow hydrothermal system region proposed by Díaz et al. (2012). This could also explain the absence of major edifice-wide deformation in the geodetic data (Pritchard and Simons, 2002), as the observed surface deformation is associated mainly with geomorphological changes (de Zeeuw-van Dalfsen et al., 2017; Richter et al., 2018). In conclusion, the eruption cycle at Lascar volcano appears to be currently driven by the pressurization of a hydrothermal system rather than by a magmatic system.

3.5 Conclusion

In this work, we use the permanent and temporary seismic deployments at Lascar volcano, Chile, to locate and discuss the spatiotemporal evolution of seismicity at this volcano over a time period of approximately 3 years, which includes two eruption events. Following a detailed analysis, the seismicity is characterized mostly by LPs and VTs originating at a relatively shallow depth beneath the volcanic edifice. We compare a range of different location techniques based on amplitude, polarization, coherence and cross-correlation waveform features to better assess the hypocentral locations of the LPs. Three of the four location methods provide results that agree on a shallow region where it is more plausible to find the LPs, while the waveform cross-correlation method depicts absolute and robust events locations with a high epicentral

accuracy but a relatively low depth resolution. The analysis is combined with waveform similarity and clustering evaluations to investigate the spatiotemporal evolution of LP sources and the presence of more waveform clusters, resulting in the resolution of a single type of signal and thus a single process responsible for the LP activity.

The data suggest an alternation between LP quiescence and activity period, this second one potentially preceding the Lascar eruptions. We observed in particular a preparatory period of ~14 months preceding the 2015 eruption (VT II and LP II) starting with the first VT swarm in August 2014 and continuing with a sustained LP activity. The VT sources are located below the volcanic edifice at a depth of 3 km below the summit. We hypothesize that the VT signals are the result of brittle processes accompanying fracturing in response to gas and magmatic fluid transfer from depth to the uppermost plumbing system. The VT activity lasted for approximately 2 months and was accompanied by a subtle increase in LP activity. This LP activity, which continued until the eruption, gradually increased with time, reaching the highest event rate from October 2014 to July 2015. The LPs from the LP II phase are located below the summit and just above the VT seismogenic zone, extending along a narrow sub-vertical region down to a depth of ~5 km that we suggest is the geometry of the volcanic conduit, excluding the presence of a magma chamber. Similar LP waveforms denote the repeated activation of a similar source process throughout the entire LP II phase, compatible with the resonance of a vertical conduit. In the last phase (August to October 2015), the LP activity declined again in preparation for the 2015 eruption. The LP seismicity rate during the last few months before the 2015 eruption was similar to that before the 2013 eruption, which could have implications for a volcanic hazard assessment. According to the evolution of LPs at the time of the 2015 eruption, the volcanic system appeared to have reached similar conditions to those at the time of the 2013 eruption. However, a strong increase in precipitation before the 2015 eruption may have acted as final trigger and may have controlled the eruption dynamics in its final phase.

Chapter 4

Processes culminating in the 2015 phreatic explosion at Lascar volcano, Chile, monitored by multiparametric data

Abstract

Small steam-driven volcanic explosions are common at volcanoes worldwide but are rarely documented or monitored; therefore, these events still put residents and tourists at risk every year. Steam-driven explosions also occur frequently (once every 2-5 years on average) at Lascar volcano, Chile, where they are often spontaneous and lack any identifiable precursor activity. Here, for the first time at Lascar, we describe the processes culminating in such a sudden volcanic explosion that occurred on 30 October 2015, which was thoroughly monitored by cameras, a seismic network, and gas and temperature sensors.

Prior to the eruption, we retrospectively identified unrest manifesting as a gradual increase in the number of long-period (LP) seismic events in 2014, indicating an enhanced level of activity at the volcano. Additionally, sulfur dioxide (SO_2) flux and thermal anomalies were detected before the eruption. Then, our weather station reported a precipitation event, followed by an increase in steaming and a sudden volcanic explosion at Lascar. The multidisciplinary data exhibited short-term variations associated with the explosion, including (1) an abrupt eruption onset that was seismically identified in the 1-10 Hz frequency band, (2) the detection of a 1.7 km high white-gray eruption column in camera images, and (3) a pronounced spike in SO_2 emission rates reaching 55 kg/s during the main pulse of the eruption as measured by a mini-differential optical absorption spectroscopy (DOAS) scanner. Continuous carbon dioxide (CO_2) and temperature measurements conducted at a fumarole on the southern rim of the Lascar crater revealed a pronounced change in the trend of the relationship between the CO_2 mixing ratio and the gas outlet temperature; we speculate that this change was associated with the prior precipitation event. An increased thermal anomaly inside the active crater as observed in Sentinel-2 images and drone over-flights performed after the steam-driven explosion revealed the presence of a ~50 m long fracture truncating the floor of the active crater, which coincides well with the location of the thermal anomaly. This study presents the chronology of events culminating in a steam-driven explosion but also demonstrates that phreatic explosions are difficult to predict, even if the volcano is thoroughly monitored; these findings emphasize why ascending to the summits of Lascar and similar volcanoes is hazardous, particularly after considerable precipitation. [1]

[1] Originally published as: Gaete, A., Walter, T. R., Bredemeyer, S., Zimmer, M., Kujawa, C., Franco, L., San Martin, J., Bucarey Parra C., (2020): Processes culminating in the 2015 phreatic explosion at Lascar volcano, Chile, monitored by multiparametric data. Natural Hazards and Earth System Sciences, 20, 377-397. doi:10.5194/nhess-20-377-2020

4.1 Introduction

Volcanoes possessing an identified region of shallow magma storage often allow the close monitoring of changes associated with deformation, seismicity and degassing activity, and data on all of these processes are highly beneficial for eruption forecasting or early-warning systems (Sparks, 2003). Nevertheless, many volcanic eruptions still occur without clear precursors, highlighting the need to further investigate the types of volcanoes generating such eruptions. For instance, unexpected and sudden phreatic eruptions occurred in 1979 at the Diëng Plateau (Le Guern et al., 1982) and in 2014 at Mt. Ontake (Oikawa et al., 2016), killing 142 and 64 people, respectively. Approximately 85 % of the phreatic explosions that occur worldwide are not followed by the extrusion of magma (Barberi et al., 1992). Thus, the occurrence of such surprising eruptions implies that the responsible processes and their scales are not easily detectable by conventional geophysical and geochemical instrumentation (Barberi et al., 1992). Volcano monitoring networks are commonly designed to detect precursor activity at depth, where the movement of magma causes detectable gravity changes, seismicity, deformation or degassing. Accordingly, eruptions that are associated with very shallow processes, such as phreatic explosions, are naturally difficult to monitor beforehand, since water steam explosions may occur spontaneously, as was identified during the phreatic eruptions at Bandai volcano (Yamamoto et al., 1999), Mt. Ruapehu (Christenson et al., 2010), Mayon volcano (Newhall et al., 2001), Aso volcano (Kawakatsu et al., 2000) and elsewhere (Barberi et al., 1992; Mastin, 1995). Most of the aforementioned volcanoes exhibit a steep morphology, high elevations and/or hazardous access conditions, and hence establishing conventional monitoring systems close to their craters is a challenging task.

Possible precursory signs of phreatic eruptions, if identified, generally occur with short notice and may manifest as seismic tremors (Martinelli, 1990), very long period (VLP) events (Jolly et al., 2010), inflation (Nakamichi et al., 2009), and/or changes in the gas chemistry and temperature of fumarolic emissions (de Moor et al., 2016) only minutes, hours or days prior to an eruption. The detection of such sudden changes requires monitoring by means of an instrument network close to the summit that combines different geophysical and geochemical techniques (Scarpa and Tilling, 2012).

Lascar, Chile (23°22′ S, 67°44′ W, 5592 m), is a steep volcano with relatively easy access that has repeatedly exhibited steam-driven explosions. The explosions at Lascar have scarcely been studied, and therefore little knowledge exists regarding whether these events are characterized by precursor activity. In an effort to better comprehend this hazardous type of eruption, a monitoring network was installed in 2010. A well-monitored volcanic explosion occurred in 2015, which is discussed in detail in this paper.

4.2 Study area and explosive history of Lascar volcano

Lascar volcano, the most active volcano in northern Chile and within the Andean Central Volcanic Zone (Francis and Rothery, 1987; Gardeweg et al., 1998; Tassi et al., 2009), formed in association with the subduction of the Nazca Plate beneath the South American Plate (Jordan et al., 1983). This volcano is located in the Antofagasta region and lies approximately 17 and 34 km from the small towns of Talabre and Toconao, respectively, and 68 km from the touristic city of San Pedro de Atacama. Lascar is an andesitic-dacitic stratovolcano that consists of two overlapping cones, which are aligned ENE-WSW, and hosts five summit craters (Gardeweg et al., 1998) that partially overlap (de Zeeuw-van Dalfsen et al., 2017). Activity of Lascar is characterized by the continuous emission of volcanic gases, smaller steam-driven explosions, the generation of thick lava flows and the expulsion of major ash-loaded clouds during the climax

of an eruption (Gardeweg et al., 2011).

The historical record of Lascar's activity comprises approximately 27 eruptions, almost half of which have occurred in the springtime (mid-September to mid-December; see Table 4.1). The eruptions range from effusive to explosive events, often with phreatic characteristics and the ejection of gas, ash and debris kilometers high into the atmosphere. Additionally, dome building and collapse have been observed (for further details, see Table 4.1). The most recent large eruption had a volcanic explosivity index (VEI) of 4 and occurred on 19-20 April 1993 (González-Ferrán, 1995; Matthews et al., 1997; Siebert et al., 2010). The 1993 eruption was identified as the climax of a longer episode characterized by four cycles of activity initiating in 1984; each cycle was separated by explosive Vulcanian eruptions that commenced with minor phreatic activity until the cycle eventually culminated in a large explosion that ejected incandescent material into the air and produced plinian to subplinian eruption clouds (Matthews et al., 1997). By 1992, a lava dome was identified inside the active crater of Lascar; after the 1993 plinian eruption, a new dome with an andesitic-dacitic composition grew inside the crater (González-Ferrán, 1995). Smaller phreatic and Vulcanian eruptions followed in December 1993 and February 1994. The short-lived explosive eruption in December 1993 was accompanied by seismic activity with an intensity of 3 on the Modified Mercalli Intensity Scale (Global Volcanism Program, 1994). In contrast, the seismic activity associated with the other eruptions was only scarcely felt in the nearby village of Talabre at a distance of 17 km from Lascar (Global Volcanism Program, 1994), implying only low-magnitude seismicity. Following the 1993 eruptive cycle, historical reports document explosions every 2-3 years on average (Table 4.1), with a frequent occurrence of steam-driven explosions. This kind of explosion commonly occurred without any evidence of precursor activity (e.g., seismicity), due to either the lack of precursors or the lack of a sufficiently dense deployment of instrumentation.

This type of eruption is poorly understood for numerous potential reasons; among them, prior to 2010, ground-based monitoring studies were conducted only sporadically at Lascar and were restricted to only short-term (weeks to months) campaign-based fieldwork. Therefore, the preparation phases and periods preceding steam-driven explosions were not documented with adequate instrumentation. Remote sensing, on the other hand, was able to provide evidence distinguishing some unrest periods preceding notable events, such as the 2000 eruption, which was associated with a short-term reduction of thermal emission and a change in the dimensions of the dome area (Wooster, 2001). Similarly, satellite-based observations were employed to assess the dispersion of eruption products during the 2003 and 2005 unrest periods (Aguilera et al., 2006; Viramonte et al., 2006); unfortunately, these studies lacked the ability to identify precursors. Matthews et al. (1997) proposed a continuous deepening of the crater floor associated with a high rate of degassing from fumaroles within the active crater; this deformation was determined by an InSAR investigation (Pavez et al., 2006). Recent InSAR studies also showed that the deformation rate appeared to be largely unaffected by the most recent explosive eruptions in 2013 and 2015 (Richter et al., 2018).

Retrospectively, other studies have been able to identify precursory activity associated with unrest periods. Wooster (2001) described the rapid cooling behavior of the Lascar dome as precursor activity following the 1993 eruption, while a recent study of the 2013 explosion utilized seismic wave interferometry to depict variations in the seismic velocity and consequently speculated about the pre-eruptive deformation of a magmatic/hydrothermal reservoir (González et al., 2016). A shallow hydrothermal system as depicted by magnetotelluric and seismic data (Díaz et al., 2012; Hellweg, 2000) influences the degassing activity of Lascar (Bredemeyer et al., 2018; Tassi et al., 2009). These degassing processes have been suggested to be the source of the tremors observed during the 1994-1995 period of unrest (Hellweg, 2000), and they are probably associated with the increase in long-period (LP) events preceding an eruption (González et al.,

Table 4.1: Historical record of activity at Lascar volcano (Global Volcanism Program, 2013; González-Ferrán, 1995; Siebert et al., 2010).

Start	Duration	Type extrusion	Explosive	VEI
1902	—	—	Y	2?
1933-Oct-09	3 months	—	Y	2
1940	—	—	Y	2
1951-Nov-16	3 months	—	Y	2?
1954-Jun-16	1 month	—	N	2?
1959-Nov-16	7 years, 2 months	—	Y - Phreatic	2
1969-May-16	—	—	N	1
1972-Jul-02	—	—	?	2?
1974-Jul-16	2 months	—	?	1
1984-Dec-16	7 months	dome building	N	0
1986-Sep-14	2 days	15 km ash column	Y	3
1987-Nov-16	2 years, 5 months	dome building and ash cloud	Y - phreatic	3
1990-Nov-24	1 day	1.5 km eruption columns	Y	1
1991-Oct-21	7 months?	dome collapse, dark plume and ashfall	Y	2
1993-Jan-30	7 months	dome collapse, plinian column, bombs ejection and pyroclastic flow	Y - phreatic strombolian explosions	4
1993-Dec-17	2 months	dark gray plume	Y - phreatic	2
1994-Jul-20	6 days	dark and brown columns and small ashfall	Y - vulcanian activity	2
1994-Nov-13	8 months	vapor and ash plumes, black plume	Y - vulcanian and small phreatic eruption	2
1996-Oct-18	1 Day	white-bluish vapor emission	Y	2
2000-Jul-20	6 months	ash emission	Y	2
2001-May-17	2 months	—	N	—
2002-Oct-26	2 days	1.5 km ash plume	Y	2
2003-Dec-09	1 day	fine ash from fumarole	?	1
2005-May-04	1 day	10 km ash cloud	Y - vulcanian eruption	3?
2006-Apr-18	1 year, 3 months	white-gray plumes and ash emission	Y - phreatic	3
2013-Apr-02	7 months	seismicity, glow and gray plume	Y	1
2015-Oct-30	21 days	2.5 km ash plume variable seismicity	Y	2

2016).

Since the end of 2010, a volcano monitoring network has been gradually deployed around Lascar, providing a reliable database which allowed us to investigate the 2015 eruption. In an attempt to better understand the most recent and unexpected 2015 eruption, we compiled a multiparametric data set to study the details of the period preceding this eruption and describe the processes associated with this event. Our study also aspires to demonstrate why this type of volcanic hazard is generally so challenging to forecast.

4.3 Data and analysis methods

Lascar has been monitored by a network consisting of broad-band seismometers, fixed cameras, permanent gas monitoring equipment and a local weather station. Data from this network have been further complemented by satellite-based infrared observations and images of the crater acquired by an unmanned aerial vehicle (UAV). The locations of all ground-based stations and the period analyzed in this study are illustrated in Fig. 4.1. The data treatment and analysis methods implemented in this study focused on the temporal evolution of seismic volcano-tectonic (VT) and LP events, SO_2 fluxes, CO_2 mixing ratios, and temperatures of fumarolic emissions and changes in the brightness of these emissions, thermal changes in the crater, and changes in the surface features of the crater. The instrumentation, data and analysis methods are described in detail below.

4.3.1 Seismic monitoring

The network consists of five permanent seismic stations operated by the Observatorio Volcanológico de los Andes del Sur (OVDAS), the national volcano observatory that continuously monitors over 40 active volcanoes in Chile. The OVDAS stations are equipped with broadband REF TEK 151-30A sensors and REF TEK 130B data loggers that record ground motions at a sampling rate of 100 Hz. Four of these five stations were used to study the evolution of seismicity in the period from July 2014 to December 2015, and their locations are illustrated in Fig. 4.1. However, as three of these stations stopped functioning before October 2015, only one seismic station was operational throughout the month of the eruption and was useful for assessing the timing and characteristics of the explosion, as well as for performing a simple event classification for October 2015 (station QUE; Fig. 4.1).

To investigate the evolution of seismicity at Lascar, we used the entire available earthquake catalog from the volcano observatory. The catalog was constructed by real-time scanning following Lahr et al. (1994) through visual classification performed by OVDAS analysts. The volcanic signals were classified according to their spectral content, harmonic signature, phase arrival times and event duration into one of six categories of signals observed at Lascar: VT, LP, VLP, volcanic tremor (TR), hybrid (HB) and explosion (EX) signals (Chouet, 1996). For our analysis, we considered VT and LP events because they were the most abundant events that occurred during the pre-eruptive phase. Although QUE was the only operational station during October 2015, it provided clear signal records with a sufficiently high signal-to-noise ratio (Gaete et al., 2019a) to distinguish VT and LP signals on the basis of their characteristic spectral contents. Based on these data, we visualized the temporal evolution and characterized the precursor VT events and the eruption signal. This event analysis provided us with a fundamental overview of the stage of activity at Lascar volcano. For a more in-depth seismic analysis, the reader is referred to Gaete et al. (2019a).

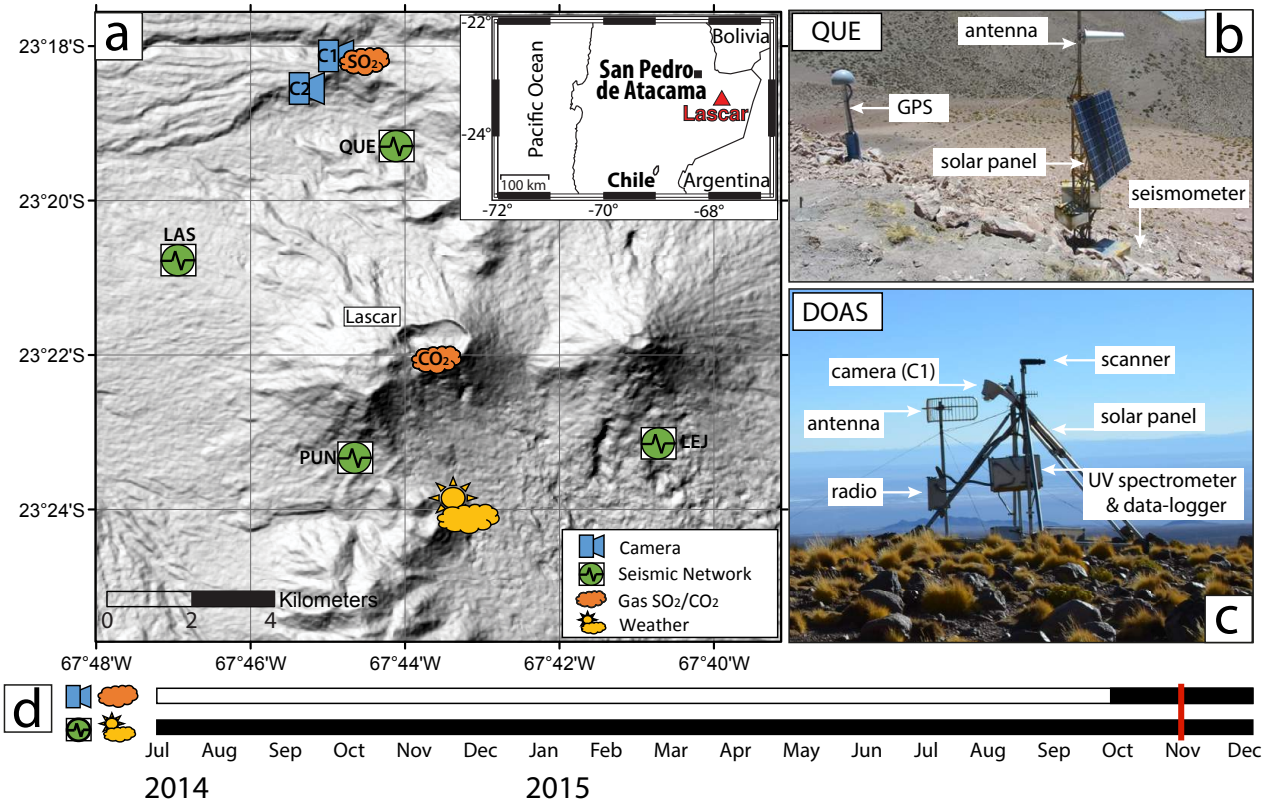

Figure 4.1: (a) Locations of Lascar and the deployed equipment applied in this study. (b) Setup of the seismic station QUE. (c) Setup of the camera (C1) and the mini-DOAS station to measure SO_2 emissions. (d) Time bars depicting the period analyzed in this study for each data set (shown in black). The red line indicates the eruption on 30 October.

4.3.2 Visual data

Solar-powered time-lapse camera stations were installed at two fixed locations to take pictures of the volcanic edifice at regular time intervals. Cameras C1 and C2 look towards the northern flank of Lascar. C1 is a streaming webcam operated by OVDAS and is programmed to capture images at an interval of one image every minute (768 px × 576 px resolution). Camera C2 is a high-resolution digital single-lens reflex (DSLR) camera (2048 px × 1536 px resolution) installed by the GFZ and takes images at an interval of 60 min. Data from C1 and C2 (see Fig. 4.1 for their location) were used to assess the height and duration of volcanic plumes using a kymograph in conjunction with pixel brightness analysis, as explained below.

Vision-based techniques have revealed the value of video data in a variety of applications, such as in smoke and fire detection (Çetin et al., 2013; Healey et al., 1993; Verstockt et al., 2009). Camera-based monitoring networks have similarly become useful for observing plumes, lava movement and the ejection of particles during an eruptive episode (Brook and Moore, 1974; Chouet et al., 1974); in particular, the use of camera-based networks has increased dramatically in many fields of volcano research since the image quality and means of data transmission are continuously improving, thereby allowing nearly continuous monitoring (Orr and Hoblitt, 2008; Paskievitch et al., 2006; Salzer et al., 2016; Walter, 2011). Water vapor is the major component of gases emitted from volcanoes, and the brightness of a volcanic plume has been shown to increase with the upwelling of new magma (Girona et al., 2015). To analyze the pixel brightness and variations in gas plumes, we applied a correction using digital image correlation to ameliorate the shaking of the camera due to strong winds. Subsequently, we applied a masking operation to generate an image containing only the gas plume (see Supplementary material, Fig. S1). Each of these images was converted to grayscale and then transformed

into a matrix, the elements of which represent the intensity values. We summed these matrix elements and normalized the values by the matrix size to compute the total brightness of one image. The results provided a measure of the pixel brightness variations occurring within the gas plume at Lascar volcano. To analyze 2 months of data, we utilized daily images captured at noon, which is when the visibility of the gas plume is the clearest and the position of the sun is constant. To perform a more detailed analysis, we used images produced every hour. The pixel brightness can provide a useful visual constraint on the activity state of a volcano, even though the brightness alone may depend strongly on the position of the sun, presence and strength of condensation, and atmospheric conditions.

We further performed kymograph analysis by extracting the RGB values along a vertical line across the center of the volcano and displaying these values in a time series plot with a data point every minute. The coloration, timing, duration, and height of discrete gas emission pulses and eruption columns can be visualized with kymographs created in this fashion, and thus they have already been extensively used for the analysis of volcano video data in previous investigations (e.g., Munoz-Saez et al., 2015; Witt and Walter, 2017). A geometric conversion from the pixel scale to the meter scale was performed using the high-resolution Pleiades-1 digital elevation model presented by Richter et al. (2018). Due to the large distance from the cameras to the active volcano crater (6.75 and 6.42 km for C1 and C2, respectively), we applied a constant scaling factor to all pixels; thereafter, distortions arising from the lens, camera sensor or field of view were not considered.

4.3.3 Gas emissions

Measurements of the CO_2 concentration and gas temperature were conducted at a low-temperature fumarole on the southeastern crater rim of Lascar volcano (Fig. 4.1). The gas temperature was monitored by means of thermocouples using an industrial platinum resistance temperature detector (RTD, PT 100, Labfacility, UK), and the CO_2 concentration was measured by means of a Vaisala CARBOCAP®Carbon Dioxide Probe (GMP343, Vaisala Oyj, Finland). The data from both sensors were recorded at 1 min intervals with an ADL-MX Advanced Datalogger (Meier-NT GmbH, Germany). The analog digital converter has an accuracy of 0.01%.

The CO_2 sensor, which has an accuracy of ±5 ppm, was successfully used in Chile in a previous study to correlate the volcanic activity with atmospheric changes (Zimmer et al., 2017). The temperature sensor, which can be applied in a range between −50 °C and 450 °C at an accuracy of ±0.06 °C, was inserted to a depth of ~35 cm into the fumarole. Residual temperatures were calculated by subtracting the mean temperature at the time of investigation from the actual reading.

Additionally, SO_2 emission rates were remotely monitored using a scanning mini-differential optical absorption spectroscopy (DOAS) station deployed by OVDAS 6.75 km north of the active crater (Fig. 4.1); the mini-DOAS station yielded one complete scan across the gas plume every 5-15 min depending on the light conditions.

SO_2 slant column densities (SCDs) along the viewing direction of the mini-DOAS scanner were retrieved in the wavelength range of 310–325 nm by means of DOAS (Galle et al., 2010; Platt and Stutz, 2008); the spectra measured inside the gas plume were compared with a gas-free spectrum and the pixel-wavelength-calibrated SO_2 absorption spectrum from Vandaele et al. (1994), which was convolved with the slit function of the spectrometer. Furthermore, we incorporated an O_3 absorption spectrum (Voigt et al., 2001) and a ring spectrum in the DOAS fit to avoid interference with absorption by ozone and scattering effects. Plume transport velocities and plume altitudes, which are required to calculate the gas flux from SO_2 SCD profiles, were estimated using the wind speeds derived from archived weather data provided by

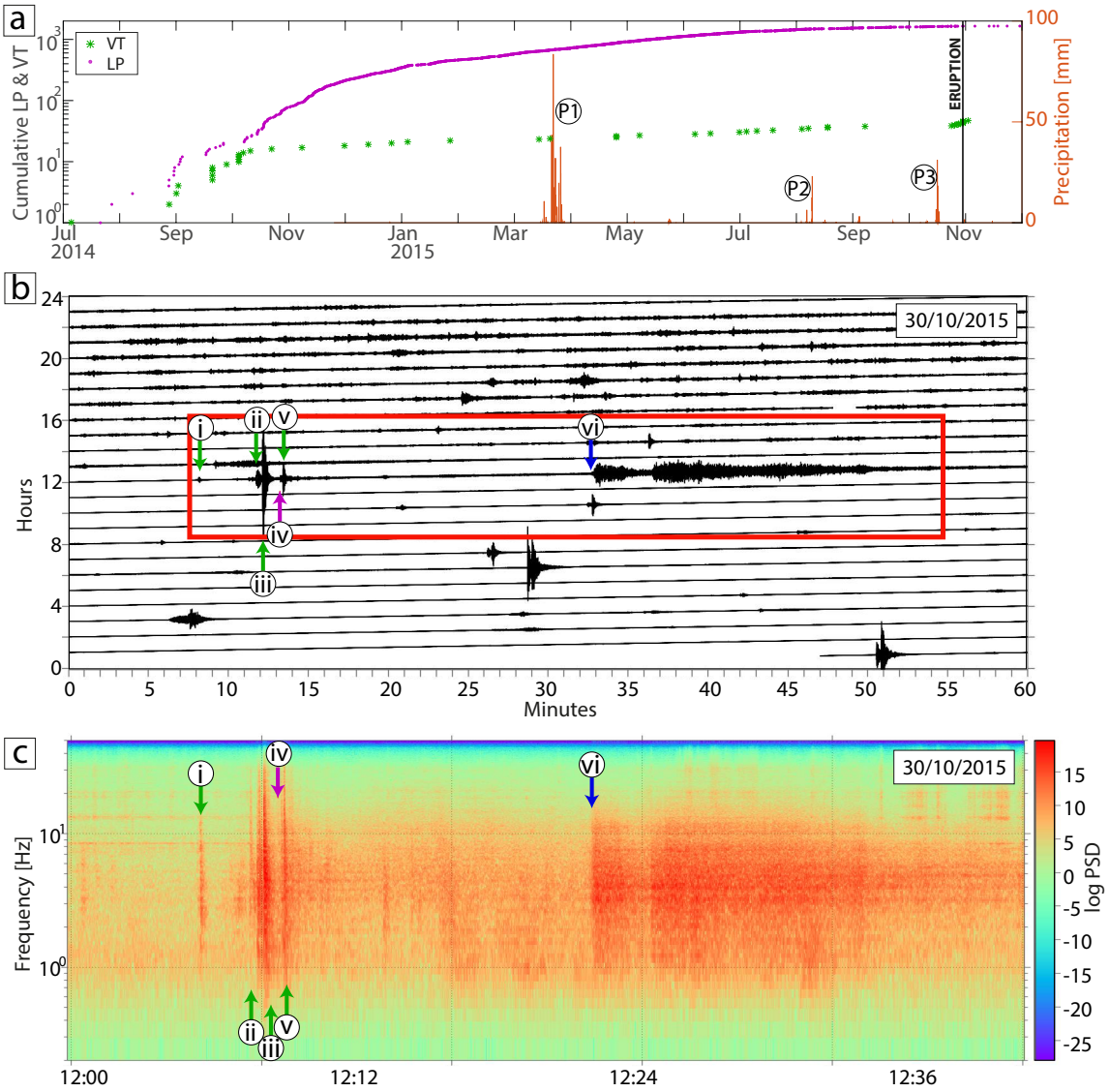

Figure 4.2: (a) Temporal evolution of seismicity characterized by LP (purple dots) and VT (green stars) events, and precipitation events from July 2014 to December 2015. Cumulative LP events show a permanent increase starting 1 year before the eruption and a slight decrease 3 months before the eruption. VT events do not show any evolution pattern but cluster around the eruption. P1-P3 represent three exceptionally strong precipitation events that occurred during the study period; P3 is the suggested trigger of the eruption. (b) Seismic record from 30 October 2015. The red box indicates the window covered in (c) and shows the VT (i, ii, iii, v green arrows) and LP events (iv purple arrow) preceding the eruption and the eruption signal (vi blue arrow). (c) Spectrogram depicting the frequency band covered by the VT and LP events as well as the eruption tremor. The events that occurred early in the morning outside the red box in (b) are regional tectonic events located more than 100 km away from the volcanic area; therefore, there is no certainty that they could have affected the volcanic system.

the National Oceanic and Atmospheric Administration's (NOAA) Global Forecast System and using information obtained from pictures taken by the time-lapse cameras, respectively. The direction of plume transport was further determined by means of triangulation using the SCD profiles in combination with plume height estimates.

4.3.4 Thermal anomalies

To investigate thermal anomalies, we used satellite images acquired by Sentinel-2, an Earth-observation satellite from the European Unions (EU) Copernicus program. Sentinel-2 was

launched on 23 June 2015 and became operational later in 2015; since August 2015, it has systematically acquired imagery of Lascar volcano at a high spatial resolution (up to 10 m). Sentinel-2 acquires multispectral data comprising 13 bands in the visible, near-infrared and shortwave infrared range of the electromagnetic spectrum. In this study, we utilized bands from the near-infrared part of the spectrum to ascertain the variations in the appearance and dimensions of the thermal anomaly inside the currently active crater of Lascar.

Here, we processed the Sentinel-2 data using the SNAP toolbox (S2TBX), which is freely provided by the European Space Agency (ESA), and we used the 12-11-8A band combination to derive a false-color RGB image representing the apparent temperature of the ground. These bands allow the perimeter of the thermal anomaly located inside the Lascar crater to be mapped and further reveal the presence (or absence) of snow at the volcano summit.

4.3.5 Aerial photography

UAVs were employed to obtain high-resolution nadir photographs of the Lascar crater, which is partially hidden from the human eye by the rim of the crater. Due to the high elevation of the volcano (>5500 m), the first successful drone flight, that is, the first drone that did not crash, was launched in November 2017. The motivation of this overflight was to determine the morphological features of the active Lascar crater. We used a DJI Mavic Pro Platinum quadcopter drone equipped with a 12Mpx cropped-sensor camera (4000 px × 3000 px 35 mm focal length, ISO 100), which was programmed to take images at an interval of 2 s, and the flight speed was 5 m/s. The drone was launched from the southern rim of the active crater at 5502 m a.s.l. (above sea level), after which it was flown to an altitude of 5700 m a.s.l. and then over the crater in a northerly direction. From the 250 drone images acquired during the flight, we constructed a photomosaic and a hillshade using the structure from motion (SfM) workflow implemented in the Agisoft Metashape Professional software package. Over 20000 tie points were identified for image matching, allowing us to generate a dense cloud consisting of over 7 million points; from this point cloud, a digital elevation model with a 20 cm resolution and an orthomosaic map with a 7 cm resolution were produced. As no ground control could be obtained, we relied on the geolocations of the DJI geotagged camera images only, leading to an apparent image error estimate of 0.6–1.3 m and a total error of 1.25 m.

4.3.6 Weather data

Hydrometeorological conditions were monitored by a weather station (Vaisala WXT520) located at the base of the volcano (Fig. 4.1); this station recorded the atmospheric pressure and temperature conditions, wind direction, wind speed, humidity, and intensity and accumulated amount of precipitation at a sampling rate of one measurement per minute. The data acquisition was temporally synchronized by means of a Global Positioning System (GPS) device, and the data were collected in the field by a Wi-Fi network and transmitted both to GFZ in Germany and to OVDAS in Chile.

We considered the intensity and accumulated amount of precipitation measured in a 1 min running average of rain and hail derived from samples acquired every 10 s. The rainfall is measured as the cumulative amount of water impacting on a 60 cm^2 collecting area with a measurement range of 0 to 200 mm/h, whereas hail is measured as the cumulative amount of hits against the collecting surface. This instrument is not designed to measure snowfall. The data were compared with the other observations to identify a rare precipitation event shortly before the 2015 explosion.

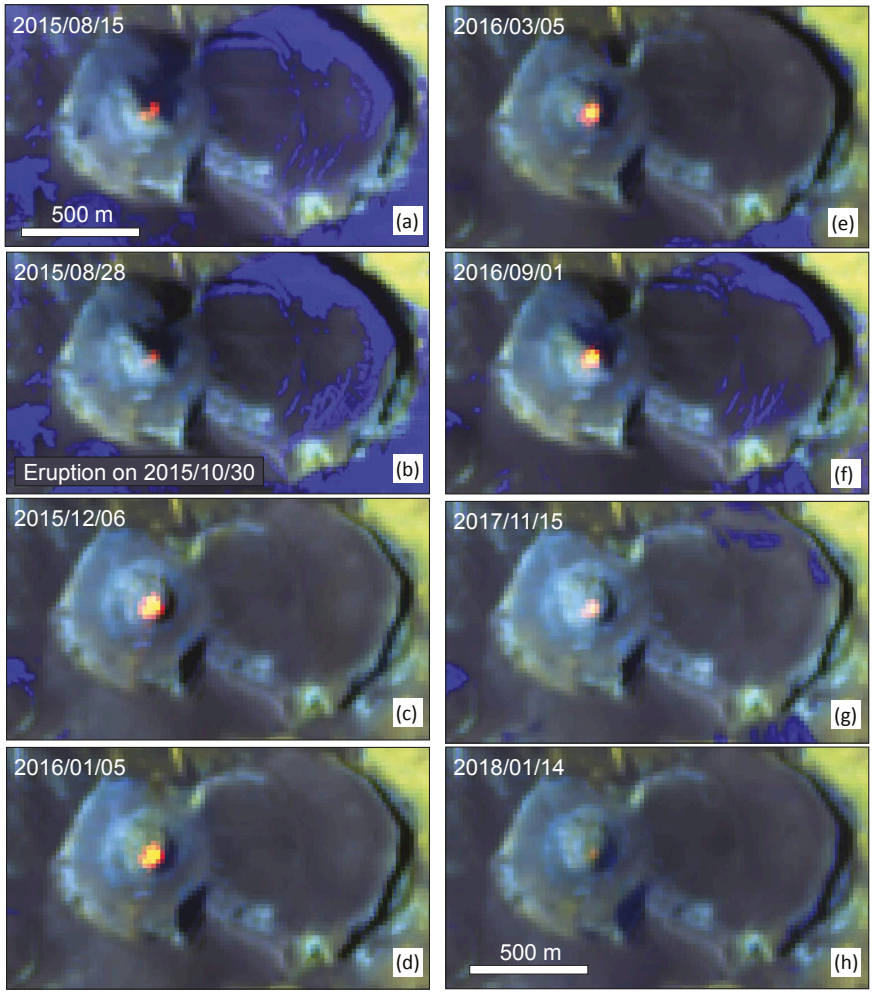

Figure 4.3: Satellite thermal anomalies (high temperatures are shown in red, while cold temperatures and snow are shown in blue) retrieved from Sentinel-2. The availability of data is irregular in 2015, but the data show a gradual decrease in the thermal anomaly in August 2015 and a later increase in the thermal anomaly on 6 December 2015, followed by a gradual decrease. Note that between 28 August 2015 and 6 December 2015 no clear Sentinel-2 images were acquired. (g) shows the thermal anomaly during the time of our UAV field campaign shown in Fig. 4.7. Data provided by the European Space Agency (ESA).

4.4 Results

First, we describe the gradual changes leading up to the eruption; second, we document the changes associated directly with the eruption; and, finally, we discuss the data retrieved in the aftermath of the eruption.

4.4.1 Gradual changes prior to the eruption

We analyzed the seismic catalog over the period from July 2014 to December 2015 to obtain an overview of the activity preceding the eruption at Lascar (Fig. 4.2a). In total, 1654 LP events (purple dots in Fig. 4.2a) and 47 VT events (green stars in Fig. 4.2a) were identified during this observation period. A gradual increase in the number of LP events started in October 2014, i.e., approximately 1 year before the eruption. This increase in LP events was not associated with any relevant changes in the VT event rate. The peak in the LP event rate was found during April-July 2015, i.e., approximately 3-6 months before the eruption. In these months, the LP activity declined from ~11 events to ~1 event per day. At the same time, the persistent thermal anomaly on the crater floor observed in the Sentinel-2 imagery gradually decreased in

both size and intensity (Fig. 4.3a and c), confirming an apparent decrease in thermal activity.

Precipitation is rare in this desert area with an annual average below 100 mm (Messerli et al., 1993). Nevertheless, from the continuous precipitation records recorded at the weather station situated at the base of the volcano, we observed three precipitation events occurring in the period analyzed in this study (P1-P3, Fig. 4.2a). All three precipitation events were associated with abundant snowfall as was observed by our cameras. Our weather station detected considerable amounts of precipitation (rain, hail) during events P1 and P2, which occurred in the middle (March 2015) and end (August 2015) of the increasing LP activity phase, respectively. The same was true for event P3, which occurred from 19 to 21 October 2015 with 112 mm of accumulated precipitation and reached 13 mm/h on 20 October 2015, only 10 days before the eruption. The latter precipitation event was forecasted by the Chilean meteorology agency, prompting an emergency alert on 18 October from the Chilean National Emergency Office (ONEMI) due to the severe weather warning throughout the entire region of Antofagasta. Indeed the maximum level of precipitation that was recorded in the Andes was observed in the first 12 h of 19 October 2015 (ONEMI, 2015).

Events P1 and P2 did not lead to detectable changes in volcanic activity. In contrast, event P3 entailed a pronounced increase in plume visibility, as reflected by the strongly enhanced pixel brightness in the atmospheric column above the active crater. Thus, focusing our analysis of the daily changes of the plume to 1 month before and after the eruption on 30 October 2015, we observed low pixel brightness variations during the pre-precipitation phase (Fig. 4.4a). Just after the event P3, the pixel brightness suddenly increased, indicating the presence of abundant condensed water within the gas plume on 21 October 2015 (Fig. 4.4a), and the maximum pre-eruptive peak was reached on 23 October 2015. These findings were confirmed upon closer inspection of the hourly variations in the brightness (Fig. S2), and the maximum value was revealed to be 4 times the normal state. Fig. S2 also displays the daily cyclic fluctuations of the pixel brightness; these fluctuations were confirmed through visual analysis of the height and brightness of the plume in Fig. 4.5d, in which a stronger signal is observed during the morning hours before transitioning to a slight manifestation of the plume in the afternoon.

Furthermore, the temperature of the fumarolic gas emissions clearly dropped from 33 to 29.2 °C, and some slight variations were evident in the CO_2 concentration after precipitation event P3; both of these trends seemed to be insignificant with respect to the amplitude variations in the long-term trends of their corresponding time series (Fig. 4.4b and c). Similar to the fumarolic temperature, the SO_2 emission rates during October decreased from an average of 4.14 kg/s SO_2 in the period prior to event P3 to merely 2.33 kg/s SO_2 in the 8 days following event P3 (Fig. 4.4d). A renewed pulse of VT events began on 23 October and continued during the following days until the eruption, whereas LP events continued to follow the declining trend observed in the preceding 3 months (Fig. 4.4e).

4.4.2 The phreatic eruption on October 30, 2015

The phreatic eruption that occurred on 30 October 2015 was reported at 09:32 LT (local time) (12:32 UTC); the explosion expelled an ash plume that rose to approximately 1.7 km above the crater and then drifted towards the northeast, as revealed by the webcam and kymograph (Fig. 4.5b).

Approximately 25 min before the explosive eruption, a cluster of four VT events was recorded within a 5 min time window (Fig. 4.2b). These VT events lasted for less than 10 s each, and the corresponding signals displayed characteristic frequencies in the range from 1 Hz to 30 Hz. The eruption was characterized by the sudden onset of a harmonic tremor signal that lasted for approximately 50 min, with the most energetic phase occurring during the first 20 min (Fig.

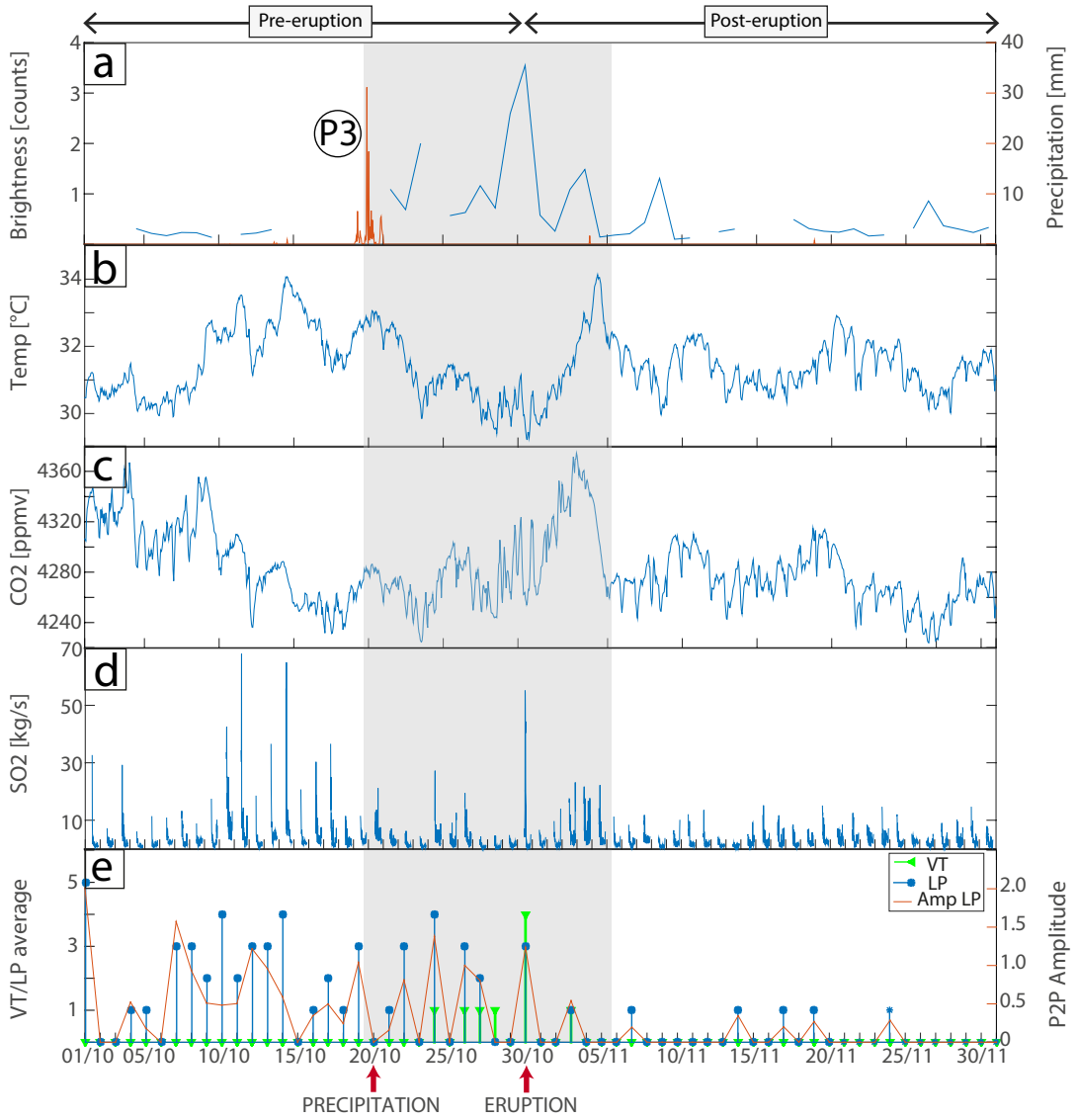

Figure 4.4: Two months of daily variations shown in multiparametric plots of data. a) Brightness (blue curve) of the fumarole computed at noon and precipitation (orange curve for P3, see Fig. 4.2), b) fumarole (blue) temperature, c) CO_2 mixing ratio, d) SO_2 emission rate (note that the data show a peak during the eruption), and e) VT/LP seismic event average and LP peak-to-peak amplitude (orange curve). Precipitation event and eruption days are indicated with arrows at the bottom. The shaded box indicates the period covered from the onset of precipitation event P3 to a few days after the eruption, during which high variability was observed in the gas plume and seismicity.

4.2b and c). This signal was characterized by a frequency content between 1 Hz and 10 Hz and a dominant frequency of 4 Hz. The eruption signal featured two parts, and the transition between the two seems to indicate two phases (Fig. 4.2c). The first part of the eruption signal lasted for 5 min and decreased strongly both in amplitude and in energy during the last 2 min. The second part lasted for approximately 10 min and was characterized by a modulation, i.e., a slowly decreasing amplitude (Fig. 4.2b and c). Throughout the remaining 30 min of the eruption, the tremor exhibited a low energy and amplitude.

The phreatic eruption was accompanied by a degassing pulse, which was reflected by an 8-fold increase in the SO_2 emission rate (Figs. 4.4d and 4.5d). The average SO_2 emission rate was 6.76 kg/s during the morning hours prior to the eruption event, and the first SO_2 emission peak of 55.14 kg/s was reached at 09:26 LT (12:26 UTC), which was approximately 6 min prior to the onset of the phreatic explosion. The corresponding optical SO_2 densities in

the plume center (i.e., the SO_2 concentrations along the viewing direction of the mini-DOAS scanner) started to increase considerably from 200 to 650 ppmm (parts per million meters) approximately 15 min before the eruption and reached a maximum of 766 ppmm approximately 5 min in advance of the ash emissions (Table S3 in the Supplement). Thus, the four VT events that occurred between 25 and 20 min before the eruption were almost immediately followed by a vigorous increase in degassing activity. Subsequently, the SO_2 flux reached a second maximum of 44.38 kg/s at 10:05 LT (13:05 UTC), approximately 32 min after the onset of the eruption, and then gradually declined until it eventually returned to its pre-eruptive value of 6.7 kg/s at 10:59 LT (13:59 UTC), i.e., approximately 29 min after the eruption tremor ceased. The corresponding SO_2 SCDs similarly reached a second maximum of 650 ppmm concurrently with the fluxes before gradually diminishing to usual values. In contrast, the CO_2 concentration and temperature of the summit fumarole abruptly decreased from respective values of 4320 ppm CO_2 and 31.2 °C, in the evening hours of 29 October; reached local minima of 4250 ppm CO_2 and 29.2 °C throughout the duration of the eruption; and subsequently increased again to 4320 ppm CO_2 and 30.8 °C in the evening hours of 30 October (Fig. 4.4b and c). The co-eruptive CO_2 minimum was further accompanied by a pixel brightness peak, exhibiting the presence of condensed water in the eruptive plume (Fig. S2); this dynamic is a recurrent feature in the entire period illustrated in Fig. S2.

A strong steam signal was observed in the two cameras beginning early in the morning of 30 October, as was also depicted by kymographic analysis (Fig. 4.5d). A cyclic daily variation in the steam plume, which decayed in height and intensity from late morning to afternoon, was evident. During the explosion, the plume turned gray and exhibited three phases based on changes in the color and altitude. At the start of the eruption, there was a short lapse when the plume was light gray and reached ~6.3 km a.s.l. (P-I in Fig. 4.5d). This phase was followed by the main eruptive phase, during which a dark-gray and taller plume (~7 km a.s.l.) with a high ash content was expelled (P-II in Fig. 4.5d). These two pulses were associated with the two parts we observed in the eruptive tremor signal described above. The final phase consisted of an isolated light-gray pulse that reached ~6.7 km a.s.l. (P- III in Fig. 4.5d). This third pulse seems to stand alone, and no change in the seismic signal was registered in this regard.

4.4.3 Post-eruptive observations

The seismic, thermal and degassing anomalies detected shortly before and during the 30 October 2015 eruption very quickly returned to their background levels. For instance, the number of LP seismic events per day decreased to few or no events and displayed a very low peak-to-peak amplitude (Figs. 4.2a and 4.4e). The Sentinel-2 data show a hot spot centered in the active crater and that the size and intensity of the surface thermal anomaly on the crater floor had increased in the first acquisition after the eruption (recorded on 6 December 2015; Fig. 4.3d). This initial high temperature of the crater floor is also reflected by the camera images showing a glow at night after the eruption (Fig. 4.5c). The dimensions and strength of the thermal anomaly slowly declined during 2016, as observed in the Sentinel-2 data (Fig. 4.3e-h). By the end of 2017, the thermal anomaly had returned to levels approaching those observed prior to the 2015 eruption (Fig. 4.3i and k).

The gas data from the monitored fumarole on the crater rim displayed pronounced changes. We first found an increase in the temperature from 29.2 °C to 34.2 °C in the 3 days after the eruption until 2 November 2015 and an increase in the CO_2 concentration from 4250 ppm to 4370 ppm until 5 November 2015, both of which gradually approached background levels again ~5 days after the eruption (Fig. 4.4b and c). According to an analysis of the camera brightness, the degassing also gradually returned to its background level by 9 November 2015, when it dropped to usual pre-precipitation values (Fig. 4.4a). The SO_2 fluxes during the

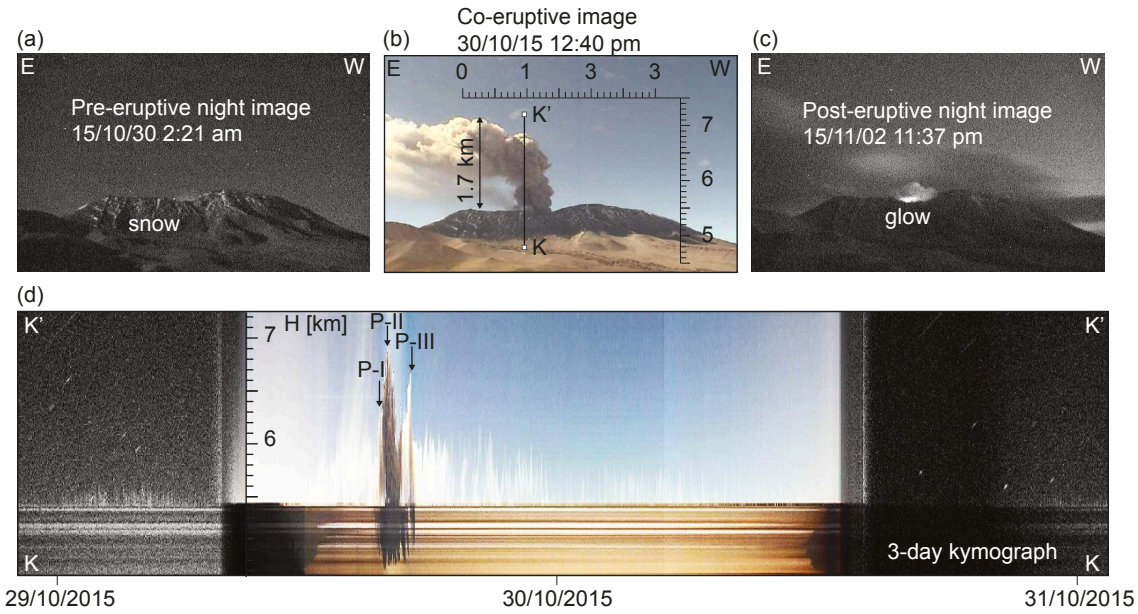

Figure 4.5: Camera data analysis allowing the eruption duration and height to be estimated from a camera looking from north to south (C1; see Fig. 4.1 for location). (a) Pre-eruptive nighttime image (29 October 2015, at 23:21 UTC) of the snow-covered edifice. Local time is given in the image. (b) Co-eruptive daytime image (30 October 2015, at 15:40 UTC) with a 1.7 km high ash-loaded eruption column. (c) Post-eruptive image (3 November 2015, at 02:37 UTC) showing increased glow. (d) Three-day kymograph extracted from 2880 images along vertical profile $K - K'$ (see vertical line in b); the height scale (H) is shown in kilometers above sea level. P-I, P-II and P-III are the three phases exhibited by the eruptive plume.

period of 2-5 November 2015 were measured at an average of 4.42 kg/s and were therefore slightly higher than the average (2.32 kg/s) during the entire post-eruptive period considered here (31 October to 31 November 2015) (Fig. 4.4d).

Our UAV overflight performed on 27 November 2017 revealed the presence of a circular feature located at the base of the deep crater floor with a diameter of ~57 m and partly covered by rockfall deposits from the crater walls (Fig. 4.7a and c). The circular feature on the crater floor may represent the surface expression of the underlying conduit and/or the remnants of a dome-like protrusion of magma, with a mound-like outline, morphology and blocky appearance at the surface. We compared the location of the circular feature to a Sentinel-2 map acquired during the 2015 eruption, and good agreement was observed between the region covered by blocky material and the thermal anomaly region (Fig. 4.7a and b). Close-up views enabled by high-resolution drone photogrammetry further revealed the presence of a linear structure oriented NE-SW dissecting this circular feature but not dissecting the apparently younger rockfall deposits (Fig. 4.7d). The explosive dissection of crater floors and lava domes by linear structures has been observed elsewhere following steam-driven explosions (Darmawan et al., 2018a; Walter et al., 2015). Therefore, we speculate that the linear NE-SW-striking structure developed during the 2015 steam-driven explosion of Lascar volcano.

4.5 Discussion

The steam-driven explosive eruption of Lascar on 30 October 2015 was the first to be densely monitored. The eruption was studied by utilizing different data sets, the results of which suggest that (i) no magma movements within a shallow magma reservoir were identifiable immediately prior to the explosion although significant changes in degassing activity were observed and (ii) the spontaneous steam-driven explosion was directly associated with a brief degassing pulse

and the development of a fractured circular feature on the crater floor. We ascertained that the volcano was in an elevated stage of activity, as the steam explosion was preceded by ~1 year of enhanced LP seismic activity, thus favoring a potential gradual pressure buildup within the shallow volcanic system. However, as the seismic activity gradually declined approximately 4 months prior to the explosion (Fig. 4.2a), a direct and causal relationship is debatable. Nevertheless, similar long-term trends in LP activity have been observed prior to eruptions of Mt. Etna, where variation in the trends was associated with replenishment with gas-rich magma (Patanè et al., 2008). If this was also the case at Lascar, this would imply a considerable input of deep gas/fluid into the system and that the release of this gas/fluid may eventually have been obstructed by a reduction in permeability of the degassing path in response to precipitation (Heap et al., 2019), increasing the pressure in the volcanic system. We noticed that this decline in seismic activity was accompanied by a reduction in the apparent temperature anomaly located inside the active crater (Fig. 4.3a-c), which was likely associated with a general decline in fumarole activity. Similar decreases in the area and intensity of hot spots have previously been observed preceding certain eruptions, such as those occurring in the periods 1992-1995 and 2000-2004 (see Table 4.1), which were interpreted to be associated with a sealing of the degassing path due to crater subsidence (González et al., 2015; Wooster and Rothery, 1997). The details of our findings, the limitations and interpretations of this study, and a conceptual model are discussed below.

4.5.1 Water infiltration into the hydrothermal system of Lascar

Different processes may drive phreatic eruptions; for example, magma may intrude wet sediments and aquifers, lava or pyroclastic flows may interact with surface water, or hydrothermal systems may form during periods of repose (Barberi et al., 1992; Rouwet et al., 2014). Moreover, evidence that precipitation can trigger volcanic activity has also been documented, such as the dome collapse at Soufrière Hills volcano, Montserrat (Carn et al., 2004; Matthews et al., 2002); a seasonal response of seismic velocity (Sens-Schönfelder and Wegler, 2006); the increase in seismicity associated with the precipitation-influenced degassing process at Merapi volcano (Richter et al., 2004); and possible phreatic eruptions that induce dome collapse (Darmawan et al., 2018a).

The hydrothermal system of Lascar has previously been extensively studied (Menard et al., 2014; Tassi et al., 2009). Gas emissions occurring at the crater floor have been previously characterized by the discharge of fluids fed by a deep magmatic source. Lascar hosts an extended hydrothermal system feeding the fumaroles located on the inner crater walls and the upper rim of the crater (González et al., 2015). The gas emissions from these fumaroles show an increasing hydrothermal chemical signature with increasing distance from the magmatic body. Therefore the hydrothermal system encompasses a central magma-dominated system and a peripheral meteorically dominated system which is susceptible to interactions with meteoric water added to the system (Tassi et al., 2009). Our study supports a link between these two systems, as we show evidence that fumarole measurements taken on the outer crater rim display changes related to both the precipitation event and the steam-driven explosion that occurred deep in the crater (see Sect. 4.5.4). Therefore the outer and inner hydrothermal systems appear to be dynamically linked, either to eruption occurrences or to precipitation events, or to both as our study suggests (see also Fig. 4.6). This finding has important implications, as monitoring the outer system, which is easy to access, may indirectly reflect the inner hydrothermal system.

Nevertheless, we note that the historic activity of Lascar provides evidence for at least six phreatic eruptions and that approximately 50% of all recorded eruptions occurred in the period from mid-September to mid-December possibly following precipitation events (Table 4.1), thereby showing a possible seasonal dependence similar to that observed elsewhere in the Andes

(Bredemeyer and Hansteen, 2014; Mason et al., 2004). Likewise, the October 2015 eruption falls within this period and occurred only a few days after a precipitation episode. Another seasonality effect of volcano eruptions was also inferred in Iceland, where most large eruptions occur during spring and summer periods (Albino et al., 2010).

Furthermore, we note that, in our observation period, two other precipitation events occurred in March and Au- gust 2015 (P1 and P2, respectively, Fig. 4.2); event P1 was larger than any other precipitation event in that year and occurred during a period of high (or even peak) seismic activity at Lascar. Why this event with such considerable precipitation did not trigger a phreatic explosion and why it was not associated with any other changes in degassing or VT seismicity remain puzzling. However, our study shows that the explosive eruption at Lascar occurred during a phase of crater floor subsidence that was identified by InSAR (Richter et al., 2018); thus, a possible explanation may lie in the timing of event P3.

Event P3 was associated with 112 mm of accumulated precipitation over 3 days, which is comparable to the average precipitation of 100 mm/yr typically observed, for example, at the ALMA observatory (over 5.000 m a.s.l. and 40 km north of Lascar volcano). Our IP cameras furthermore showed the occurrence of snow in addition to the rain and hail recorded by our precipitation sensor and that the melting of snow following event P3 was rapid and occurred within 3 days, whereas the melting following events P1 and P2 was much slower, and snow cover was still visible even after 10 days. The precipitation associated with the P3 event likely percolated into the shallow hydrothermal system, triggering a phreatic explosion during a period of low seismic activity. Similarly, major explosive eruptions elsewhere have not necessarily occurred during peak volcanic activity and maximum precipitation but occurred during a period when the deep percolation of water was no longer inhibited by lava extrusion (Darmawan et al., 2018b).

Our analysis of different data sets over the 1 month prior to the eruption and the 1 month after the eruption allowed us to recognize precursory anomalies in the VT seismicity and the brightness of the volcanic plume; these anomalies led us to suggest a relationship with the precipitation of event P3. The maximum pre-eruptive brightness was followed by the reactivation of VT activity, which was delayed by 1 day, and was accompanied by continuous fumarole cooling in response to the infiltration of external water; during this period, the cooling rate and depth of penetration were correlated with the amount of precipitation and soil cracks (Zimmer et al., 2017).

Phreatic volcano explosions typically occur without any precursors (Stix and de Moor, 2018). These types of eruptions are similarly believed to occur without precursors at Lascar, a volcano with frequent and well-documented phreatic explosions. Two different end members of phreatic eruptions have been identified by Stix and de Moor (2018): those associated with a deeper hydrothermal system (type 1) and those associated with a near-surface hydrothermal system (type 2) that also includes surface waters. Lascar volcano is known for its lively history of violent hydrothermal explosions, and our observations suggest that the 2015 eruption was a type-2 phreatic explosion according to the Stix and de Moor (2018) classification scheme. Thus, we discuss a possible trigger for this event due to the infiltration of meteoric water through cracks produced by subsidence of the crater floor. This liquid water was stored at shallow levels and vaporized by hot rocks, which led to the explosion.

A short-term increase in VT activity was observed in direct association with the eruption, after which the VT activity rapidly declined. The absence of VT events from the record almost 2 months prior to the eruption suggests that the event that occurred on the 24th and those that occurred throughout the following days were signs of fracturing caused by an increase in pressure following the percolation of meteoric water into Lascar's hydrothermal system. For example, VT events preceded the 2007 phreatic eruption of Mount Ontake, Japan (Kato et al.,

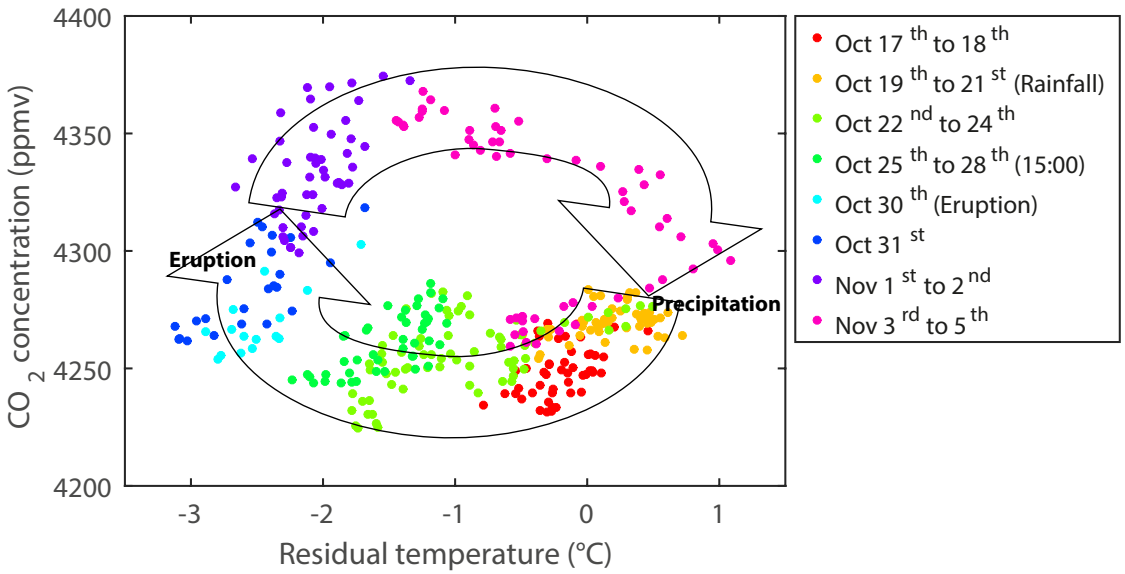

Figure 4.6: Evolution plot of the CO_2 mixing ratio versus the gas temperature measured at a Lascar fumarole from October 17 to November 5, 2015. The distinctive colored dots represent key stages in the evolution of these parameters characterized by a clockwise behavior. This cyclic behavior was induced by precipitation event P3 (October 19-21; orange dots), causing 1) the gas outlet temperature to decrease following the rainfall event and 2) the CO_2 mixing ratio and outlet temperature to gradually rise subsequent to the eruption (October 30; cyan dots). The cycle closes during the period of November 3-5 (magenta dots), during which the CO_2 concentration and gas outlet temperature returned to their pre-eruptive values.

2015), which was associated with the infiltration of hot fluids from the hydrothermal system. At Lascar, the short-term increase in VT activity occurred during an increase in the pixel brightness observed by the cameras; both of these phenomena may indicate the formation of new cracks exposing the previously sealed hydrothermal system.

Moreover, the addition of percolating water into the system could have led to a strong dilution or reduction in CO_2 emissions in response to an increased groundwater content, resulting in an anticorrelated relationship between the steam brightness and the CO_2 concentration (Fig. S2). This dynamics was previously discussed as being the result of an atmospheric pressure reduction governing the boiling tempera- ture of water and consequently increasing the vaporization of water in shallow aquifers (Zimmer et al., 2017). The only comparison in this regard was performed for SO_2 (Girona et al., 2015), where a very similar trend was observed in the steam brightness and the SO_2 column abundance curves acquired simultaneously during a very short (30 min) passive degassing period at Mount Erebus, Antarctica. The correlation between the SO_2 and brightness time series reflects the fact that volcanic water vapor is typically emitted in proportional amounts to the SO_2 and CO_2 abundances in the plume in the short term and under normal conditions. This concept can provide an idea about the parametric relationship between the water and gas contents in fumaroles. For our results, the most plausible interpretation suggests that the percolating water added to the system needed some time to heat up. Therefore, we observe a gradual increase in vaporized water over the 5 days preceding the eruption, the excess of which is evidenced by the relatively white color of the fumarole steam. The gradual increase observed during the 3 days immediately following precipitation is likely associated with the vaporization of water (Fig. S2).

The rapid fumarole heating after the eruption and the short-lived increase in the CO_2 concentration (Fig. 4.4b and c) may be interpreted as a response to the open conduit resulting from the fracture truncating the central elevation on the crater floor due to the eruption. Previous studies have described rainfall-triggered structural destabilization and lava dome collapse and their thermal-hydraulic mechanisms (Elsworth et al., 2004; Hicks et al., 2010; Matthews

and Barclay, 2004). The remaining linear feature observed across the central elevation that we believe formed during the 2015 eruption could provide evidence of a pressure buildup and an explosion of the system (Fig. 4.7b). This would allow for the existence of a persistent thermal anomaly, as is evidenced from satellite data even after 1 year (Fig. 4.3), and the appearance of a glow from the crater the night after the eruption (Fig. 4.5), which was still observable on the night of 2 November according to the kymographic analysis (Fig. S3a). This finding also favors the mechanism in which degassing transports more energy through hot fumarolic gases as a result of a higher magmatic gas flux into the atmosphere. The entire gas pulse accompanying the eruption expelled at least 170 t of SO_2 in only 100 min, which is approximately half the amount of SO_2 that Lascar volcano usually emits throughout a whole day in a noneruptive period (Tamburello et al., 2014; Bredemeyer et al., 2018). Using the molar ratios of Tamburello et al. (2014), we calculate that at least 5440 t of H_2O and 230 t of CO_2 were also released during these 100 min.

This large mass of emitted gas detected from the ground was nevertheless dwarfed by the estimated 49 kt of emitted SO_2 in the eruption cloud recorded by the Ozone Monitoring Instrument (Global Volcanism Program, 2016). The enormous discrepancy between these two measurements may be attributed to the high aerosol contents (condensed water droplets and ash) that were present in the proximal portion of the volcanic plume but rapidly diminished with increasing distance from the emission source (Fig. 4.5b) due to the downwind evaporation of water droplets and the gravitational settling of ash. It is thus very likely that the near-field ground-based measurements recorded at a distance of approximately 5 km from the source were significantly more affected by light scattering at the surface of the volcanic cloud than were the far-field satellite observations, leading to a severe underestimation of the light absorbance caused by SO_2 in the cloud (Mori et al., 2006). This so-called light dilution effect was also reflected in the fact that the SO_2 column densities in the center of the volcanic plume (Table S3) were lower during the ash emission period than they were prior to the eruption.

4.5.2 Limitations of the used methods

Locating seismic events with a reliable accuracy largely depends on the density of the seismic network and the spatial distribution of the stations. Throughout October 2015 and thus during the eruption, only one seismic station was operational (QUE; see Fig. 4.1). Hence, a limitation during the analysis of the seismic data was that we could neither constrain the locations of the VT and tremor signals nor characterize the event sources due to a lack of data; moreover, because the events were characterized by a small magnitude, they were strongly affected by noise.

Satellite remote sensing has continuously developed in recent decades to include better sensor technology and higher-accuracy measurements, thereby showing that it is a very useful technique, especially for monitoring remote areas that are difficult to access. Nevertheless, the dependence of obtaining good-quality images and useful information from satellite images on the weather conditions still remains one of the main limitations of this approach, which we have also mentioned as an issue in our observations.

The main limitation of the methods used for computing the brightness and performing kymographic analysis is that they require good atmospheric conditions and a wind direction that favors the visibility of the plume within the image field of interest. In particular, pixel brightness analysis requires a permanently visible volcanic plume (preferentially under blue-sky conditions) to acquire clear and good-quality images. Nevertheless, although our method does not consider the influences of long-term atmospheric variables (e.g., pressure, humidity and temperature) governing the condensation of water vapor in a volcanic plume, the resulting

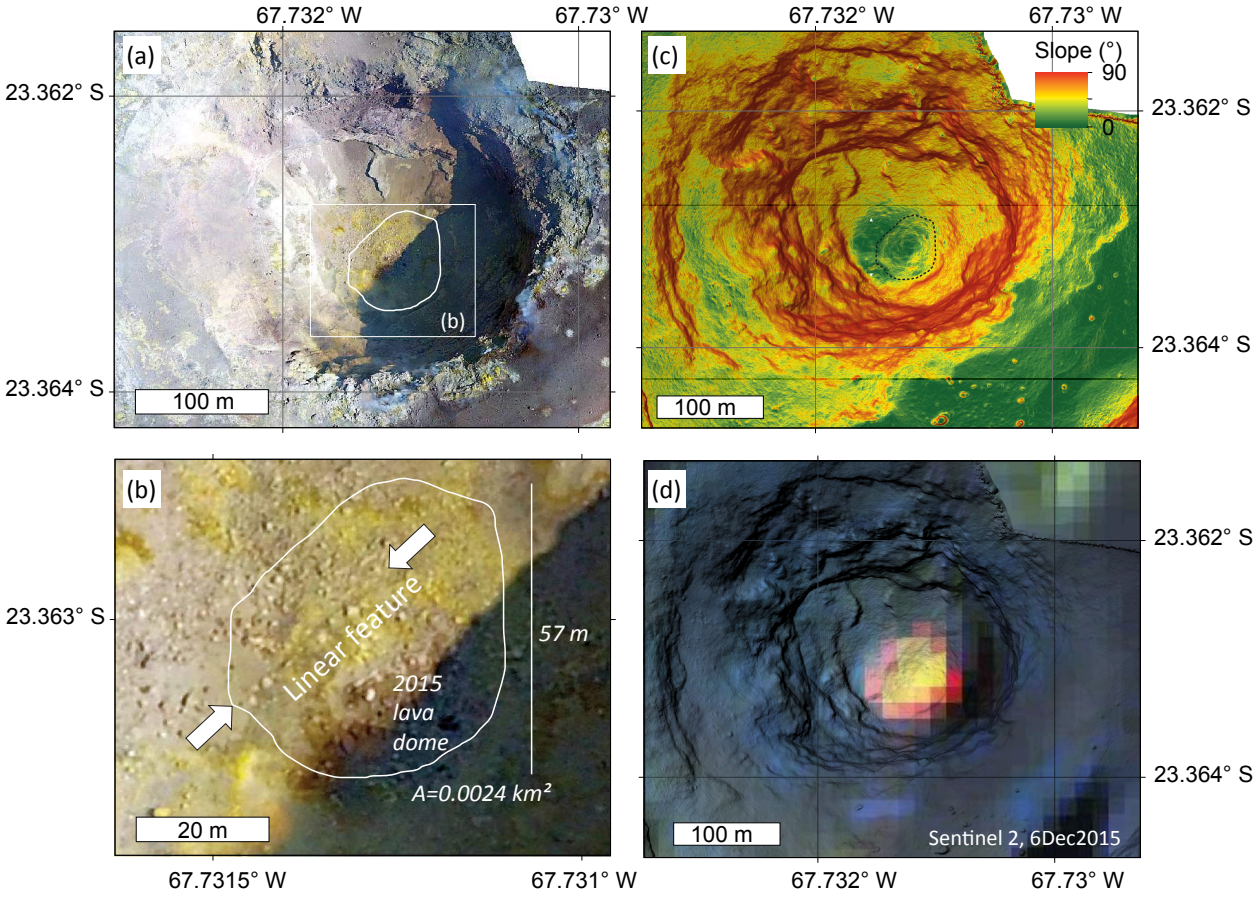

Figure 4.7: Drone overflight results. (a) Photomosaic of the crater region showing the 2017 central elevation of the crater floor with a diameter of 57 m. The white line is the approximate perimeter of the thermal anomaly. (b) Close-up of photomosaic (as indicated in a) showing the blocky central elevation of the crater floor which corresponds to the dimensions of the thermal anomaly. Note the NE-SW-striking linear feature transecting the central elevation. (c) Digital elevation shaded relief model overlaid by a slope map whose values represent the slope in degrees; the central elevation is delineated in the center of the crater. (d) Sentinel-2 thermal anomaly pixels acquired 37 days after the eruption overlain on a shaded relief map to illustrate the location of the central elevation of the deep Lascar crater. Data provided by the European Space Agency (ESA).

perturbations can be corrected as long as they are well defined. The sun's position and diurnal radiation variations additionally cause cyclic perturbations, which can be either avoided by comparing pictures taken at the same time of day or corrected by analyzing reference regions, as proposed by Girona et al. (2015). The use of this approach implies an advantage with respect to other established gas monitoring methods considering its low cost and its straightforward and valuable implementation for detecting changes in a volcanic plume.

SO_2 flux measurements from the mini-DOAS scanner could be conducted only during daylight, when the UV intensity is sufficiently high, and, therefore, as they contain gaps at nighttime, these records are semicontinuous. The measurements at Lascar were further restricted by the fact that only one scanning mini-DOAS station was installed 6.75 km away, with a target on the northern face of the crater, thus limiting the observation range to a northerly direction of plume transport that was confined between WNW and ENE. Thus, we were fortunate that the eruption plume drifted through the field of view of that one station, enabling us to conduct this detailed study of its optical properties. Volcanic plumes that drifted in directions outside this range were not captured by the instrument, causing additional discontinuities in the gas emission time series. Moreover, such measurements are strongly affected if considerable amounts of ash are present in the volcanic plume, leading to a severe underestimation of the emitted gas mass, as discussed above. Likewise, the passage of meteorological clouds during

the precipitation period likely introduced larger uncertainty into our observations due to the scattering of light on the water droplets in the cloud, leading to either an underestimation or an overestimation, depending on the locations of those meteorological clouds with respect to the volcanic plume (Kern et al., 2010). Stormy conditions, which were frequently encountered throughout the entire observation period, caused a strong dilution of the gas plume already located in the near-field region of the volcano, which resulted in a reduction in the already very low SO_2 SCDs, often hindering the detection of the gas plume. Altogether, these frequently occurring unfavorable weather conditions led to a variable data quality, resulting in standard errors ranging between ±30 % and ±50 %.

On the Andean Plateau, storms and poor weather conditions in general are more often characterized by snowfall than by rainfall or hail, as was observed by the cameras during the three precipitation events that occurred during the study period. However, visual distinction between the types of precipitation (snow, hail and rain) in such field conditions is challenging. Moreover, some precipitation events may have an effect on the volcano, while others do not, since strong winds and dry atmospheric conditions commonly rather promote sublimation of snow and hail instead of melting and thus prevent water from percolating into the volcano, besides other complexities. Therefore, the values registered by our instrument may be an underestimation of the real amount of accumulated precipitation but also do not necessarily reflect changes in soil moisture and water penetration. To understand the occurrence of phreatic eruptions in the Andean Plateau, future monitoring networks should include hydrometeor and soil moisture stations capable of distinguishing between types of precipitation and determining the depth of water penetration.

High-quality and accurate *in-situ* gas and temperature measurements depend on the appropriate placement of the instruments as a consequence of the accessibility of those locations. To this end, measurements of the CO_2 variability at Lascar could be carried out only at the fumarole field on the rim of the crater, where magmatic gas emissions are altered following mixing with hydrothermal fluids. Moreover, observations from the crater rim may not be representative of the gas discharge conditions elsewhere throughout the volcano, particularly when the focus of gas emission changes. The gas emissions during the eruption, for example, were strongly focused in the crater area, suggesting that the marginal areas at higher elevations (e.g., our fumarole on the crater rim) were less well supplied with gas because the overpressure was released elsewhere. The co-eruptive CO_2 minimum was thus likely a consequence of the location of the CO_2 sensor, which is one major limitation of using point-sampling devices. Furthermore, the CO_2 mixing ratio and temperature of a fumarole are also strongly susceptible to changes in the weather, which is why the interpretation of these variables is often complicated when observed trends cannot be explicitly attributed to weather conditions or volcanic activity. Monitored together with relevant weather variables, however, measurements of the CO_2 mixing ratio and temperature in hydrothermally dominated fumaroles are extremely well suited for studying the influence of weather conditions on volcanic activity. This was particularly true for the hydrothermally dominated low-temperature fumarole on the crater rim studied in this work.

Finally, using drones provides the possibility of attaching equipment to measure different parameters (e.g., thermal anomalies, gas emissions and structural features) during an overflight. However, the successful use of drones is usually limited by complicated access to the remote areas where volcanoes are located. Specifically, Lascar's summit is located at an elevation of almost 6 km a.s.l., and thus climbing to the rim requires a preceding acclimatization phase due to the thin-air conditions. Furthermore, overflights are commonly affected by strong winds, which are very common at such high altitudes, raising the risk that a drone will crash or directly preventing a drone from being launched. This was the main reason for the 2-year delay

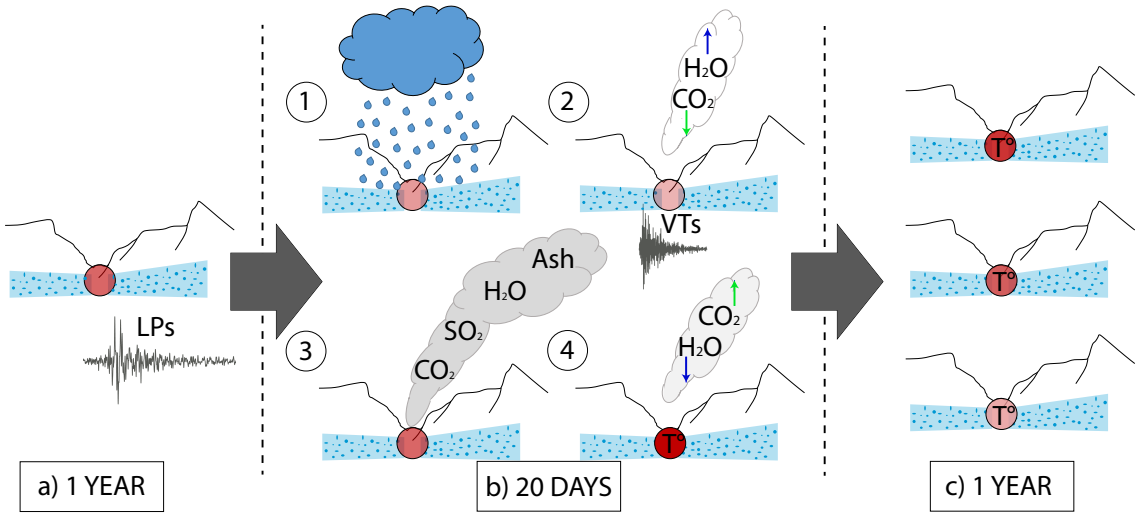

Figure 4.8: Schematic interpretation of the pre-, co- and post-eruptive processes associated with the 30 October 2015 phreatic eruption of Lascar volcano. The light-blue zones represent the approximate location of the hydrothermal system of Lascar. (a) The pre-eruptive phase started approximately 1 year before the eruption, showing a sustained increase in LP activity. (b) Ten days before the eruption, a 20 days phase initiated after being triggered by precipitation on 20 October. This phase developed in four stages: (1) an unusually strong precipitation event occurs; (2) meteoric water percolates into the crater, changes the water content and CO_2 concentration in the fumarole, and reactivates VT activity; (3) the volcano is pushed into a steam-driven explosion, producing a 1.7 km high eruption column above the crater that is composed mainly of water, ash, CO_2 and SO_2, causing the crater floor to fracture; (4) post-eruptive degassing transpires with a hotter fumarole containing more CO_2 and less water, and a thermal anomaly is present in the active crater; and (c) the post-eruptive permanent thermal anomaly slowly decreases in temperature for 1 year.

in our data and why some changes in the crater floor associated with the eruption may have remained undetected.

4.5.3 Implication for future monitoring instrumentation

Seismic activity often increases before an eruption; hence, it is an essential tool for monitoring volcanic eruptions (Tokarev, 1963). Nevertheless, predicting spontaneous explosive activity remains a challenge either because dense instrumentation is unavailable or because certain eruption types, particularly steam-driven explosions, are not preceded by seismicity, although a few examples suggest that precursors may also exist for this eruption type. A good example is the Aso volcano, where a steam-driven explosion was preceded a few minutes earlier by a LP displacement signal due to the inflation and deflation of the source, which could provide warning for such eruptions based on broadband seismometer measurements (Kawakatsu et al., 2000).

From this perspective, the apparent absence of short-term precursors for the historical activity reported at Lascar could be a consequence of the deployed network. Comparing the observations derived from the complete image data set covering the 2015 eruption, we were able to find evidence of long-term variations in LP seismicity starting with an 8-month increase followed by a 4-month decrease that was accompanied by a constant drop in the thermal anomaly observed in August 2015. Likewise, shorter-term changes were also observed by camera, followed by the occurrence of new VT events, the frequency rate of which increased only a few minutes before the explosion. Overall, these observations allow us to infer a weak preparatory phase preceding the eruption.

Finally, most of the methods discussed in this study have been broadly and successfully used

to monitor volcanoes; for instance, drones have been employed to map morphological structures (e.g., Darmawan et al., 2018a), mini-DOAS scanners have been used to measure SO_2 emission rates (e.g., Bredemeyer et al., 2018), satellite data have been utilized to detect thermal anomalies (e.g., González et al., 2015), and *in-situ* sensors have been used to record gas concentrations and fumarole temperatures (e.g., Zimmer et al., 2017). In addition, the use of optical images from permanently installed cameras in this study was shown to be an effective way to detect pre-eruptive changes through pixel brightness analysis and to estimate the variations in and the altitude of the eruptive plume using kymographic analysis. Furthermore, the use of drones equipped with different sensors, such as high-resolution optical systems, captured detailed information about changes deep in the crater.

4.5.4 Conceptual model of the 2015 Lascar phreatic explosion

Our interpretation inferred from the parametric relationship between the CO_2 concentration and residual temperature of the fumarole after the percolation of meteoric water into the hydrothermal system is illustrated in Fig. 4.6. Here, we speculate about the cyclic evolution of the CO_2 mixing ratio and residual temperature of the summit fumarole 2 weeks after precipitation event P3. The cycle started with a reduction in the residual temperature of 4 °C during the period of 19-30 October 2015 and minor variations in the CO_2 content. During the 3 days following the eruption, the CO_2 mixing ratio changed from 4240 ppmv to 4380 ppmv, and a moderate increase in the residual temperature occurred. During 4-7 November 2015, the residual temperature increased further, whereas the CO_2 concentration decreased and slowly returned to the 'normal' pre-precipitation values (~4260 ppmv CO_2 and 0 °C residual temperature). Figure 4.6 clearly shows the effects of meteoric water on the evolution of the CO_2 concentration and the fluctuations in the fumarole temperature. This result is in agreement with observations of Tassi et al. (2009) regarding the significant influence of meteoric inputs in the southern-outer rim fumaroles. In addition, the 3 days delay in the increase in the pixel brightness seems to be the required time for water to infiltrate into the hydrothermal system and to vaporize.

The apparent anticorrelated behavior of the steam brightness and CO_2 concentration (Fig. S2) may suggest that an increase in the water vapor within the plume is directly associated with a lower CO_2 concentration at fumaroles. The observed difference between the observed behavior of the SO_2 flux and the CO_2 concentrations, however, can also be associated with distinct instrument observation ranges. While SO_2 fluxes were measured globally from the entire volcano and were largely dominated by gas contributions from the plume emitted mainly from the active crater, the CO_2 concentration was measured locally at a fumarole located in the crater periphery. The scrubbing of SO_2 emissions is thus less likely to occur at Lascar because the gases emitted by the active crater do not have to pass through the aquifers of the surrounding hydrothermal system (Bredemeyer et al., 2018), whereas the CO_2 concentrations on the crater rim may indeed have been affected by water that had infiltrated into the volcanic edifice. In the long term, both parameters (i.e., the SO_2 and CO_2 concentrations) did not display significant variations that deviated from the normal previously observed behavior.

The previous interpretation and the processes preceding the eruption are conceptualized in Fig. 4.8. Our conceptual model shows a pre-eruptive phase (Fig. 4.8a) characterized by a sustained increase in LP seismic activity. We interpret this phase as a sign of sustained fluid injection from depth inducing a long-lasting gradual pressure buildup due to a progressively blocked fluid path. This interpretation is derived from the decrease in LP events and the reduction of the apparent thermal anomaly evidenced in the images acquired by Sentinel-2 months prior to the eruption. The co-eruptive phase spanning 20 days started with precipitation event P3 on 19-20 October, which caused the subsequent percolation of water into the volcanic

system (Fig. 4.8b-1), which in turn reduced the temperature of the fumarole and eventually prevented efficient outgassing, as is evidenced by the slight reduction in the CO_2 concentration (Fig. 4.8b-2). This water was vaporized and released into the atmosphere, increasing the water content of the volcanic plume. The eruption (Fig. 4.8b-3) principally released water, CO_2 and SO_2, thereby expelling much of the excess water within the hydrothermal system. Over the following days, an increase in the temperature contributed to a further reduction in the water content in the plume, and the gradual drying of degassing pathways led to the observed increase in the CO_2 concentration (Fig. 4.8b-4). The post-eruptive phase (Fig. 4.8c) is distinguished by a permanent thermal anomaly that slowly decreased in temperature throughout the following year.

4.6 Conclusion

This paper covered the period of unrest associated with the eruption of Lascar volcano on 30 October 2015. We characterize a steam-driven explosion of Lascar and its precursor activity. Based on a multidisciplinary data set, we found that signs of unrest and precursor activity can manifest as spatiotemporal changes on a variety of scales among the measured parameters. In the presented case, long-term changes in LP seismic activity were observed before but not after the eruption, while gas and camera data revealed short-term variations in a time window spanning the eruption. In addition, long-term remote-sensing information allowed us to recognize a thermal anomaly after the eruption that helped to support our short-term observations.

Overall, the multiparametric analysis suggests that the period of unrest began with a 1-year rapid increase in LP seismicity. During a gradual decline in the rate of seismicity, an unusually strong precipitation event occurred that initiated changes in the magmatic-hydrothermal system. Events evolved in four stages over a time window of days as follows: (1) precipitation, (2) enhanced steam formation and VT activation, (3) eruption, and (4) a temporary increase in the CO_2 mixing ratio and fumarole temperature. Afterwards, the thermal anomaly in the crater slowly decreased in intensity over approximately 1 year following the eruption (see Fig. 4.8).

Our analysis has shown that, by combining different techniques and data sets, we can create an efficient monitoring system to perform a successful hazard assessment and establish an early-warning system for volcanoes that seem to show no clear precursor activity. In addition, we have demonstrated that signs of unrest and precursor activity can manifest as spatiotemporal changes in a variety of scales and that analysis of such signals should be promoted for future monitoring at Lascar and other volcanoes exhibiting similar behavior worldwide.

Chapter 5

Summary and outlook

This dissertation has provided an overview of different aspects concerning the emplacement and geometry of the plumbing systems at caldera-like environments as well as the role played by these peculiarities in the unrest process and volcanic eruption. I described the regions of complexities within the plumbing systems at caldera-like settings, promoted by a deviating effect on the dike trajectory and focused on understanding how this effect boosts volcanic activity in the hydrothermal system of an active volcano. Therefore, the three manuscripts included in this cumulative thesis tackle the issue of the topographic effects as they define of the configuration and precursor of volcanic activity.

Among different mechanisms involved in the dike emplacements and the establishment of plumbing systems, I focused on exploring the effect generated by the stress reorientation in the crust due to topographic lows, providing an insight of possible geometries expected to develop beneath caldera-like topographies. Thus, applying laboratory models I found that magma and/or fluid transport is strongly influenced by the mass distribution in the crust, evolving into a plumbing system that can span from deep to very shallow depths. This means that the lack of mass due to caldera-like topographies deviates the intrusions towards regions with major load and away from the topographic lows. I observed intrusions that evolved into two circumferential end-members, circumferential dike and cone sheet, as well as intermediate geometries, all controlled by the caldera-like size and margin.

Simultaneously with the modeling approach, I conducted annual field trips to monitor Lascar volcano, which indeed showed unrest and even erupted in 2015. Using the data collected in those field campaigns in an attempt to validate the modeling results, the location of the LP events occurring during a period of high seismic activity in Lascar volcano were obtained. Considering that Lascar has a crater architecture that depicts caldera characteristics on a small scale and, taking advantage of the availability of seismic data, the inner structure of Lascar was imaged through the location of LP events. The results were constrained implementing the cross-correlation differential times and showing that most LP activity is concentrated at a very shallow depth within the volcanic edifice. The epicentral locations are arranged in an elongated cluster and oriented similarly to the two volcanic edifices, with hypocentral locations within the first 2 km beneath the dormant western edifice, suggested to be Lascar's hydrothermal system. The deepest part is considered to be a semi-vertical conduit beneath the active crater and connected to the shallow region through a deviatory path hypothesized to be the result of continuous E-W movement of the old nested crater towards the active crater. This would induce the deepening of the active crater and in consequence, changes in the stress field of the surrounding rocks. The reorientation of the stress field would act directly on the shallow portion of the plumbing system in its developing phase, where the hydrothermal system is located, similar to the effect produced by the caldera-like topography in the laboratory models but at a smaller scale. This has implications in the degassing, crater morphology and eruptive activity of Lascar.

Herein, the active degassing at Lascar is produced by continuous feeding of magmatic gases that interact with the hydrothermal system. I found that the pre-eruptive activity of Lascar is principally conducted within the hydrothermal system, which can be influenced by the sustained subsidence of the active crater. The anomalous long-lasting LP activity during the pre-eruptive phase of the 2015 eruption is interpreted as the cause of the pressure built up in the volcanic system. According to our observations and previous studies, I associated one year anomalous seismicity evolution and the persisting inhibition of the thermal anomaly with the continuous deepening of the active crater. The continuous deepening would block the fluid path, increasing the pressure in the shallow hydrothermal system. Changes in the fumarole activity following the precipitation ten days before the eruption suggested percolation of the meteoric water to be the trigger of the eruption. Overall, the shallow depth of the hydrothermal system is considered to contribute to efficient water percolation, which is added to a system that was already exhibiting anomalous activity. However, we do not have a way to prove this hypothesis.

The analysis based on the studies elaborated in this dissertation shows the importance of combining observations with models to obtain a more effective interpretation of volcanic processes. Thus, this shows that volcanoes must be viewed as a system, where the arrangement of the plumbing system, the external structure, as well as environmental factors influence the volcanic activity and the eruptive style beyond purely chemical and physical magma properties. Moreover, this dissertation will contribute to an improved interpretation of geophysical data and understanding of volcanic processes to produce more accurate models and efficient forecasting of future eruptions at Lascar or volcanoes that show similar behavior.

Future work: In a first attempt, this thesis combines aspects concerning the plumbing systems in caldera-like settings, utilizing diverse methods. I empirically shown the implication of the unloading effect of caldera-like architecture on magma propagation and definition of the intrusion emplacement and geometry. These results highly impact on the understanding of natural systems worldwide because they can assist in the interpretation of deformation and seismic data, as well as improve the modeling of deformation sources since in previous studies they are commonly assumed as simplified flat geometric intrusions due to factors such as low amplitude of the signal deformation. Here, I have demonstrated that intrusions can adopt a broad range of geometries by exploring the emplacement mechanism due to the elastic properties of the crust. For this purpose, I used a reduced number of parameters but if we aim to produce more accurate results and reduce the model limitations, we need to implement them with higher complexities. Thus, future models could consider factors as inelastic deformation, rock layering and the magma-flow dynamics. Furthermore, models implementing the trace particle technique in 3D Digital Image Correlation (DIC) may allow one to obtain the displacement and strain, as well as the surface deformation by using a sensor to scan the surface of the models. This method can provide better-quantified results for stress and strain calculation. The result will be determined for different intrusion geometries and will be compared and used to interpret real geophysical data.

Studying the Lascar eruption opened new questions about likely cyclic eruption behavior. Since 1986, Lascar has shown an eruptive pattern of one eruption every second year on average, with phreatic eruption as the most frequent style. These eruptions are very hazardous and have caused many fatalities in the past years. For instance, the recent eruption in 2014 of Mt. Ontake killed 64 people (Oikawa et al., 2016), which is why my study makes an important contribution to forecasting and early warning development. In this thesis, I suggested the sustained deepening of the active crater as the cause of pressure building during the pre-eruptive phase at Lascar. If the deepening rate is constant, we would expect a cyclic pattern of eruptions, as apparent. Moreover, the similar temporal modulation observed in the average of

events preceding the 2013 and 2015 eruptions can confirm this hypothesis. Thus, the imminent occurrence of an eruption in the near future with similar changes in the tested parameters would prove this hypothesis. If this occurs as is my expectation, this will be a major contribution to the knowledge of the Lascar system and in general volcanoes worldwide, providing an advantage in early warning and eruption forecasting.

Supplementary information

This supplement contains video captions, figures and tables in support of articles included in Chapter 2 and Chapter 4.

Supplementary information for Chapter 2: Analog modeling on calderas

Video Figure S1: Experimental circumferential dike formation and propagation (all videos 30 frames per second): a)-b) Experiment AG-07 viewed with a) polarized light ($x-z$ plane), and b) artificial light ($y-z$ plane), c)-f) Experiment AG-13 ($x-z$ plane) viewed with laser light (c), and total strain (color maps: horizontal e_{xx} (d), vertical e_{zz} (e), and shear e_{xz} (f) components) and displacement (vector arrows) calculated using digital image correlation. The red color represents extensional deformation in the normal components and anticlockwise rotational in the shear component (video on the enclosed CD).

Video Figure S2: Experimental cone sheet formation and propagation (experiment AG-08, 30 frames per second): a) viewed with polarized light ($x-z$ plane), and b) viewed with artificial light ($y-z$ plane) (video on the enclosed CD).

Video Figure S3: Experimental cone sheet formation and propagation (experiment AG-17, $x-z$ plane, all videos 30 frames per second): a) Viewed with laser light, b)-d) total strain (color maps: horizontal e_{xx} (b), vertical e_{zz} (c), and shear e_{xz} (d) components) and displacement (vector arrows) calculated using digital image correlation. The red color represents extensional deformation in the normal components and anticlockwise rotational in the shear component (video on the enclosed CD).

Video Figure S4: Experimental cone sheet formation and propagation (experiment AG-19, $y-z$ plane, all videos 30 frames per second): a) Viewed with laser light, b)-d) total strain (horizontal e_{yy} (b), vertical e_{zz} (c), and shear e_{yz} (d) components) and displacement (vector arrows) calculated using digital image correlation. The red color represents extensional deformation in the normal components and anticlockwise rotational in the shear component (video on the enclosed CD).

Table S1: Parameters and equations implemented to scale the experiments, including their ranges and the preferred values we have selected in nature and the experiments.

	Parameter (units) or Equation	Nature (range)	Nature (preferred value)	Experiments	Experiments (preferred value)	Scaling ratio
Medium and fluid properties						
Host medium density[1]	$\rho_r (kgm^{-3})$	2300–3000	2700	994–1002	1200	0.37
Fluid density[2]	$\rho_f (kgm^{-3})$	2000–2800	2680	990–996	996	0.37
Fluid viscosity[10]	$\mu (Pas)$	0.1–1 $\times 10^{23}$	100	8.9×10^{-4}	8.9×10^{-4}	8.9×10^{-6}
Density difference[3]	$\Delta\rho = \rho_r - \rho_f$	1–300	20	4–6	6	0.3
Poisson's ratio[4]	ν	0.1–0.35	0.25	0.495–0.5	0.499	2
Fracture toughness[5]	$K_c (Pam^{1/2})$	3×10^8–1×10^9	1×10^9	24–80	80	8×10^{-8}
Acceleration due to gravity	$g (ms^{-2})$	—	10	—	10	1
Geometry						
Geometric length	$L(m)$	—	1×10^3	—	0.01	1×10^{-5}
Caldera diameter	$C(m)$	9×10^3–12×10^3	12×10^3	0.09–0.12	0.12	1×10^{-5}
Caldera depth	$D(m)$	3×10^3–4.5×10^3	4×10^3	0.03–0.045	0.04	1×10^{-5}
Depth of intrusion[11]	$h(m)$	3×10^3–17×10^3	13.5×10^3	0.08–0.16	0.15	1.1×10^{-5}
Scaling expression						
Lengths						
Buoyancy length[6]	$L_b = (K_c/(\pi^{1/2}\Delta\rho g))^{2/3}$	3.2×10^3–6.6×10^4	19965	0.83–1.22	0.83	4.1×10^{-5}
Stresses						
Elastic deformation[7]	$\sigma = Ee$	1×10^6–4×10^7	2×10^7	4.5–75	60	3×10^{-6}
Lithostatic load	$P_L = \rho_r gh$	6.7×10^7–5×10^8	3.6×10^8	779–1571	1473	4.1×10^{-6}
Unloading[8]	$P_U = \rho_r gD$	6.9×10^7–1.3×10^8	1.1×10^8	298–451	401	3.7×10^{-6}
Young's Modulus[9]	E	1×10^9–1×10^{10}	1×10^{10}	300–3000	3000	3×10^{-7}
Strain						
Thickness/width	e	1×10^{-3}–4×10^{-3}	2×10^{-3}	0.015–0.025	0.02	10

[a] See (Carmichael and Klein, 2018; Di Giuseppe et al., 2009, [1]), (Murase and McBirney, 1973, [2]), (Kavanagh et al., 2013; Rivalta et al., 2015, [3,5,6,8,9]), (Gercek, 2007, [4]), (Merle, 2015, [8]), (Rivalta et al., 2015, [10]), (Kennedy et al., 2018, [11]) for definitions and ranges.

Table S2: Properties of the two cylindrical brass loads used to measure the Young's modulus.

Load	Mass [kg], m	Thickness [m]	Diameter [m], Ψ
L1	0.05	0.012	0.025
L2	0.042	0.010	0.025

Supplementary information for Chapter 4: Phreatic eruption of Lascar volcano

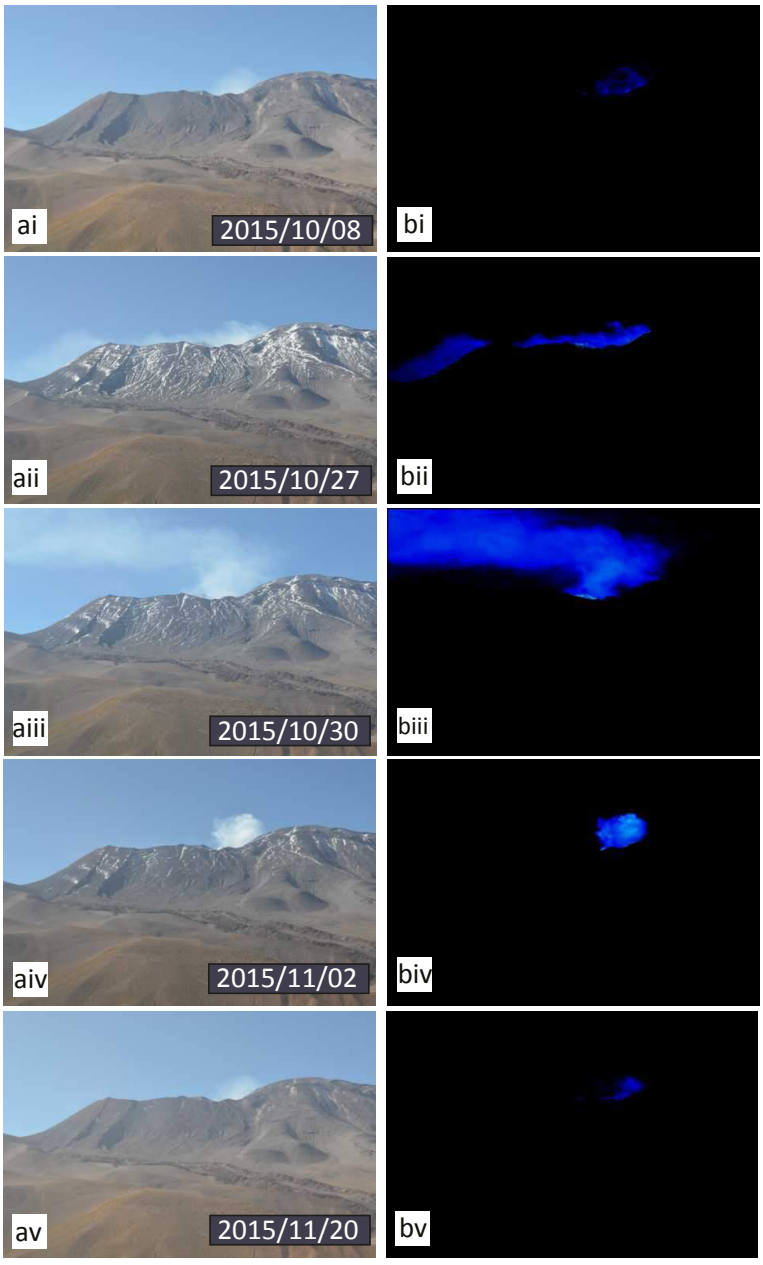

Figure S1: Example of images from camera C2 (see Fig. 4.1 for location) used for brightness analysis for the period 1st October to 30th November. Column (a) shows raw images and column (b) shows the same images after application of the mask filter. Image (aiii) shows the volcanic plume condition just after the VT cluster and 12 minutes before the eruption. All these images were made at 9:12 local time (12:12 UTC).

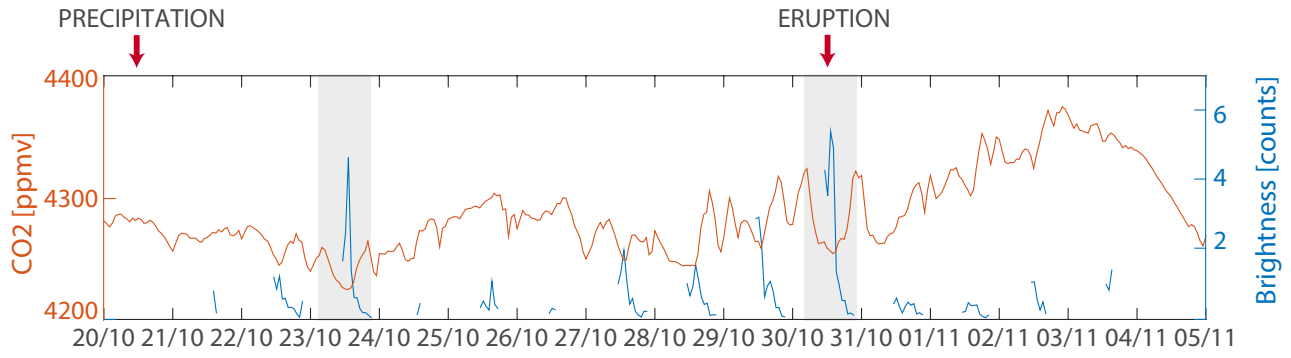

Figure S2: CO_2 mixing ratio versus hourly variations of fumarole brightness. The grey stripes show two pronounced peaks of brightness. The first one occurs three days after the precipitation (P3, see Fig. 4.2) and the second one during the eruption, showing clear anticorrelation between the parameters.

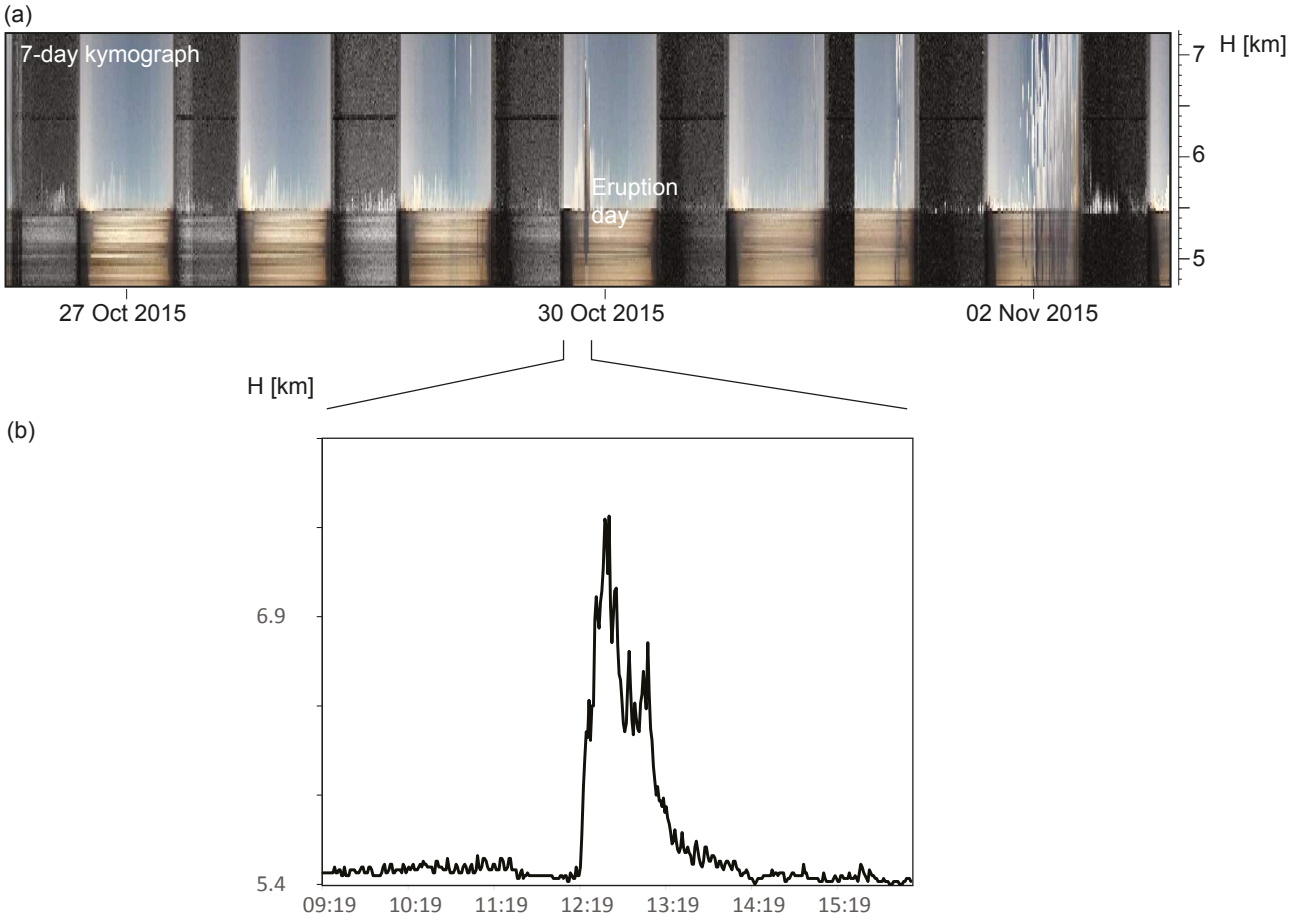

Figure S3: (a) One week kymograph showing the short eruption pulse. (b) Height variation of the eruption derived from the highest eruption point identified in the camera images along the vertical profile K-K' (see vertical line in Fig. 4.5b).

Table S3: Time series of plume center SO_2 SCDs of the October 30th, 2015 eruption along with corresponding SO_2-fluxes and plume transport conditions at approximately 5 km distance from crater, where the volcanic plume intercepts the field of view of the scanning DOAS. Exact UTC times of plume center intercept are indicated. The horizontal red line marks the time of eruption onset and bright yellow to orange cell fills provide amplitude information for each data column. Plume transport directions were determined by means of triangulation using the location of the center of SO_2 mass in combination with the plume heights retrieved from visual imagery (see Fig. S3b). Plume heights 5 km downwind of the crater were assumed to be about 100 m higher than those measured directly above source, since the plume was observed to continue rising slightly when being drifted downwind of the crater. Heights are given with respect to elevation of the crater rim. Wind speeds at plume height were obtained from GDAS1 atmospheric soundings provided by NOAA.

Time hh:mm:ss	SO_2 SCD [$ppmm$]	SO_2 SCD [molecules cm^{-2}]	SO_2-flux kg/s	Plume [degree]	Plume high [m] above crater	Wind speed at plume high [m/s]
11:50:50	249	6.23×10^{17}	4.11	76.9	200	10.2
12:03:05	203	5.08×10^{17}	9.75	40.5	200	7.8
12:16:32	646	1.62×10^{18}	13.54	87.1	1000	8.64
12:27:52	766	1.92×10^{18}	55.14	62.8	1800	11.57
12:37:57	610	1.53×10^{18}	54.44	72.9	2200	12.4
12:48:01	656	1.64×10^{18}	49.28	38.3	1500	11
12:57:33	425	1.06×10^{18}	40.33	33.3	1300	10.53
13:06:56	462	1.16×10^{18}	44.38	31.3	1500	10.53
13:16:36	435	1.09×10^{18}	25.19	8.9	600	9.9
13:25:07	440	1.10×10^{18}	19.19	10.8	500	9.9
13:33:56	520	1.30×10^{18}	16.96	12.5	400	9.9
13:42:51	382	9.55×10^{17}	13.31	9	400	9.6
13:51:54	199	4.98×10^{17}	8.15	8.6	300	7.8
14:00:13	126	3.15×10^{17}	6.7	5.6	300	7.8
14:08:28	134	3.35×10^{17}	3.61	5.6	300	7.8
14:16:44	66	1.64×10^{17}	3.18	3.7	200	7.8

Bibliography

Aguilera, F., Viramonte, J., Medina, E., Guzmán, K., Becchio, R., Delgado, H., and Arnosio, M. (2006). Recent eruptive activity from Lascar volcano (2006). In *11th Chilean Geological Congress, Universidad Católica del Norte, Antofagasta*, pages 393–396, Antofagasta.

Albino, F., Pinel, V., and Sigmundsson, F. (2010). Influence of surface load variations on eruption likelihood: Application to two Icelandic subglacial volcanoes, Grímsvötn and Katla. *Geophysical Journal International*, 181(3):1510–1524.

Anderson, E. (1936). The dynamics of the formation of cone-sheets, ring dykes, and caldron-subsidence. *Royal Society of Edinburgh Proceedings*, 56:128–163.

Asch, G., Kurt, W., Hellweg, M., Seidl, D., and Rademacher, H. (1996). Observations of rapid-fire event tremor at Lascar volcano, Chile. *Annals of Geophysics*, 39(2):273–282.

Bagnardi, M., Amelung, F., and Poland, M. P. (2013). A new model for the growth of basaltic shields based on deformation of Fernandina volcano, Galápagos Islands. *Earth and Planetary Science Letters*, 377-378:358–366.

Barberi, F., Bertagnini, A., Landi, P., and Principe, C. (1992). A review on phreatic eruptions and their precursors. *Journal of Volcanology and Geothermal Research*, 52(4):231–246.

Battaglia, J. and Aki, K. (2003). Location of seismic events and eruptive fissures on the Piton de la Fournaise volcano using seismic amplitudes. *Journal of Geophysical Research*, 108(B8):2364.

Battaglia, J., Got, J., and Okubo, P. (2003). Location of long-period events below Kilauea Volcano using seismic amplitudes and accurate relative relocation. *Journal of Geophysical Research*, 108(B12):2553.

Bean, C. J., De Barros, L., Lokmer, I., Métaxian, J.-P., O' Brien, G., and Murphy, S. (2014). Long-period seismicity in the shallow volcanic edifice formed from slow-rupture earthquakes. *Nature Geoscience*, 7(1):71–75.

Beyreuther, M., Barsch, R., Krischer, L., Megies, T., Behr, Y., and Wassermann, J. (2010). ObsPy: A Python Toolbox for Seismology. *Seismological Research Letters*, 81(3):530–533.

Blundy, J., Mavrogenes, J., Tattitch, B., Sparks, S., and Gilmer, A. (2015). Generation of porphyry copper deposits by gas-brine reaction in volcanic arcs. *Nature Geoscience*, 8(3):235–240.

Bohm, M., Lüth, S., Echtler, H., Asch, G., Bataille, K., Bruhn, C., Rietbrock, A., and Wigger, P. (2002). The Southern Andes between 36° and 40°S latitude: seismicity and average seismic velocities. *Tectonophysics*, 356(4):275–289.

Bonaccorso, A., Cannata, A., Corsaro, R. A., Di Grazia, G., Gambino, S., Greco, F., Miraglia, L., and Pistorio, A. (2011). Multidisciplinary investigation on a lava fountain preceding a flank eruption: The 10 May 2008 Etna case. *Geochemistry, Geophysics, Geosystems*, 12(7):1–21.

Bredemeyer, S. and Hansteen, T. H. (2014). Synchronous degassing patterns of the neighbouring volcanoes Llaima and Villarrica in south-central Chile: the influence of tidal forces. *International Journal of Earth Sciences*, 103(7):1999–2012.

Bredemeyer, S., Ulmer, F. G., Hansteen, T. H., and Walter, T. R. (2018). Radar path delay effects in volcanic gas plumes: The case of Láscar Volcano, Northern Chile. *Remote Sensing*, 10(10):1514.

Brook, M. and Moore, C. (1974). Lightning in volcanic clouds. *Journal of Geophysical Research*, 79(3):472–475.

Brown, D. (2012). Tracker Video Analysis and Modeling Tool for Physics Education.

Brown, D. J. and Bell, B. R. (2006). Intrusion-induced uplift and mass wasting of the Palaeogene volcanic landscape of Ardnamurchan, NW Scotland. *Journal of the Geological Society*, 163(1):29–36.

Browning, J. and Gudmundsson, A. (2015). Caldera faults capture and deflect inclined sheets: an alternative mechanism of ring dike formation. *Bulletin of Volcanology*, 77(1):4.

Buckingham, E. (1914). On Physically Similar Systems; Illustrations of the Use of Dimensional Equations. *Physical Review*, 4(4):345–376.

Burchardt, S. and Galland, O. (2016). Studying Volcanic Plumbing Systems – Multidisciplinary Approaches to a Multifaceted Problem. In *Updates in Volcanology - From Volcano Modelling to Volcano Geology*, pages 23–53. InTech.

Burchardt, S., Tanner, D. C., Troll, V. R., Krumbholz, M., and Gustafsson, L. E. (2011). Three-dimensional geometry of concentric intrusive sheet swarms in the Geitafell and the Dyrfjöll volcanoes, eastern Iceland. *Geochemistry, Geophysics, Geosystems*, 12(7).

Burchardt, S., Troll, V. R., Mathieu, L., Emeleus, H. C., and Donaldson, C. H. (2013). Ardnamurchan 3D cone-sheet architecture explained by a single elongate magma chamber. *Scientific Reports*, 3(1):2891.

Burchardt, S., Walter, T. R., and Tuffen, H. (2018). Growth of a Volcanic Edifice Through Plumbing System Processes–Volcanic Rift Zones, Magmatic Sheet-Intrusion Swarms and Long-Lived Conduits. In *Volcanic and Igneous Plumbing Systems*, pages 89–112. Elsevier.

Cannata, A., Hellweg, M., Di Grazia, G., Ford, S., Alparone, S., Gresta, S., Montalto, P., and Patanè, D. (2009). Long period and very long period events at Mt. Etna volcano: Characteristics, variability and causality, and implications for their sources. *Journal of Volcanology and Geothermal Research*, 187(3-4):227–249.

Caricchi, L. and Blundy, J. (2015). The temporal evolution of chemical and physical properties of magmatic systems. *Geological Society Special Publication*, 422(1):1–15.

Carmichael, R. S. and Klein, C. (2018). Rock. https://www.britannica.com/science/rock-geology. (Accessed 26 July 2018).

Carn, S. A., Watts, R. B., Thompson, G., and Norton, G. E. (2004). Anatomy of a lava dome collapse: The 20 March 2000 event at Soufrière Hills Volcano, Montserrat. *Journal of Volcanology and Geothermal Research*, 131(3-4):241–264.

Cauchie, L., Saccorotti, G., and Bean, C. J. (2015). Amplitude and recurrence time analysis of LP activity at Mount Etna, Italy. *Journal of Geophysical Research: Solid Earth*, 120(9):6474–6486.

Cesca, S., Battaglia, J., Dahm, T., Tessmer, E., Heimann, S., and Okubo, P. (2008). Effects of topography and crustal heterogeneities on the source estimation of LP event at Kilauea volcano. *Geophysical Journal International*, 172(3):1219–1236.

Cesca, S., Åđen, A. T., and Dahm, T. (2014). Seismicity monitoring by cluster analysis of moment tensors. *Geophysical Journal International*, 196(3):1813–1826.

Cesca, S. and Grigoli, F. (2015). Full Waveform Seismological Advances for Microseismic Monitoring. In *Advances in Geophysics*, volume 56, pages 169–228. Elsevier.

Cesca, S., Grigoli, F., Heimann, S., Dahm, T., Kriegerowski, M., Sobiesiak, M., Tassara, C., and Olcay, M. (2016). The M w 8.1 2014 Iquique, Chile, seismic sequence: a tale of foreshocks and aftershocks. *Geophysical Journal International*, 204(3):1766–1780.

Çetin, A. E., Dimitropoulos, K., Gouverneur, B., Grammalidis, N., Günay, O., HabiboÇğlu, Y. H., Töreyin, B. U., and Verstockt, S. (2013). Video fire detection – Review. *Digital Signal Processing*, 23(6):1827–1843.

Chadwick, W. W., Jónsson, S., Geist, D. J., Poland, M., Johnson, D. J., Batt, S., Harpp, K. S., and Ruiz, A. (2011). The May 2005 eruption of Fernandina volcano, Galápagos: The first circumferential dike intrusion observed by GPS and InSAR. *Bulletin of Volcanology*, 73(6):679–697.

Chouet, B. (1986). Dynamics of a fluid-driven crack in three dimensions by the finite difference method. *Journal of Geophysical Research*, 91(B14):13967.

Chouet, B. (1988). Resonance of a fluid-driven crack: radiation properties and implications for the source of long-period events and harmonic tremor. *Journal of Geophysical Research*, 93(B5):4375–4400.

Chouet, B. (2003). Volcano Seismology. *Pure and Applied Geophysics*, 160(3):739–788.

Chouet, B., Hamisevicz, N., and McGetchin, T. R. (1974). Photoballistics of volcanic jet activity at Stromboli, Italy. *Journal of Geophysical Research*, 79(32):4961–4976.

Chouet, B. A. (1996). Long-period volcano seismicity: its source and use in eruption forecasting. *Nature*, 380(6572):309–316.

Chouet, B. A. and Matoza, R. S. (2013). A multi-decadal view of seismic methods for detecting precursors of magma movement and eruption. *Journal of Volcanology and Geothermal Research*, 252:108–175.

Chouet, B. A., Page, R. A., Stephens, C. D., Lahr, J. C., and Power, J. A. (1994). Precursory swarms of long-period events at Redoubt Volcano (1989–1990), Alaska: Their origin and use as a forecasting tool. *Journal of Volcanology and Geothermal Research*, 62(1-4):95–135.

Christenson, B., Reyes, A., Young, R., Moebis, A., Sherburn, S., Cole-Baker, J., and Britten, K. (2010). Cyclic processes and factors leading to phreatic eruption events: Insights from the 25 September 2007 eruption through Ruapehu Crater Lake, New Zealand. *Journal of Volcanology and Geothermal Research*, 191(1-2):15–32.

Cole, J., Milner, D., and Spinks, K. (2005). Calderas and caldera structures: a review. *Earth-Science Reviews*, 69(1-2):1–26.

Comte, D., Roecker, S. W., and Suárez, G. (1994). Velocity structure in northern Chile: evidence of subducted oceanic crust in the Nazca Plate. *Geophysical Journal International*, 117(3):625–639.

Corbi, F., Rivalta, E., Pinel, V., Maccaferri, F., and Acocella, V. (2016). Understanding the link between circumferential dikes and eruptive fissures around calderas based on numerical and analog models. *Geophysical Research Letters*, 43(12):6212–6219.

Corbi, F., Rivalta, E., Pinel, V., Maccaferri, F., Bagnardi, M., and Acocella, V. (2015). How caldera collapse shapes the shallow emplacement and transfer of magma in active volcanoes. *Earth and Planetary Science Letters*, 431:287–293.

Crisp, J. D. C. (1953). The Use of Gelatin Models in Structural Analysis. *Proceedings of the Institution of Mechanical Engineers, Part B: Management and engineering manufacture*, 1(1-12):580–604.

Cusano, P., Petrosino, S., and Saccorotti, G. (2008). Hydrothermal origin for sustained Long-Period (LP) activity at Campi Flegrei Volcanic Complex, Italy. *Journal of Volcanology and Geothermal Research*, 177(4):1035–1044.

Darmawan, H., Walter, T. R., Brotopuspito, K. S., Subandriyo, and I Gusti Made Agung Nandaka (2018a). Morphological and structural changes at the Merapi lava dome monitored in 2012–15 using unmanned aerial vehicles (UAVs). *Journal of Volcanology and Geothermal Research*, 349:256–267.

Darmawan, H., Walter, T. R., Troll, V. R., and Budi-Santoso, A. (2018b). Structural weakening of the Merapi dome identified by drone photogrammetry after the 2010 eruption. *Natural Hazards and Earth System Sciences*, 18(12):3267–3281.

de Moor, J. M., Aiuppa, A., Pacheco, J., Avard, G., Kern, C., Liuzzo, M., Martínez, M., Giudice, G., and Fischer, T. P. (2016). Short-period volcanic gas precursors to phreatic eruptions: Insights from Poás Volcano, Costa Rica. *Earth and Planetary Science Letters*, 442:218–227.

de Silva, S. L. (1989). Altiplano-Puna volcanic complex of the central Andes. *Geology*, 17(12):1102.

de Zeeuw-van Dalfsen, E., Richter, N., González, G., and Walter, T. R. (2017). Geomorphology and structural development of the nested summit crater of Láscar Volcano studied with Terrestrial Laser Scanner data and analogue modelling. *Journal of Volcanology and Geothermal Research*, 329:1–12.

Del Pezzo, E., Bianco, F., and Borgna, I. (2013). Magnitude scale for LP events: a quantification scheme for volcanic quakes. *Geophysical Journal International*, 194(2):911–919.

Del Pezzo, E., Godano, C., Gorini, A., and Martini, M. (1992). Wave Polarization and Location of the Source of the Explosion Quakes at Stromboli Volcano. In *Volcanic Seismology*, number Chapter 21 in 3, pages 279–296. Springer, Berlin, Heidelberg.

Di Giuseppe, E., Funiciello, F., Corbi, F., Ranalli, G., and Mojoli, G. (2009). Gelatins as rock analogs: A systematic study of their rheological and physical properties. *Tectonophysics*, 473(3-4):391–403.

Di Grazia, G., Falsaperla, S., and Langer, H. (2006). Volcanic tremor location during the 2004 Mount Etna lava effusion. *Geophysical Research Letters*, 33(4):L04304.

Di Vito, M. A., Acocella, V., Aiello, G., Barra, D., Battaglia, M., Carandente, A., Del Gaudio, C., de Vita, S., Ricciardi, G. P., Ricco, C., Scandone, R., and Terrasi, F. (2016). Magma transfer at Campi Flegrei caldera (Italy) before the 1538 AD eruption. *Scientific Reports*, 6(1):32245.

Díaz, D., Brasse, H., and Ticona, F. (2012). Conductivity distribution beneath Lascar volcano (Northern Chile) and the Puna, inferred from magnetotelluric data. *Journal of Volcanology and Geothermal Research*, 217-218:21–29.

Dorbath, C., Gerbault, M., Carlier, G., and Guiraud, M. (2008). Double seismic zone of the Nazca plate in northern Chile: High-resolution velocity structure, petrological implications, and thermomechanical modeling. *Geochemistry, Geophysics, Geosystems*, 9(7).

Dzurisin, D. (2007). *Volcano Deformation – Geodetic Monitoring Techniques*. Springer, Springer-Praxis Books in Geophysical Sciences, Berlin.

Elsworth, D., Voight, B., Thompson, G., and Young, S. (2004). Thermal-hydrologic mechanism for rainfall-triggered collapse of lava domes. *Geology*, 32(11):969.

Fleet, D. and Weiss, Y. (2010). Optical Flow Estimation. In Paragios, N., , Chen, Y., , and Faugeras, O., editors, *Handbook of Mathematical Models in Computer Vision*, volume 19, pages 237–257. Springer-Verlag, New York.

Francis, P. W. and Rothery, D. A. (1987). Using the Landsat Thematic Mapper to detect and monitor active volcanoes: An example from Lascar volcano, northern Chile. *Geology*, 15(7):614–617.

Gaete, A., Cesca, S., Franco, L., San Martin, J., Cartes, C., and Walter, T. R. (2019a). Seismic activity during the 2013–2015 intereruptive phase at Lascar volcano, Chile. *Geophysical Journal International*, 219(1):449–463.

Gaete, A., Kavanagh, J. L., Rivalta, E., Hilmi Hazim, S., Walter, T. R., and Dennis, D. J. (2019b). The impact of unloading stresses on post-caldera magma intrusions. *Earth and Planetary Science Letters*, 508:109–121.

Galland, O., Bertelsen, H., Eide, C., Guldstrand, F., Haug, Ø., Leanza, H. A., Mair, K., Palma, O., Planke, S., Rabbel, O., Rogers, B., Schmiedel, T., Souche, A., and Spacapan, J. (2018). Storage and Transport of Magma in the Layered Crust–Formation of Sills and Related Flat-Lying Intrusions. In Burchardt, S., editor, *Volcanic and Igneous Plumbing Systems*, pages 113–138. Elsevier.

Galland, O., Burchardt, S., Hallot, E., Mourgues, R., and Bulois, C. (2014). Dynamics of dikes versus cone sheets in volcanic systems. *Journal of Geophysical Research: Solid Earth*, 119(8):6178–6192.

Galland, O., Holohan, E., Van Wyk De Vries, B., and Burchardt, S. (2015). Laboratory Modelling of Volcano Plumbing Systems: A Review. *Advances in Volcanology*, pages 1–14.

Galle, B., Johansson, M., Rivera, C., Zhang, Y., Kihlman, M., Kern, C., Lehmann, T., Platt, U., Arellano, S., and Hidalgo, S. (2010). Network for Observation of Volcanic and Atmospheric Change (NOVAC) - A global network for volcanic gas monitoring: Network layout and instrument description. *Journal of Geophysical Research Atmospheres*, 115(D5):D05304.

Gardeweg, M., Amigo, A., Matthews, S., Sparks, R., and Clavero, J. (2011). Geología del volcán Láscar, Región de Antofagasta. *Carta Geológica de Chile, Serie Geología Básica 131, p. 43, 1 mapa escala 1:50.000*.

Gardeweg, M., Sparks, R., and Matthews, S. J. (1998). Evolution of Lascar Volcano, Northern Chile. *Journal of the Geological Society*, 155(1):89–104.

GEOFON Data Centre (1993). GEOFON Seismic Network. Deutsches GeoForschungsZentrum GFZ. https://geofon.gfz-potsdam.de/.

Gercek, H. (2007). Poisson's ratio values for rocks. *International Journal of Rock Mechanics and Mining Sciences*, 44(1):1–13.

Geshi, N. (2005). Structural development of dike swarms controlled by the change of magma supply rate: the cone sheets and parallel dike swarms of the Miocene Otoge igneous complex, Central Japan. *Journal of Volcanology and Geothermal Research*, 141(3-4):267–281.

Gharti, H. N., Oye, V., Roth, M., and Kühn, D. (2010). Automated microearthquake location using envelope stacking and robust global optimization. *Geophysics*, 75(4):MA27–MA46.

Girona, T., Costa, F., Taisne, B., Aggangan, B., and Ildefonso, S. (2015). Fractal degassing from Erebus and Mayon volcanoes revealed by a new method to monitor H2O emission cycles. *Journal of Geophysical Research : Solid Earth*, 120:2988–3002.

Global Volcanism Program (1994). Report on Lascar (Chile). Bulletin of the Global Volcanism Network 19, Smithsonian Institution.

Global Volcanism Program (2013). Lascar (355100) in Volcanoes of the World. Technical Report v. 4.8.5, Smithsonian Institution.

Global Volcanism Program (2016). Report on Lascar (Chile). Bulletin of the Global Volcanism Network 41, Smithsonian Institution.

González, C., Inostroza, M., Aguilera, F., González, R., Viramonte, J., and Menzies, A. (2015). Heat and mass flux measurements using Landsat images from the 2000–2004 period, Lascar volcano, northern Chile. *Journal of Volcanology and Geothermal Research*, 301:277–292.

González, D. M., Bataille, K., Eulenfeld, T., and Franco, L. E. (2016). Temporal seismic wave velocity variations at Láscar volcano. *Andean Geology*, 43(2):240–246.

González-Ferrán, O. (1995). *Volcanes de Chile*. Instituto Geografico Militar, Santiago, Chile.

Gressier, J.-B., Mourgues, R., Bodet, L., Matthieu, J.-Y., Galland, O., and Cobbold, P. (2010). Control of pore fluid pressure on depth of emplacement of magmatic sills: An experimental approach. *Tectonophysics*, 489(1-4):1–13.

Grigoli, F., Cesca, S., Amoroso, O., Emolo, A., Zollo, A., and Dahm, T. (2014). Automated seismic event location by waveform coherence analysis. *Geophysical Journal International*, 196(3):1742–1753.

Grigoli, F., Cesca, S., Vassallo, M., and Dahm, T. (2013). Automated Seismic Event Location by Travel-Time Stacking: An Application to Mining Induced Seismicity. *Seismological Research Letters*, 84(4):666–677.

Gudmundsson, A. (2006). How local stresses control magma-chamber ruptures, dyke injections, and eruptions in composite volcanoes. *Earth-Science Reviews*, 79(1-2):1–31.

Guldstrand, F., Burchardt, S., Hallot, E., and Galland, O. (2017). Dynamics of Surface Deformation Induced by Dikes and Cone Sheets in a Cohesive Coulomb Brittle Crust. *Journal of Geophysical Research: Solid Earth*, 122(10):8511–8524.

Healey, G., Slater, D., Lin, T., Drda, B., and Goedeke, A. D. (1993). A system for real-time fire detection. *Proceedings of IEEE Conference on Computer Vision and Pattern Recognition*, 93:15–17.

Heap, M. J., Troll, V. R., Kushnir, A. R., Gilg, H. A., Collinson, A. S., Deegan, F. M., Darmawan, H., Seraphine, N., Neuberg, J., and Walter, T. R. (2019). Hydrothermal alteration of andesitic lava domes can lead to explosive volcanic behaviour. *Nature communications*, 10(1):5063.

Hellweg, M. (2000). Physical models for the source of Lascar's harmonic tremor. *Journal of Volcanology and Geothermal Research*, 101(1-2):183–198.

Hicks, P. D., Matthews, A. J., and Cooker, M. J. (2010). Triggering of a volcanic dome collapse by rainwater infiltration. *Journal of Geophysical Research: Solid Earth*, 115(9):1–8.

Jellinek, A. M. and DePaolo, D. J. (2003). A model for the origin of large silicic magma chambers: precursors of caldera-forming eruptions. *Bulletin of Volcanology*, 65(5):363–381.

Johnson, S. E., Paterson, S. R., and Tate, M. C. (1999). Structure and emplacement history of a multiple-center, cone-sheet-bearing ring complex: The Zarza Intrusive Complex, Baja California, Mexico. *Geological Society of America Bulletin*, 111(4):607–619.

Jolly, A. D., Sherburn, S., Jousset, P., and Kilgour, G. (2010). Eruption source processes derived from seismic and acoustic observations of the 25 September 2007 Ruapehu eruption-North Island, New Zealand. *Journal of Volcanology and Geothermal Research*, 191(1-2):33–45.

Jordan, T., Isacks, B., Allmendinger, R., Brewer, J., Ramos, V., and Ando, C. (1983). Andean tectonics related to geometry of subducted Nazca plate. *Geological Society of America Bulletin*, 94(3):341.

Jurkevics, A. (1988). Polarization analysis of three-component array data. *Bulletin of the Seismological Society of America*, 78(5):1725–1743.

Kao, H. and Shan, S.-J. (2004). The Source-Scanning Algorithm: mapping the distribution of seismic sources in time and space. *Geophysical Journal International*, 157(2):589–594.

Kao, H. and Shan, S. J. (2007). Rapid identification of earthquake rupture plane using Source-Scanning Algorithm. *Geophysical Journal International*, 168(3):1011–1020.

Kato, A., Terakawa, T., Yamanaka, Y., Maeda, Y., Horikawa, S., Matsuhiro, K., and Okuda, T. (2015). Preparatory and precursory processes leading up to the 2014 phreatic eruption of Mount Ontake, Japan. *Earth, Planets and Space*, 67(1):111.

Kavanagh, J., Boutelier, D., and Cruden, A. (2015). The mechanics of sill inception, propagation and growth: Experimental evidence for rapid reduction in magmatic overpressure. *Earth and Planetary Science Letters*, 421:117–128.

Kavanagh, J. L. (2018). Mechanisms of Magma Transport in the Upper Crust-Dyking. In *Volcanic and Igneous Plumbing Systems*, pages 55–88. Elsevier.

Kavanagh, J. L., Burns, A. J., Hilmi Hazim, S., Wood, E. P., Martin, S. A., Hignett, S., and Dennis, D. J. (2018a). Challenging dyke ascent models using novel laboratory experiments: Implications for reinterpreting evidence of magma ascent and volcanism. *Journal of Volcanology and Geothermal Research*, 354:87–101.

Kavanagh, J. L., Engwell, S. L., and Martin, S. A. (2018b). A review of laboratory and numerical modelling in volcanology. *Solid Earth*, 9(2):531–571.

Kavanagh, J. L., Menand, T., and Daniels, K. A. (2013). Gelatine as a crustal analogue: Determining elastic properties for modelling magmatic intrusions. *Tectonophysics*, 582:101–111.

Kavanagh, J. L., Menand, T., and Sparks, R. S. J. (2006). An experimental investigation of sill formation and propagation in layered elastic media. *Earth and Planetary Science Letters*, 245(3-4):799–813.

Kawakatsu, H., Kaneshima, S., Matsubayashi, H., Ohminato, T., Sudo, Y., Tsutsui, T., Uhira, K., Yamasato, H., Ito, H., and Legrand, D. (2000). Aso94: Aso seismic observation with broadband instruments. *Journal of Volcanology and Geothermal Research*, 101(1-2):129–154.

Kawakatsu, H. and Yamamoto, M. (2015). Volcano Seismology. In *Treatise on Geophysics*, volume 4, pages 389–419. Elsevier.

Kay, S. M. and Coira, B. L. (2009). Shallowing and steepening subduction zones, continental lithospheric loss, magmatism, and crustal flow under the Central Andean Altiplano-Puna Plateau. In *Backbone of the Americas: Shallow Subduction, Plateau Uplift, and Ridge and Terrane Collision*, volume 204, pages 229–259. Geological Society of America.

Kennedy, B., Holohan, E., Stix, J., Gravley, D., Davidson, J., and Cole, J. (2018). Magma plumbing beneath collapse caldera volcanic systems. *Earth-Science Reviews*, 177:404–424.

Kern, C., Deutschmann, T., Vogel, L., Wöhrbach, M., Wagner, T., and Platt, U. (2010). Radiative transfer corrections for accurate spectroscopic measurements of volcanic gas emissions. *Bulletin of Volcanology*, 72(2):233–247.

Kervyn, M., Ernst, G. G. J., van Wyk de Vries, B., Mathieu, L., and Jacobs, P. (2009). Volcano load control on dyke propagation and vent distribution: Insights from analogue modeling. *Journal of Geophysical Research*, 114(B3):B03401.

Kumagai, H., Placios, P., Ruiz, M., Yepes, H., and Kozono, T. (2011). Ascending seismic source during an explosive eruption at Tungurahua volcano, Ecuador. *Geophysical Research Letters*, 38(1):L01306.

Lahr, J. C., Chouet, B. A., Stephens, C. D., Power, J. A., and Page, R. A. (1994). Earthquake classification, location, and error analysis in a volcanic environment: implications for the magmatic system of the 1989-1990 eruptions at redoubt volcano, Alaska. *Journal of Volcanology and Geothermal Research*, 62(1-4):137–151.

Latter, J. (1981). Volcanic earthquakes, and their relationship to eruptions at Ruapehu and Ngauruhoe volcanoes. *Journal of Volcanology and Geothermal Research*, 9(4):293–309.

Le Bas, M. J. (1987). Nephelinites and carbonatites. *Geological Society, London, Special Publications*, 30(1):53–83.

Le Guern, F., Tazieff, H., and Pierret, R. F. (1982). An example of health hazard: People killed by gas during a phreatic eruption: Diëng plateau (Java, Indonesia), February 20th 1979. *Bulletin Volcanologique*, 45(2):153–156.

Lee, W. and Lahr, J. (1972). HYPO71 : a computer program for determining hypocenter, magnitude, and first motion pattern of local earthquakes. Technical report, U.S. Geological Survey.

Lokmer, I., Saccorotti, G., Di Lieto, B., and Bean, C. J. (2008). Temporal evolution of long-period seismicity at Etna Volcano, Italy, and its relationships with the 2004–2005 eruption. *Earth and Planetary Science Letters*, 266(1-2):205–220.

Maccaferri, F., Bonafede, M., and Rivalta, E. (2011). A quantitative study of the mechanisms governing dike propagation, dike arrest and sill formation. *Journal of Volcanology and Geothermal Research*, 208(1-2):39–50.

Magee, C., Stevenson, C., O'Driscoll, B., Schofield, N., and McDermott, K. (2012). An alternative emplacement model for the classic Ardnamurchan cone sheet swarm, NW Scotland, involving lateral magma supply via regional dykes. *Journal of Structural Geology*, 43:73–91.

Marchetti, E. and Ripepe, M. (2005). Stability of the seismic source during effusive and explosive activity at Stromboli Volcano. *Geophysical Research Letters*, 32(3):L03307.

Martinelli, B. (1990). Analysis of seismic patterns observed at Nevado del Ruiz volcano, Colombia during August - September 1985. *Journal of Volcanology and Geothermal Research*, 41(1-4):297–314.

Mason, B. G., Pyle, D. M., Dade, W. B., and Jupp, T. (2004). Seasonality of volcanic eruptions. *Journal of Geophysical Research: Solid Earth*, 109:B04206.

Mastin, L. G. (1995). Thermodynamics of gas and steam-blast eruptions. *Bulletin of Volcanology*, 57(2):85–98.

Mathieu, L., Burchardt, S., Troll, V. R., Krumbholz, M., and Delcamp, A. (2015). Geological constraints on the dynamic emplacement of cone-sheets - The Ardnamurchan cone-sheet swarm, NW Scotland. *Journal of Structural Geology*, 80(June):133–141.

Matoza, R. S., Shearer, P. M., Lin, G., Wolfe, C. J., and Okubo, P. G. (2013). Systematic relocation of seismicity on Hawaii Island from 1992 to 2009 using waveform cross correlation and cluster analysis. *Journal of Geophysical Research: Solid Earth*, 118(5):2275–2288.

Matoza, R. S., Shearer, P. M., and Okubo, P. G. (2014). High-precision relocation of long-period events beneath the summit region of Kilauea Volcano, Hawai'i, from 1986 to 2009. *Geophysical Research Letters*, 41(10):3413–3421.

Matthews, A. J. and Barclay, J. (2004). A thermodynamical model for rainfall-triggered volcanic dome collapse. *Geophysical Research Letters*, 31(L05614):1–4.

Matthews, A. J., Barclay, J., Carn, S., Thompson, G., Alexander, J., Herd, R., and Williams, C. (2002). Rainfall-induced volcanic activity on Montserrat. *Geophysical Research Letters*, 29(13):1644.

Matthews, S. J., Gardeweg, M. C., and Sparks, R. S. J. (1997). The 1984 to 1996 cyclic activity of Lascar Volcano, northern Chile: Cycles of dome growth, dome subsidence, degassing and explosive eruptions. *Bulletin of Volcanology*, 59(1):72–82.

McLeod, P. and Tait, S. (1999). The growth of dykes from magma chambers. *Journal of Volcanology and Geothermal Research*, 92(3-4):231–246.

McNutt, S. R. (2005). Volcanic Seismology. *Annual Review of Earth and Planetary Sciences*, 33(1):461–491.

Menard, G., Moune, S., Vlastélic, I., Aguilera, F., Valade, S., Bontemps, M., and González, R. (2014). Gas and aerosol emissions from Lascar volcano (Northern Chile): Insights into the origin of gases and their links with the volcanic activity. *Journal of Volcanology and Geothermal Research*, 287:51–67.

Merle, O. (2015). The scaling of experiments on volcanic systems. *Frontiers in Earth Science*, 3:1–15.

Messerli, B., Grosjean, M., Bonani, G., Bürgi, A., Geyh, M. A., Graf, K., Ramseyer, K., Romero, H., Schotterer, U., Schreier, H., and Vuille, M. (1993). Climate change and natural resource dynamics of the Atacama Altiplano during the last 18 000 years: a preliminary synthesis. *Mountain Research and Development*, 13(2):117–127.

Montalbetti, J. F. and Kanasewich, E. R. (1970). Enhancement of Teleseismic Body Phases with a Polarization Filter. *Geophysical Journal of the Royal Astronomical Society*, 21(2):119–129.

Mori, T., Mori, T., Kazahaya, K., Ohwada, M., Hirabayashi, J., and Yoshikawa, S. (2006). Effect of UV scattering on SO2 emission rate measurements. *Geophysical Research Letters*, 33(17):L17315.

Morioka, H., Kumagai, H., and Maeda, T. (2017). Theoretical basis of the amplitude source location method for volcano-seismic signals. *Journal of Geophysical Research: Solid Earth*, 122(8):6538–6551.

Munoz-Saez, C., Namiki, A., and Manga, M. (2015). Geyser eruption intervals and interactions: Examples from El Tatio, Atacama, Chile. *Journal of Geophysical Research: Solid Earth*, 120:1–18.

Murase, T. and McBirney, A. R. (1973). Properties of Some Common Igneous Rocks and Their Melts at High Temperatures. *Geological Society of America Bulletin*, 84(11):3563.

Nakamichi, H., Kumagai, H., Nakano, M., Okubo, M., Kimata, F., Ito, Y., and Obara, K. (2009). Source mechanism of a very-long-period event at Mt Ontake, central Japan: Response of a hydrothermal system to magma intrusion beneath the summit. *Journal of Volcanology and Geothermal Research*, 187(3-4):167–177.

Nakano, M. and Kumagai, H. (2005). Waveform inversion of volcano-seismic signals assuming possible source geometries. *Geophysical Research Letters*, 32(L12302).

Németh, K. and Kereszturi, G. (2015). Monogenetic volcanism: personal views and discussion. *International Journal of Earth Sciences*, 104(8):2131–2146.

Neuberg, J. and Luckett, R. (1996). Seismo-volcanic sources on Stromboli volcano. *Annals of Geophysics*, 39(2):377–391.

Neuberg, J., Luckett, R., Ripepe, M., and Braun, T. (1994). Highlights from a seismic broad-band array on Stromboli Volcano. *Geophysical Research Letters*, 21(9):749–752.

Neuberg, J. and Pointer, T. (2000). Effects of volcano topography on seismic broad-band waveforms. *Geophysical Journal International*, 143(1):239–248.

Neuberg, J., Tuffen, H., Collier, L., Green, D., Powell, T., and Dingwell, D. (2006). The trigger mechanism of low-frequency earthquakes on Montserrat. *Journal of Volcanology and Geothermal Research*, 153(1-2):37–50.

Newhall, C., Albano, S., Matsumoto, N., and Sandoval, T. (2001). Roles of groundwater in volcanic unrest. *Journal of the Geological Society of Philippines*, 56:69–84.

Oikawa, T., Yoshimoto, M., Nakada, S., Maeno, F., Komori, J., Shimano, T., Takeshita, Y., Ishizuka, Y., and Ishimine, Y. (2016). Reconstruction of the 2014 eruption sequence of Ontake Volcano from recorded images and interviews. *Earth, Planets and Space*, 68(79).

ONEMI, O. N. d. E. (2015). Se declara Alerta Amarilla para la Región de Antofagasta por nucleo frio en altura, October 18th, 2015. http://www.onemi.cl/alerta/. (Accessed 18 March 2019).

Orr, T. R. and Hoblitt, R. P. (2008). A versatile time-lapse camera system developed by the Hawaiian Volcano Observatory for use at Kilauea volcano, Hawai'i. *U.S. Geological Survey Scientific Investigations Report 2008-5117*, page 8 p.

OVDAS, O. V. d. l. A. d. S. (2013). Reporte Especial de Actividad Volcánica - Región de Antofagasta, Marzo 2013. n 39, Servicio Nacional de Geología y Minería (SERNAGEOMIN), Temuco.

OVDAS, O. V. d. l. A. d. S. (2015). Reporte de Actividad Volcánica (RAV) - Región de Antofagasta, Noviembre 2015. n 11, Servicio Nacional de Geología y Minería, (SERNAGEOMIN), Temuco.

Pallister, J., Hoblitt, R., and Meeker, G. (1996). Magma mixing at Mount Pinatubo: petrographic and chemical evidence from the 1991 deposits. *Fire and Mud: Eruptions and Lahars of Mount Pinatubo , Philippine*, pages 1–27.

Paskievitch, J., Read, C., and Parker, T. (2006). Remote telemetered and time-lapse cameras at Augustine Volcano. In *The 2006 Eruption of Augustine Volcano, Alaska*, pages 285–293.

Patanè, D., Di Grazia, G., Cannata, A., Montalto, P., and Boschi, E. (2008). Shallow magma pathway geometry at Mt. Etna volcano. *Geochemistry, Geophysics, Geosystems*, 9(12).

Pavez, A., Remy, D., Bonvalot, S., Diament, M., Gabalda, G., Froger, J. L., Julien, P., Legrand, D., and Moisset, D. (2006). Insight into ground deformations at Lascar volcano (Chile) from SAR interferometry, photogrammetry and GPS data: Implications on volcano dynamics and future space monitoring. *Remote Sensing of Environment*, 100(3):307–320.

Petersen, T., Caplan-Auerbach, J., and McNutt, S. R. (2006). Sustained long-period seismicity at Shishaldin Volcano, Alaska. *Journal of Volcanology and Geothermal Research*, 151(4):365–381.

Platt, U. and Stutz, J. (2008). Differential Absorption Spectroscopy. In *Differential Optical Absorption Spectroscopy*, pages 135–174. Springer Berlin Heidelberg, Berlin, Heidelberg.

Pollard, D. D., Segall, P., and Delaney, P. T. (1982). Formation and interpretation of dilatant echelon cracks. *Geological Society of America Bulletin*, 93(12):1291.

Prejean, S., Stork, A., Ellsworth, W., Hill, D., and Julian, B. (2003). High precision earthquake locations reveal seismogenic structure beneath Mammoth Mountain, California. *Geophysical Research Letters*, 30(24).

Pritchard, M. E. and Simons, M. (2002). A satellite geodetic survey of large-scale deformation of volcanic centres in the central Andes. *Nature*, 418(6894):167–171.

Richey, J. and Thomas, H. (1930). The Geology of Ardnamurchan, North-west Mull and Coll: a description of Sheet 51 and part of sheet 52 of the Geological Map. Printed under the authority of HM Stationery Office.

Richter, G., Wassermann, J., Zimmer, M., and Ohrnberger, M. (2004). Correlation of seismic activity and fumarole temperature at the Mt. Merapi volcano (Indonesia) in 2000. *Journal of Volcanology and Geothermal Research*, 135(4):331–342.

Richter, N., Salzer, J. T., de Zeeuw-van Dalfsen, E., Perissin, D., and Walter, T. R. (2018). Constraints on the geomorphological evolution of the nested summit craters of Láscar volcano from high spatio-temporal resolution TerraSAR-X interferometry. *Bulletin of Volcanology*, 80(3):21.

Rivalta, E., Taisne, B., Bunger, A., and Katz, R. (2015). A review of mechanical models of dike propagation: Schools of thought, results and future directions. *Tectonophysics*, 638:1–42.

Roman, D. C. and Gardine, M. D. (2013). Seismological evidence for long-term and rapidly accelerating magma pressurization preceding the 2009 eruption of Redoubt Volcano, Alaska. *Earth and Planetary Science Letters*, 371-372:226–234.

Rouwet, D., Sandri, L., Marzocchi, W., Gottsmann, J., Selva, J., Tonini, R., and Papale, P. (2014). Recognizing and tracking volcanic hazards related to non-magmatic unrest: A review. *Journal of Applied Volcanology*, 3(1):17.

Saccorotti, G., Lokmer, I., Bean, C. J., Di Grazia, G., and Patanè, D. (2007). Analysis of sustained long-period activity at Etna Volcano, Italy. *Journal of Volcanology and Geothermal Research*, 160(3-4):340–354.

Salzer, J. T., Thelen, W. A., James, M. R., Walter, T. R., Moran, S., and Denlinger, R. (2016). Volcano dome dynamics at Mount St. Helens: Deformation and intermittent subsidence monitored by seismicity and camera imagery pixel offsets. *Journal of Geophysical Research: Solid Earth*, 121(11):7882–7902.

Scarpa, R. and Tilling, R. I. (2012). *Monitoring and Mitigation of Volcano Hazards*. Springer, Berlin, Heidelberg.

Schaff, D. P. and Waldhauser, F. (2005). Waveform cross-correlation-based differential travel-time measurements at the northern California seismic network. *Bulletin of the Seismological Society of America*, 95(6):2446–2461.

Schirnick, C., van den Bogaard, P., and Schmincke, H.-U. (1999). Cone sheet formation and intrusive growth of an oceanic island - The Miocene Tejeda complex on Gran Canaria (Canary Islands). *Geology*, 27(3):207.

Schmiedel, T., Galland, O., and Breitkreuz, C. (2017). Dynamics of Sill and Laccolith Emplacement in the Brittle Crust: Role of Host Rock Strength and Deformation Mode. *Journal of Geophysical Research: Solid Earth*, 122(11):8860–8871.

Schmincke, H. U. (1967). Cone sheet swarm, resurgence of tejeda caldera, and the early geologic history of gran Canaria. *Bulletin Volcanologique*, 31(1):153–162.

Sens-Schönfelder, C. and Wegler, U. (2006). Passive image interferemetry and seasonal variations of seismic velocities at Merapi Volcano, Indonesia. *Geophysical Research Letters*, 33(21):L21302.

Siebert, L., Simkin, T., and Kimberly, P. (2010). *Volcanoes of the world.* Smithsonian Institution.

Sparks, R. (2003). Forecasting volcanic eruptions. *Earth and Planetary Science Letters*, 210(1-2):1–15.

Sparks, R. S. J., Biggs, J., and Neuberg, J. W. (2012). Monitoring volcanoes. *Science (New York, N.Y.)*, 335(6074):1310–1.

Stix, J. and de Moor, J. M. (2018). Understanding and forecasting phreatic eruptions driven by magmatic degassing. *Earth, Planets and Space*, 70(83).

Sutton, M., Wolters, W., Peters, W., Ranson, W., and McNeill, S. (1983). Determination of displacements using an improved digital correlation method. *Image and Vision Computing*, 1(3):133–139.

Taisne, B., Brenguier, F., Shapiro, N. M., and Ferrazzini, V. (2011). Imaging the dynamics of magma propagation using radiated seismic intensity. *Geophysical Research Letters*, 38(4):L04304.

Taisne, B. and Jaupart, C. (2009). Dike propagation through layered rocks. *Journal of Geophysical Research*, 114(B9):B09203.

Takada, A. (1990). Experimental study on propagation of liquid-filled crack in gelatin: Shape and velocity in hydrostatic stress condition. *Journal of Geophysical Research*, 95(B6):8471.

Tamburello, G., Hansteen, T. H., Bredemeyer, S., Aiuppa, A., and Tassi, F. (2014). Gas emissions from five volcanoes in northern Chile and implications for the volatiles budget of the Central Volcanic Zone. *Geophysical Research Letters*, 41(14):4961–4969.

Tassi, F., Aguilera, F., Vaselli, O., Medina, E., Tedesco, D., Delgado Huertas, A., Poreda, R., and Kojima, S. (2009). The magmatic- and hydrothermal-dominated fumarolic system at the Active Crater of Lascar volcano, northern Chile. *Bulletin of Volcanology*, 71(2):171–183.

Tokarev, P. I. (1963). On a possibility of forecasting of bezymianny volcano eruptions according to seismic data. *Bulletin Volcanologique*, 26(1):379–386.

Troll, V. R., Emeleus, C. H., and Donaldson, C. H. (2000). Caldera formation in the Rum Central Igneous Complex, Scotland. *Bulletin of Volcanology*, 62(4-5):301–317.

USGS, H. V. O. (2018). Preliminary Analysis of the ongoing Lower East Rift Zone (LERZ) eruption of Kilauea Volcano : Fissure 8 Prognosis and Ongoing Hazards. Technical report.

Vandaele, A. C., Simon, P. C., Guilmot, J. M., Carleer, M., and Colin, R. (1994). SO2 absorption cross section measurement in the UV using a Fourier transform spectrometer. *Journal of Geophysical Research*, 99(D12):25599.

Verstockt, S., Lambert, P., Walle, R. V. D., Merci, B., and Sette, B. (2009). State of the art in vision-based fire and smoke detection. *Proceedings of the 14th International Conference on Automatic Fire Detection*, 2:285–292.

Viramonte, J., Aguilera, F., Delgado, H., Rodriguez, L., Guzman, K., Jimenez, J., and Becchio, R. (2006). A new eruptive cycle of Lascar Volcano (Chile): the risk for the aeronavigation in northern Argentina. In *Garavolcan 2006, Tenerife, Spain, 22-26 May 2006*.

Voigt, S., Orphal, J., Bogumil, K., and Burrows, J. P. (2001). The temperature dependence (203-293 K) of the absorption cross sections of O3 in the 230-850 nm region measured by Fourier-transform spectroscopy. *Journal of Photochemistry and Photobiology A: Chemistry*, 143(1):1–9.

Waldhauser, F. (2001). HypoDD: A computer program to compute double-difference hypocenter locations. Technical report.

Waldhauser, F. and Ellsworth, W. L. (2000). A Double-difference Earthquake location algorithm: Method and application to the Northern Hayward Fault, California. *Bulletin of the Seismological Society of America*, 90(6):1353–1368.

Walter, T. R. (2011). Low cost volcano deformation monitoring: optical strain measurement and application to Mount St. Helens data. *Geophysical Journal International*, 186(2):699–705.

Walter, T. R., Subandriyo, J., Kirbani, S., Bathke, H., Suryanto, W., Aisyah, N., Darmawan, H., Jousset, P., Luehr, B. G., and Dahm, T. (2015). Volcano-tectonic control of Merapi's lava dome splitting: The November 2013 fracture observed from high resolution TerraSAR-X data. *Tectonophysics*, 639:23–33.

Wassermann, J. (2012). Volcano Seismology. In *New Manual of Seismological Observatory Practice 2 (NMSOP-2)*, volume 1, chapter 13, pages 1–67. Deutsches GeoForschungsZentrum GFZ.

Watanabe, T., Masuyama, T., Nagaoka, K., and Tahara, T. (2002). Analog experiments on magma-filled cracks: Competition between external stresses and internal pressure. *Earth, Planets and Space*, 54(12):1247–1261.

Wegler, U. and Lühr, B.-G. (2001). Scattering behaviour at Merapi volcano (Java) revealed from an active seismic experiment. *Geophysical Journal International*, 145(3):579–592.

Whelley, P. L., Jay, J., Calder, E. S., Pritchard, M. E., Cassidy, N. J., Alcaraz, S., and Pavez, A. (2012). Post-depositional fracturing and subsidence of pumice flow deposits: Lascar Volcano, Chile. *Bulletin of Volcanology*, 74(2):511–531.

Witt, T. and Walter, T. R. (2017). Video monitoring reveals pulsating vents and propagation path of fissure eruption during the March 2011 Pu'u 'O'o eruption, Kilauea volcano. *Journal of Volcanology and Geothermal Research*, 330:43–55.

Wooster, M. J. (2001). Long-term infrared surveillance of Lascar Volcano: Contrasting activity cycles and cooling pyroclastics. *Geophysical Research Letters*, 28(5):847–850.

Wooster, M. J. and Rothery, D. A. (1997). Thermal monitoring of Lascar Volcano, Chile, using infrared data from the along-track scanning radiometer: a 1992-1995 time series. *Bulletin of Volcanology*, 58(7):566–579.

Yamamoto, T., Nakamura, Y., and Glicken, H. (1999). Pyroclastic density current from the 1888 phreatic eruption of Bandai volcano, NE Japan. *Journal of Volcanology and Geothermal Research*, 90(3-4):191–207.

Zeng, X., Zhang, H., Zhang, X., Wang, H., Zhang, Y., and Liu, Q. (2014). Surface Microseismic Monitoring of Hydraulic Fracturing of a Shale-Gas Reservoir Using Short-Period and Broadband Seismic Sensors. *Seismological Research Letters*, 85(3):668–677.

Zimmer, M., Walter, T. R., Kujawa, C., Gaete, A., and Franco-Marin, L. (2017). Thermal and gas dynamic investigations at Lastarria volcano, Northern Chile. The influence of precipitation and atmospheric pressure on the fumarole temperature and the gas velocity. *Journal of Volcanology and Geothermal Research*, 346:134–140.

Zobin, V. (2012). *Introduction to Volcanic Seismology*. Elsevier.